

# Hot Electron Production in Plasmas Illuminated by Intense Lasers<sup>†</sup>

A. A. Balakin<sup>1</sup>, G. M. Fraiman<sup>1</sup>, and N. J. Fisch<sup>2</sup>

<sup>1</sup> *Institute of Applied Physics, Russian Academy of Sciences, Nizhni Novgorod, 603950 Russia*

<sup>2</sup> *Princeton Plasma Physics Laboratory, 08543 Princeton, NJ, USA*

Received November 19, 2004

Electron–ion collisions in strong electromagnetic fields, whether nonrelativistic or ultrarelativistic, can lead to the acceleration of electrons to high energies. The production efficiency and the Joule heating rate are calculated. Experimental verification of theoretical predictions, including the power law scaling, is presented.  
© 2005 Pleiades Publishing, Inc.

PACS numbers: 42.65.–k

Recent experiments with petawatt laser plasmas revealed interesting and unpredictable phenomena [1, 2]. A large number of fast electrons with energies up to several tens of MeV were detected. The estimated energy of these electrons was up to 10% of the pump laser energy. On the other hand, the plasma temperature was of the order of hundreds of eV and was only weakly dependent on laser intensity, but it was significantly dependent on the pump pulse duration. The number of these hot electrons was dependent on the laser intensity, and the angular distribution function of these electrons was very wide. It seems difficult to imagine that all these results are consequences of any plasma wave turbulence. Moreover, a resonant wake process such as might be used for deliberate acceleration of electrons would exhibit strong directionality  $n$  of the accelerated electrons. Thus, the review paper [1] considers the electron distribution phenomena to be rather puzzling. In this work, we point out that many of the important features of strong laser–plasma interactions and, particularly, hot-electron production can be interpreted as a consequence of electron–ion collisions.

However, traditional models of electron–ion collisions in strong laser fields that are based on the small-angle scattering approximation [3], i.e., under the assumption that quivering electrons pass near ions along straight lines, cannot explain the existing experimental results. An alternative description of Coulomb collisions, taking into account the substantial acceleration of particles during the scattering process, was proposed [4]. The application of the proposed model to the description of hot-electron production provided by electron–ion collisions and a comparison with experimental data from [1, 2] constitute the major emphasis of the present work.

The paper is organized as follows. First, we discuss the applicability conditions and the main parameter for the model being used. We show that, for relativistic levels of laser intensities, these effects are very important. We give estimates for the “energy spectrum” of hot electrons (so named after [1]) directly formed by electron–ion collisions, obtaining a power tail distribution. We estimate the total number of hot electrons produced from a unit volume per unit time. We calculate as well the heating rate of the background plasma. Finally, we compare the experimental data [1, 2] with our theoretical predictions and show good agreement between the two.

Let us note first the range of laser emission parameters where the present model is suitable. In further expressions, electron temperature  $T$  is in eV, intensity  $P$  is in  $10^{18}$  W/cm<sup>2</sup>, frequency  $\omega$  is in  $10^{15}$  Hz, density  $n$  is in  $10^{18}$  cm<sup>-3</sup>, and all other values are given in CGS units.

The plasma is assumed to be cold in comparison with the oscillatory energy, so that

$$v \ll v_{\text{osc}} = \frac{eE}{m\omega} \Leftrightarrow T \ll 6.7 \times 10^5 \frac{P}{\omega^2}. \quad (1)$$

This condition is satisfied easily and remains true practically for all plasmas interacting with short intense laser pulses, especially in the first stage of the experiment (preceding the Joule heating).

Second, the laser field intensity must be large enough for the characteristic spatial scale of scattering  $b_{\text{osc}}$  to be small compared to the radius of oscillations  $r_{\text{osc}}$ :

$$b_{\text{osc}} = \frac{e^2 Z}{v_{\text{osc}} p_{\text{osc}}} \ll r_{\text{osc}} = \frac{v_{\text{osc}}}{\omega} \Leftrightarrow \omega \ll 110 P^{3/8}, \quad (2)$$

<sup>†</sup>This article was submitted by the authors in English.

where  $p_{\text{osc}} = eE/\omega$  is the oscillatory electron momentum. This parameter range was first introduced in [4]. It has never been considered in conventional theories of electron–ion collisions, but it exhibits useful physical limits. It can be written as a limit on the ion Coulomb field potential energy at the distance of the oscillation radius  $r_{\text{osc}}$ , which must be small compared to the oscillatory energy  $m v_{\text{osc}}^2$ . In other words, the dimensionless parameter

$$\Omega = \left(\frac{b_{\text{osc}}}{r_{\text{osc}}}\right)^{\frac{1}{4}} \approx \left\{ \begin{array}{ll} \frac{1}{110} \frac{\omega}{p^{3/8}}, & p_{\text{osc}} \ll mc \\ \frac{1}{170} \frac{\sqrt{\omega}}{p^{1/8}}, & p_{\text{osc}} \gg mc \end{array} \right\} \ll 1 \quad (3)$$

needs to be small. This parameter appears naturally when the test-particle-motion equation is put into dimensionless form. In particular, in a nonrelativistic approximation for a field with linear polarization along the  $\mathbf{z}_0$  axis, this equation can be rewritten as

$$m\ddot{\mathbf{R}} = -\frac{\mathbf{R}}{R^3} + \cos\Omega t \cdot \mathbf{z}_0. \quad (4)$$

Here, the time is normalized to  $\Omega/\omega$ , and distance, to the characteristic scale

$$r_E = \sqrt{r_{\text{osc}} b_{\text{osc}}} = \sqrt{eZ/E}. \quad (5)$$

Note that the radius  $r_E$  is equal to the distance from the ion at which the amplitude of the laser field becomes of the order of the amplitude of the ion Coulomb field [4]. In terms of  $r_E$ , the smallness of the parameter  $\Omega$  is equivalent to the fact that the radius of the sphere surrounding the ion, inside of which the Coulomb field dominates, is less than the radius of electron oscillations. Moreover, this scale appears naturally when the acceleration due to the ion during the scattering process is considered (see below).

Thus, only the one parameter  $\Omega$  determines the structure of the seven-dimensional phase space of Eq. (4). In the absence of the external field ( $\Omega \rightarrow \infty$ ), particle motion is regular and well-known from the solution of the Rutherford problem [6]. A finite value of  $\Omega$  results in the formation of a stochastic layer in the vicinity of separatrix curves, but as long as  $\Omega \gg 1$ , its volume remains exponentially small.

As the field amplitude increases (which corresponds to the decrease of  $\Omega$ ), the stochastic layer broadens and, at  $\Omega \leq 1$ , occupies the whole region  $|p| \leq p_{\text{osc}}$  in momentum space. Even in this case, description of the electron dynamics is possible under the approximation of regular trajectories, but only under the condition that it is highly energetic particles ( $p \gg p_{\text{osc}}$ ) that contribute most to the collision integral. However, we are primarily interested in the opposite limit of small thermal velocities (1), specifically, when particle dynamics is

stochastic, since this is exactly the regime usually realized in experiments.

In order to describe particle scattering in the presence of the strong laser field, let us make use of the fact that the collision process proceeds in two stages [4]. In the beginning, particles are just attracted to the ion with the essential changing of the impact parameters; i.e., the variation of the test particle density and momentum direction occurs at practically constant kinetic energy of the drift motion. Also, the electron bunching happens at first stage, so that the wave phase at the momentum of “hard” collision is the same for different electrons and ions. Secondly, the “hard” collision occurs (which is actually the last collision), accompanied by a substantial change of electron momentum and by electron departure from the Coulomb center, and, at this stage, scattering at large angles with a corresponding large energy exchange is possible.

It is enough to find the particle density  $n(\mathbf{p}, t)$  before hard collision (i.e., the density in the small vicinity of the ion) for deriving the probability density of a collision with impact parameter  $\mathbf{\rho}$  over time  $W(\mathbf{p}, t) = v n(\mathbf{p}, t) d^2\rho$ . To obtain the particle density  $n(\mathbf{r}, t)$  prior to the last hard collision, one can use both the results of numerical simulation and the results of analytical analysis [4]. In both cases, the dependence  $n(\mathbf{r}, t)$  is a singular periodical function of  $t$ :

$$n(\mathbf{r}, t) = n_e \frac{a}{\rho} \sum_{n=-\infty}^{\infty} \delta\left(\omega t - \left(n + \frac{1}{2}\right)\pi\right). \quad (6)$$

Here,  $\rho = \sqrt{x^2 + y^2}$  is the transverse electron coordinate (impact parameter) before the hard collision,  $a(\mathbf{v}) \geq b_v = e^2 Z/mv^2$  is a coefficient describing the efficiency of the attraction of particles to the ion and depending on the direction of the initial velocity  $\mathbf{v}$  relative to  $\mathbf{v}_{\text{osc}}$ . It is important to emphasize that this dependence on drift-velocity direction is weak [4]. Thus, for the major fraction of test particles, we have quasi-isotropic scattering, so that we can use expression (6) for further estimates. It is also important to note that the obtained singularity of the probability function occurs independently from the wave polarization and intensity. In particular, it can be shown that the same estimate is appropriate for ultrarelativistic intensities as well.

Distribution (6) describes electrons that have experienced strong attraction to the ion. Previously, such particles were called “representative” electrons [4]. Note that, for the majority of such particles, one can consider the scattering of the total velocity,  $\mathbf{V} = \mathbf{v} + \mathbf{v}_{\text{osc}}(t)$ , as a small-angle scattering.

The hard collision can be described by the relations from the Rutherford-problem solution [6]. With smallness of drift velocity (1) taken into account, momentum variation here is determined by the oscillatory momen-

tum value at the collision moment and by the impact parameter  $\rho$ :

$$\Delta p_{\Delta p \ll p_{\text{osc}}} \approx 2p_{\text{osc}} \frac{b_{\text{osc}}}{\rho}, \quad b_{\text{osc}} = \frac{e^2 Z}{p_{\text{osc}} v_{\text{osc}}}. \quad (7)$$

It is supposed in (6) that collisions occur only when the oscillatory velocity reaches its maximum (it is the effect of bunching that provides the latter [4, 5]) and the collision is momentary. The latter condition implies the upper limit on the impact parameter:

$$\rho/v_{\text{osc}} \ll \pi/\omega_o \Leftrightarrow \rho \ll r_{\text{osc}}. \quad (8)$$

Otherwise, for such large impact parameters, velocity variation during the scattering process is substantial and Rutherford formulas (7) are not applicable. However, this limitation is not important, since the energy variation  $\Delta W$  of such far-flung particles in strong fields ( $b_{\text{osc}} \ll r_{\text{osc}}$ ) is small compared to the oscillatory energy:

$$\frac{2m\Delta W}{p_{\text{osc}}^2} \Big|_{\rho > r_{\text{osc}}} \leq \left(\frac{b_{\text{osc}}}{r_{\text{osc}}}\right)^2 \ll 1. \quad (9)$$

Equation (7) allows us to find the relation between the density function on impact parameters (6) and the distribution of the hot-particle production rate on momentum per unit volume and unit time:

$$g(p) = v n_i n(\rho) \frac{\rho d\rho}{p dp} = n_i n(\rho) v \frac{4b_{\text{osc}}^2 p_{\text{osc}}^2}{p^4}. \quad (10)$$

Using density distribution (6), one finally gets

$$g(p) = 4n_i n_e p_{\text{osc}}^2 \frac{v a b_{\text{osc}}}{p_{\text{osc}} p^3}. \quad (11)$$

Note that the dependence of the hot-electron distribution on momentum has the universal law  $\sim 1/p^3$  for any (relativistic and nonrelativistic) energies of particles.

From the relation between the kinetic energy and the particle momentum

$$w = \sqrt{p^2 c^2 + m^2 c^4} - mc^2 \approx \begin{cases} p^2/2m, & p \ll mc \\ cp, & p \gg mc \end{cases}$$

( $m$  is the rest mass of electron), it is easy to find the particle energy distribution for the nonrelativistic case  $w \ll mc^2$

$$g(w) = 8\pi n_i n_e m p_{\text{osc}}^2 \frac{v a b_{\text{osc}}}{p_{\text{osc}} (2mw)^{\frac{3}{2}}} \quad (12)$$

and the relativistic one  $w \gg mc^2$

$$g(w) = 8\pi n_i n_e p_{\text{osc}}^2 \frac{v c a b_{\text{osc}}}{p_{\text{osc}} w^2}. \quad (13)$$

We will insert here the dimensional estimate for the particle density  $dn(w)/dt = \int_w^\infty g(w) dw$  with energies exceeding some limit in the relativistic case for the period of the field, supposing  $w, cp_{\text{osc}} \gg mc^2$ :

$$\frac{dn(w)}{dt} [\text{cm}^{-3} \text{ s}^{-1}] \approx \frac{10^{25} n_e Z}{\sqrt{T} w}. \quad (14)$$

In this relation, particle energy  $w$  is measured in MeV and other quantities are measured in units specified in (1). Note that this density does not depend on laser intensity. However, the total number of hot electrons depends on pump intensity due to the larger interaction volume with laser intensities.

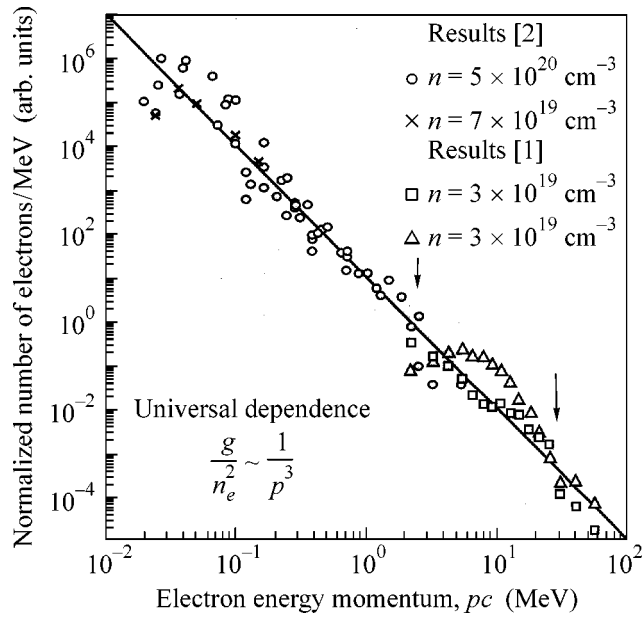
In particular, considering the number of particles with energy higher than 1 MeV for plasma<sup>1</sup> with density  $10^{19} \text{ cm}^{-3}$  and volume  $300 \times 20 \times 20 \mu\text{m}$  at a pulse duration of 10 ps, one finds that the hot-electron number must be of the order of  $10^9 Z$  particles, where  $Z \geq 10$  is the charge of ions in plasma, which coincides well with the number of particles,  $10^{10}$  to  $10^{11}$ , measured experimentally. Another comparison with experimental data that one can perform is to observe that the number of hot electrons produced by collisions must be proportional to the square of the plasma density. We compared this result with the data taken from [2] and found good agreement between the theory and experiment.

In experiments [1, 2], it is the distribution of particles scattered off in the same direction that is measured, i.e., the distribution function over momentum  $g(p)$  as found in (11). Superposing theoretical dependence (11) on the experimental data points, one can see good coincidence between the two (figure). Note that, in the figure, we combined four different series of experimental measurements [1, 2].

The figure represents further evidence of the collisional effects on hot electrons. The collisional heating gives a natural upper limit to the momentum (and, correspondingly, the energy) that particles may achieve. This limit is the doubled oscillatory momentum  $2p_{\text{osc}}$ , which, under the conditions of the experiment [2] (figure), corresponds to an energy of about 2 MeV. We see, indeed, the abrupt decrease of the hot-particle number for energies higher than 2 MeV. Similar results were obtained in [1].<sup>2</sup> It is important to emphasize that what is shown in the figure is the dependence on the ‘‘energy momentum’’ (electron kinetic momentum mul-

<sup>1</sup> These data correspond to experiment [1].

<sup>2</sup> We should note that much more energetic particles (with energies up to  $p_{\text{osc}}^2/m$  or  $p_{\text{osc}}^3/m^2 c$ ) can be produced as a result of electron-ion collisions in the ultrarelativistic case, while distribution law (11) is applicable only for electrons with energy less than the oscillatory energy  $p_{\text{osc}} c \gg mc^2$ . The momentum and angular distribution law of such ultraenergetic particles is different from (11). It is probable that exactly these electrons have been seen at distribution tails in experiments [1, 7].



The comparison between the experimental results (figure from [1, 2]) and the theoretical (solid line, (11)) dependence of hot-electron distribution on “energy momenta”  $pc$ . Arrows show the “cutoff” effect.

multiplied by the speed of light,  $pc$ ), not on the actual energy. These would be identical only in the case of ultrarelativistic particles in [1]. The possibility of this interpretation of the experimental results might be connected with the fact that the magnetic scintillator used for the measurements actually measures the distribution function of the particle momentum rather than the particle energy.<sup>3</sup>

Further comparisons with the experimental data can be performed by analyzing the heating rate  $Q = \int g(w)w dw$ , which is easy to calculate using particle energy distribution (12). By substituting  $a = b_v$ , one gets the expression for the heating rate:

In the nonrelativistic case  $w, cp_{\text{osc}} \ll mc^2$ ,

$$Q \approx 4\pi n_i n_e m v_{\text{osc}}^2 v a b_{\text{osc}}; \quad (15)$$

in the ultrarelativistic case  $cp_{\text{osc}} \gg mc^2$ ,

$$Q \approx 4\pi n_i n_e m c^2 c b_c^2 \frac{c}{v}. \quad (16)$$

Here,  $r_a = v/\omega$  is the adiabaticity radius, i.e., the distance over which incident particles with an impact parameter exceeding  $r_a$  have adiabatically small energy variation;  $b_c = e^2 Z/mc^2$  is the Rutherford radius, which, if estimated with for  $Z = 1$  and for electron velocities

<sup>3</sup> Taking this into account and also considering the dependence on plasma density and the “cutoff” effect, we might conjecture that the power law shown in [2] was aberrant due to a calibration mistake.

equal to the speed of light  $c$ , matches the classical electron radius.

Expression (16) must be supplemented by an additional term describing the contribution of ultrarelativistic electrons to distribution law (13). This term will obviously coincide with (16), at least approximately, but, for a more precise calculation, a more detailed description of the collisions is necessary. That description would need to take into account the radiation losses and quantum effects taking place in the case when the momentum variation becomes significant.

Note that the heating rate in ultrarelativistic case (16) does not depend on the pumping field amplitude. The estimate of the heating rate per unit volume,

$$Q[\text{eV cm}^{-3} \text{ s}^{-1}] = 10^{13} \frac{nZ}{\sqrt{T}}, \quad (17)$$

allows one to estimate the plasma temperature (kinetic energy) after the pulse has passed. In particular, for a pulse with an ultrarelativistic intensity and a duration of 1 ps (which corresponds to the conditions of the experiment in [1]), the electron temperature is of the order of hundreds of eV. That is exactly the order of the temperature (200–600 eV) observed in the experiment in [1].

The results represented above were obtained using the pair-collisions approximation, wherein the probability of the simultaneous collisions of three and more particles is assumed to be negligible. The condition of this approximation is the smallness of the interaction volume  $nV_{\text{int}} \ll 1$ . Usually (without a field), the interaction volume is estimated as  $V_{\text{int}} = b_v^3$ , giving

$$nb_v^3 \ll 1 \Leftrightarrow nr_D^3 \gg 1, \quad (18)$$

where  $r_D = \sqrt{4\pi e^2 n/mv_T^2}$  is the Debye radius. In strong fields, the interaction volume is  $V_{\text{int}} \approx \sigma_{\text{eff}} r_{\text{osc}}$  ( $\sigma_{\text{eff}} = \pi b_v b_{\text{osc}}$  is the effective collisional cross section [4]), which leads to the mild requirement

$$\frac{r_E}{r_D} = 3.67 \times 10^{-3} \frac{\sqrt{ZI}}{\sqrt{n^4 P}} \ll 1. \quad (19)$$

But this condition, obviously, can be derived using different approaches. Indeed, the new scale  $r_E$  that appears as the particle attraction is taken into account is the distance to the ion (multiplied by the factor  $\sqrt{2\pi} r_E$ ; see [4]), at which a particle moving near the ion with an oscillation velocity hits the ion after a single oscillation. The effect of attraction will not be “washed off” by neighboring particles if this scale is less than the Debye shielding radius  $r_D$ . Hence, one again comes to condition (19). One more simple condition can be considered, namely, the absence of the influence of external ions on the dynamics of hard collision. The volume of

hard collision is  $V_{\text{hard}} = 2\pi r_E^2 r_{\text{osc}}$ . So, the condition is  $nV_{\text{hard}} \ll 1$  or

$$2\pi r_E^2 r_{\text{osc}} n = \frac{Z}{2} \omega_{pl}^2 / \omega^2 \ll 1, \quad (20)$$

the ordinary condition of transparent plasmas. Both conditions (19) and (20) are simple to fulfill.

To summarize, in considering the two types of particles being scattered (Eq. (6)), we derived an expression for the effective collision frequency and the hot-particle energy distribution, which agree well with experimental data. Moreover, taking into account the “representative” electrons (the singular part of (6)) is necessary for an adequate explanation of the experimental results.

This work was supported by the Russian Foundation for Basic Research (project no. 02-02-17275), the Council of the President of the Russian Federation for the Support of Young Russian Scientists and Leading Scientific Schools (project no. MK-1193.2003.02), US

DOE (contract no. DE-AC02-76 CHO3073), and the US DARPA.

#### REFERENCES

1. M. H. Key, M. D. Cable, T. E. Cowan, *et al.*, *Phys. Plasmas* **5**, 1966 (1998); S. P. Hatchett, C. G. Brown, T. E. Cowan, *et al.*, *Phys. Plasmas* **7**, 2076 (2000).
2. K. Koyama, N. Saito, and M. Tanimoto, in *ICPP 2000* (Quebec, Canada, 2000), ICPP 4051, p. MP1.067.
3. V. P. Silin, *Zh. Éksp. Teor. Fiz.* **47**, 2254 (1964) [*Sov. Phys. JETP* **20**, 1510 (1965)]; J. M. Dawson and C. Oberman, *Phys. Fluids* **6**, 394 (1963).
4. G. M. Fraiman, V. A. Mironov, and A. A. Balakin, *Phys. Rev. Lett.* **82**, 319 (1999); *Zh. Éksp. Teor. Fiz.* **115**, 463 (1999) [*JETP* **88**, 254 (1999)].
5. G. M. Fraiman, V. A. Mironov, and A. A. Balakin, *Zh. Éksp. Teor. Fiz.* **120**, 797 (2001) [*JETP* **93**, 695 (2001)].
6. L. D. Landau and E. M. Lifshitz, *Course of Theoretical Physics*, Vol. 1: *Mechanics*, 4th ed. (Nauka, Moscow, 1988; Pergamon, Oxford, 1989).
7. S.-Y. Chen, M. Krishnan, A. Maksimchuk, *et al.*, *Phys. Plasmas* **6**, 4739 (1999).

# Anomalous Behavior near $T_c$ and Synchronization of Andreev Reflection in Two-Dimensional Arrays of SNS Junctions

T. I. Baturina<sup>1</sup>, Yu. A. Tsaplin<sup>1,2</sup>, A. E. Plotnikov<sup>1</sup>, and M. R. Baklanov<sup>3</sup>

<sup>1</sup> *Institute of Semiconductor Physics, Siberian Division, Russian Academy of Sciences, Novosibirsk, 630090 Russia*  
e-mail: tatbat@isp.nsc.ru

<sup>2</sup> *Novosibirsk State University, Novosibirsk, 620090 Russia*

<sup>3</sup> *Interuniversity Microelectronics Center, B-3001 Leuven, Belgium*

Received October 25, 2004; in final form, December 2, 2004

The temperature dependences of resistance and the current–voltage characteristics of two-dimensional arrays of superconductor–normal metal–superconductor (SNS) junctions have been measured at low temperatures. It has been found that, in two-dimensional arrays of SNS junctions the following occur: (i) a change in the energy spectrum within an interval of the order of the Thouless energy is observed even when the thermal spread far exceeds the Thouless energy for a single SNS junction; (ii) the manifestation of the subharmonic gap structure with high harmonic numbers is possible even when the energy relaxation length is smaller than that required for the realization of a multiple Andreev reflection in a single SNS junction. These results point to the synchronization of a great number of SNS junctions. A possible mechanism that may be responsible for the features observed in the behavior of two-dimensional arrays of SNS junctions is discussed. © 2005 Pleiades Publishing, Inc.

PACS numbers: 73.23.-b; 74.45.+c; 74.81.Fa

Andreev reflection is a microscopic mechanism responsible for the charge transport through a normal metal–superconductor interface [1]. An electron-like quasiparticle in the normal metal with an energy lower than the superconducting gap ( $\Delta$ ) is reflected from the boundary as a hole-like quasiparticle, while a Cooper pair is transferred to the superconductor. If the normal metal is sandwiched between two superconductors, an additional charge-transfer mechanism, namely, multiple Andreev reflection (MAR), arises. This mechanism was proposed in [2] to explain the subharmonic gap structure (SGS) observed as dips in the differential resistance curves at voltages  $eV_n = 2\Delta/n$  ( $n$  is an integer). The MAR concept is as follows: owing to sequential Andreev reflections from normal metal–superconductor (NS) interfaces, a quasiparticle passing through the normal region can accumulate an energy of  $2\Delta$ , which is sufficient for the transition to single-particle states of the superconductor. Although, by now, ample experimental data on the transport properties of NS and superconductor–normal metal–superconductor (SNS) junctions are available [3] and the existing theoretical models fairly well describe the phenomena observed in the experiments [4–6], the properties of multiply connected SNS systems are poorly investigated. It should be noted that systems consisting of superconducting islands incorporated into a normal metal are spontaneously formed in disordered superconducting films [7]. In view of this circumstance, it is of interest to study the properties of model multiply connected SNS systems

with superconducting and normal regions formed in a controlled way.

This paper is devoted to the properties of two-dimensional arrays of SNS junctions fabricated on the basis of a 20-nm-thick PtSi superconducting film (with a critical temperature of  $T_c = 0.64$  K) [8]. The transport parameters of the initial PtSi film were as follows: the resistance per square at  $T = 4.2$  K was  $R_{sq} = 22.8 \Omega$ , the mean free path was  $l = 1.35$  nm, and the diffusion coefficient was  $D = 7.3$  cm<sup>2</sup>/s. The initial samples were fabricated by photolithography in the form of Hall bars, which were 50  $\mu\text{m}$  wide and 100  $\mu\text{m}$  long. Then, by electron beam lithography with subsequent plasma chemical etching, the initial film was thinned in preset regions. Figure 1a schematically represents the structure under study. It consists of periodically arranged film areas with a thickness of 20 nm (islands), between which the film is thinned by plasma chemical etching. The period of the structure is 1  $\mu\text{m}$ , and the island dimensions are  $0.8 \times 0.8 \mu\text{m}$ . This structure completely covers the whole area of the Hall bar (Fig. 1b). Thus, the number of islands between the potential terminals is  $50 \times 100$ . To control the depth of etching, a reference film was etched uniformly over its surface simultaneously with the structure etching. The low-temperature transport measurements were performed by the standard four-terminal method with a low-frequency ( $\sim 10$  Hz) alternating current using the lock-in detection technique. The current was within the range 1–10 nA.

The experiment showed that the decrease in the film thickness due to plasma chemical etching used in the structure fabrication process suppressed the superconducting transition. At the same time, in the islands, whose thickness remained equal to that of the initial PtSi film, the suppression of the superconducting transition was nearly insignificant. Hence, there is a certain temperature interval within which the thinned film is in the normal (N) state and the islands are in the superconducting (S) state. In this temperature interval, the structures under study represent a two-dimensional array of SNS junctions. Moreover, since the superconducting and normal regions of the SNS junctions fabricated in the aforementioned way consist of the same material, the formation of tunnel barriers at the NS interfaces is excluded and a high transparency of the NS interfaces can be *a priori* expected.

Figure 2 shows the temperature dependence of resistance for two samples that only differ in the film thickness between the islands. The resistance per square of the reference film at  $T = 4.2$  K is  $995 \Omega$  for sample S#1 and  $1483 \Omega$  for sample S#2. For all structures studied, a noticeable decrease in resistance with decreasing temperature is observed slightly below the temperature  $T_c$  of the initial 20-nm-thick PtSi film. As the temperature decreases (Fig. 2), a small decrease in the resistance is first observed at  $T \sim 0.61$  K; then, the resistance increases, reaches a maximum, and then decreases again. Such an anomalous behavior of the temperature dependence of resistance in the narrow temperature range near  $T_c$  was never observed before, and the origin of this behavior is unknown.

To explore the nature of this anomaly, we studied the current-voltage characteristics of the samples. For sample S#1, Fig. 3 shows the dependences of the differential resistance ( $dV/dI$ ) on the bias voltage. The measured values of  $dV/dI$  are given per square. The total voltage is divided by the number of junctions (100) in the rows lying between the potential terminals. For a square array, this procedure yields the average voltage across one SNS junction, and this quantity is represented by the abscissa axis in Fig. 3 (below, all dependences of the differential resistance on the bias voltage are plotted in similar coordinate systems). The dependences of  $dV/dI$  on  $V$  are symmetric with respect to the direction of the current. As one can see from the dependences shown in Fig. 3, an increase in temperature leads to a suppression of the excessive conductivity and, at  $T \approx 570$  mK, the minimum observed at  $V = 0$  is replaced by a maximum. It should be emphasized that the change of a minimum to a maximum in the differential resistance curves at zero bias voltage occurs in the same temperature interval within which the anomaly is observed in the temperature dependence of resistance (in Fig. 2, for sample S#1, this interval is indicated by arrows).

Let us estimate the characteristic energy scales for the two-dimensional array of SNS junctions under

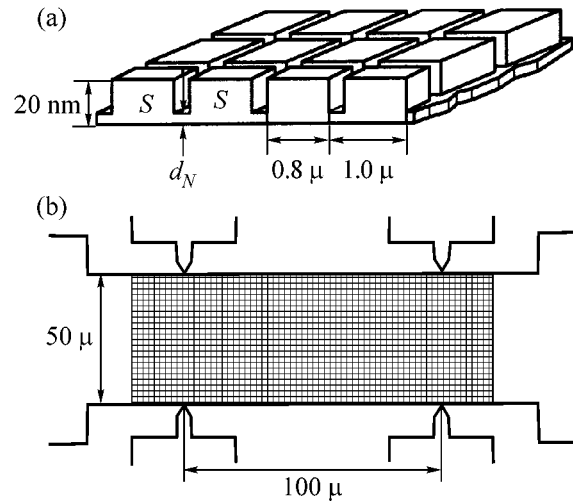


**Fig. 1.** Schematic representation of the structure: (a) profile of the film modulated in thickness (the geometric dimensions are indicated in the figure); (b) position of the structured film on the sample used for the measurements.

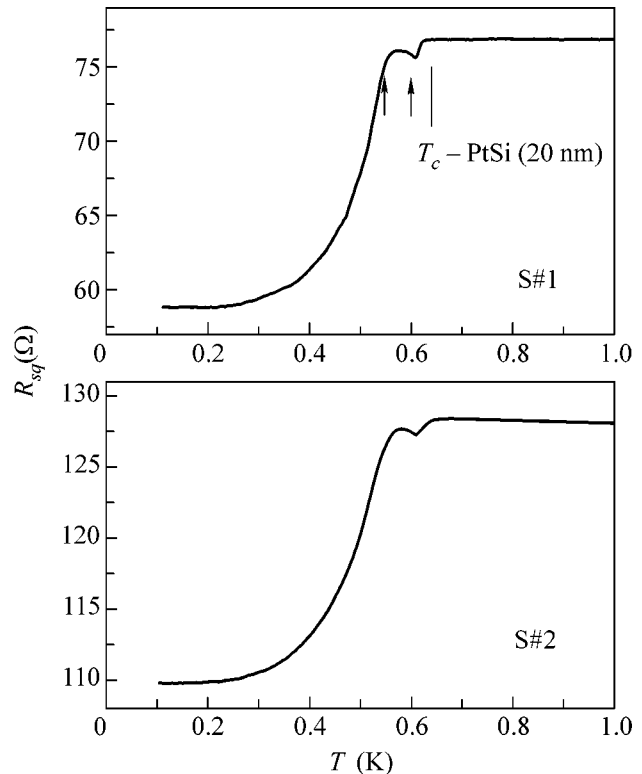


**Fig. 2.** Temperature dependence of the resistance per square for samples S#1 and S#2. The dash in the plot indicates the superconducting transition temperature for the initial 20-nm-thick PtSi film. The arrows indicate the temperature range from 0.545 to 0.599 K.

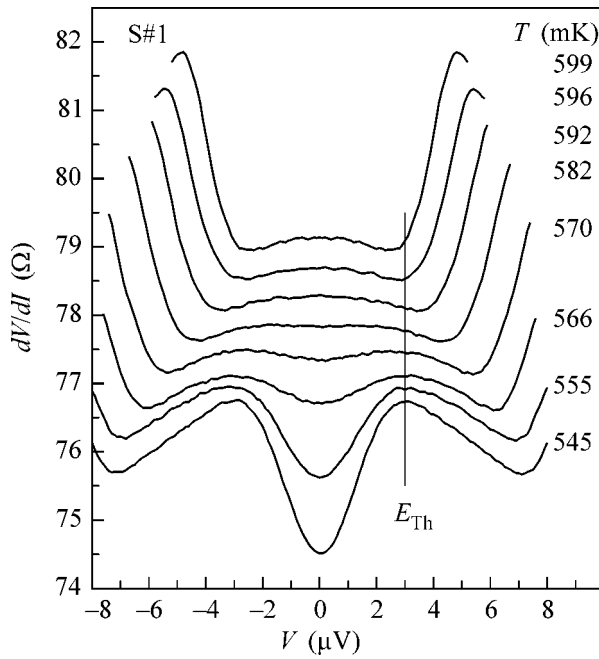


**Fig. 3.** Differential resistance per square versus the bias voltage per SNS junction for sample S#1. All dependences, except for the lower one, are sequentially shifted upwards by  $0.5 \Omega$ .

study. The energy corresponding to the voltage at which the minimum is suppressed at zero bias and temperatures below 570 mK is estimated as  $eV_{ex} \approx 3 \mu\text{eV}$ . The presence of the maximum in the differential resistance at  $T > 570 \text{ mK}$  may be caused by the minimum that occurs in the density of states in the normal region. A theoretical study of the properties of diffusive NS junctions [9] shows that the decrease in the density of states is caused by the presence of coherent Cooper pairs in the normal metal. According to the theory, at a distance  $x$  from the NS interface, only the pairs from the energy window  $E_F \pm E_{\text{Th}}$  (the coherence window), where  $E_{\text{Th}} = \hbar D/x^2$  is the Thouless energy, will remain coherent. Therefore, the density of states has a minimum at energies  $E < E_{\text{Th}}$  and a maximum at  $E = E_{\text{Th}}$ , and this maximum is higher than the density of states in the normal metal. The experimental study of the density of states as a function of the distance to the NS interface [10] showed a good agreement with the theory. Note that this effect manifests itself in two ways. On the one hand, the presence of coherent Cooper pairs leads to a decrease in the resistance of the normal region (an analog of the Maki–Thompson correction), and, on the other hand, the pairing leads to a decrease in the density of single-particle states (an analog of the correction to the density of states in the Cooper channel). These competing contributions may lead to a nonmonotonic temperature dependence of the resistance of SNS junctions [11]. Let us estimate the Thouless energy  $E_{\text{Th}} = \hbar D/L^2$  for the structure under study, where  $L = 0.2 \mu\text{m}$

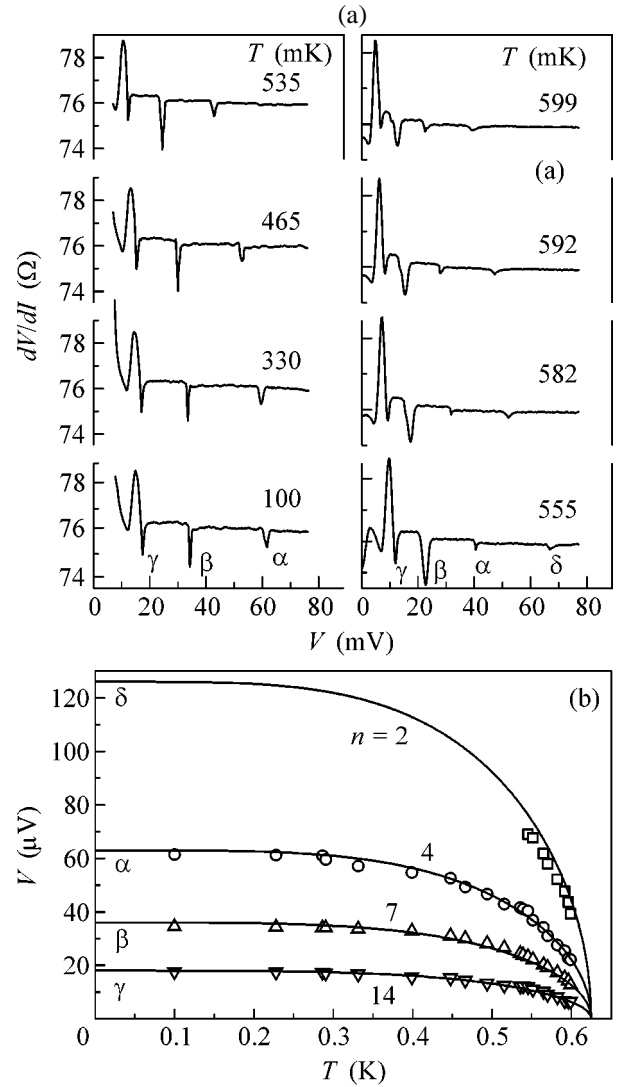
is the length of the normal region and  $D = 2 \text{ cm}^2/\text{s}$  is the diffusion coefficient for the reference film. Then, the Thouless energy is  $E_{\text{Th}} = 3 \mu\text{eV}$ , which nearly coincides with the characteristic voltage value (in Fig. 3, this value is indicated by the vertical straight line). However, for the observation of the effects associated with changes in the quasiparticle spectrum at the Thouless energy, the necessary condition is  $kT < E_{\text{Th}}$ . In the temperature range of interest, e.g., at  $T = 580 \text{ mK}$ , the thermal broadening is  $kT \approx 50 \mu\text{eV}$ , which noticeably exceeds the correlation energy  $E_{\text{Th}}$  for the SNS junctions forming the array. Thus, one should expect that the processes determined by  $E_{\text{Th}}$  would not manifest themselves in the differential resistance curves. However, the experimental dependences clearly display the suppression of the maximum at a voltage of about  $E_{\text{Th}}/e$ . This fact suggests that the effect observed in the experiment is collective; i.e., the whole array is responsible for its manifestation. Note that the total bias voltage is  $eV_{\Sigma} = 300 \mu\text{eV}$ ; i.e., it is much higher than  $kT$ . We will return to discussing this issue after presenting the results that, in our opinion, also testify to a correlation in the behavior of the array of SNS junctions.

Figure 4a shows the dependences of the differential resistance on the bias voltage per one SNS junction. These dependences have pronounced minima at some voltage values (the minima are marked by  $\alpha$ ,  $\beta$ , and  $\gamma$  in the plot). When the temperature increases, the minima are shifted to lower voltages and, in the interval from 550 to 600 mK, one more minimum ( $\delta$ ) appears; at lower temperatures, this minimum is absent. The temperature dependences of the positions of these features are shown in Fig. 4b by different symbols. The solid lines in Fig. 4b represent the temperature dependences of the superconducting energy gap  $2\Delta(T)/en$ , where  $\Delta(T)$  is the temperature dependence of the superconducting energy gap predicted by the BCS microscopic superconductivity theory and  $n$  is an integer (the corresponding values are indicated in Fig. 4b). The exact value of  $\Delta(0)$  for platinum monosilicide is unknown. The estimate by the formula  $\Delta(0) = 1.76kT_c$  ( $T_c = 0.88 \text{ K}$  for bulk PtSi [12]) yields the value  $\Delta/e \approx 133 \mu\text{V}$ . If we set  $\Delta/e = 126 \mu\text{V}$ , the positions of the features in the voltage dependences of the differential resistance will be determined by the condition  $eV = 2\Delta(T)/n$ . From Fig. 4b, one can see that the temperature dependences of the positions of minima observed in the experimental differential resistance curves functionally coincide with the dependences  $2\Delta(T)/en$ . From this fact, we can conclude that these features represent the subharmonic gap structure (SGS).

However, there are two circumstances clearly indicating that it is difficult to treat the features observed at bias voltages equal to  $2\Delta(T)/en$  as the manifestation of the SGS caused by multiple Andreev reflections that occur independently in each SNS junction and that this interpretation is impossible for large values of  $n$ . First, the conventional mechanism of the SGS formation in a

single SNS junction implies that, for the appearance of a subharmonic of number  $n$ , an  $n$ -fold passage of quasiparticles through the normal region is necessary without any energy relaxation. In other words, the energy relaxation length ( $l_\epsilon$ ) must be no smaller than  $n \cdot L$  [6]. The energy relaxation length can be estimated from the known phase-breaking length  $l_\phi$ . In the temperature range of interest,  $l_\epsilon$  can exceed  $l_\phi$  by no more than an order of magnitude [13]. When a carrier acquires an energy of  $2\Delta = 252$  meV, it is heated to a temperature of  $\sim 3$  K. According to our magnetotransport measurements, at this temperature, we have  $l_\phi = 40$  nm. Then, the most optimistic estimate yields  $l_\epsilon \sim 0.4 \mu\text{m}$ . This value is much smaller than  $14 \times 0.2 \mu\text{m} = 2.8 \mu\text{m}$ , which is necessary for the realization of the subharmonic with  $n = 14$ . Second, it is difficult to expect that normal regions are fully identical, i.e., characterized by exactly the same resistance. Evidently, we are dealing with a network of different resistances. Therefore, when a current flows through the structure, the voltages across the normal regions are different. This means that, if, for some of the normal regions, the condition  $eV = 2\Delta/n$  is satisfied at a given value of the current, for other regions it will be satisfied at some other values of the current. Only when the resistances are close to each other is it possible to observe the subharmonic gap structure as a result of the statistical averaging; however, this structure will be smeared in proportion to the deviations of actual resistances from the average value. These speculations lead to a natural conclusion that, for a network of random resistances, the observation of the subharmonic gap structure is impossible. Contrary to this conclusion, the experiment shows that the SGS still manifests itself, although it is somewhat irregular; i.e., it lacks some of the harmonics. Similar results for an array of SNS junctions of other configuration were obtained in [14]. No theory has been developed to describe multiply connected SNS systems, and, on the basis of the theoretical results obtained for single SNS junctions, it is difficult to explain the observation of subharmonics with numbers reaching  $n = 14$ .

In considering the properties of single SNS junctions, the superconducting regions are usually assumed to be large and to serve as reservoirs for electrons. The fundamental distinction of the array of SNS junctions is the finite size of the superconducting regions ( $L_S$ ). Therefore, it is necessary to take into account the possibility of the mutual influence of the Andreev reflection processes that occur at the interfaces of one superconducting island. In NSN junctions, in addition to the “common” Andreev reflection, when an electron-like excitation is reflected at the interface of the superconductor with transformation into a hole-like excitation (in Fig. 5, process 1:  $e_i \longleftrightarrow h_i$ ), an additional process of crossed Andreev reflection  $e_i \longleftrightarrow h'_j$  (process 2) is possible, when the electron-like and hole-like excitations are on different sides of the superconducting region [15–17]. As a consequence, such a reflection in



**Fig. 4.** Sample S#1: (a) differential resistance per square versus the bias voltage per SNS junction (i.e., the voltage across the terminal is divided by 100); (b) positions of the features marked in Fig. 4a as functions of temperature. The solid lines represent  $2\Delta(T)/en$ . The respective values of  $n$  are indicated in the plot. The dependences are calculated for  $\Delta(0) = 126 \mu\text{eV}$  and  $T_c = 0.625$  K.

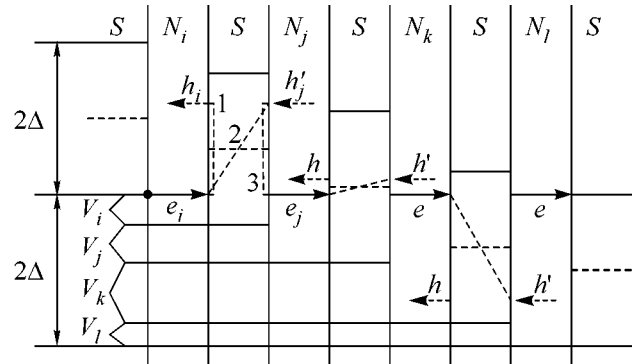


**Fig. 5.** Andreev reflection process in a semiconductor representation for a structure consisting of alternating superconducting and normal regions.

combination with the common Andreev reflection, which occurs on one side of the superconductor (process 3), leads to the passage of quasiparticles without any energy loss. Note that, for the observation of the  $n$ th subharmonic of Andreev reflection, the realization of this mechanism of charge transport does not require that the voltage across each of the normal regions be exactly equal to  $V_n = 2\Delta/en$ . It is sufficient that the total voltage across the chain of normal regions connected in series through superconducting regions be equal to  $2\Delta/e$ :

$$\sum_{s=i}^{i+n-1} V_s = 2\Delta/e.$$

Moreover, for the observation of the  $n$ th subharmonic of Andreev reflection, the condition  $l_\epsilon > nL$  need not necessarily be satisfied. It is sufficient that the energy relaxation length be greater than the distance between the superconducting regions ( $l_\epsilon > L$ ). We also note that the crossed Andreev reflection process makes a considerable contribution to the charge transport through an NSN junction even if the size of the superconducting region is several times greater than the superconducting coherence length  $\xi$  [15, 18]. In our case,  $\xi(0) \approx 70$  nm, and, at  $T = 100$  mK, we have  $L_s/\xi \approx 10$ .

We believe that this charge-transport mechanism is responsible for the features observed in the experiment. Returning to the behavior of the two-dimensional array of SNS junctions near zero bias, we note that the synchronous Andreev reflection on both sides of the superconducting regions should lead to correlated changes of the energy spectra in normal regions, by analogy with the formation of minibands and minigaps in semiconductor superlattices.

We are grateful to M.V. Feigel'man for useful discussions and for the interest taken in our work. This work was supported by the Russian Academy of Sciences (the program "Quantum Macrophysics"), the Ministry of Science of the Russian Federation (the program "Superconductivity of Mesoscopic and Strongly Correlated Systems"), and the Russian Foundation for Basic Research (project no. 03-02-16368).

## REFERENCES

1. A. F. Andreev, Zh. Éksp. Teor. Fiz. **46**, 1823 (1964) [Sov. Phys. JETP **19**, 1228 (1964)].
2. T. M. Klapwijk, G. E. Blonder, and M. Tinkham, Physica B & C (Amsterdam) **109–110**, 1657 (1982).
3. B. Pannetier and H. Courtois, J. Low Temp. Phys. **118**, 599 (2000).
4. G. E. Blonder, M. Tinkham, and T. M. Klapwijk, Phys. Rev. B **25**, 4515 (1982).
5. M. Octavio, M. Tinkham, G. E. Blonder, and T. M. Klapwijk, Phys. Rev. B **27**, 6739 (1983); K. Flensberg, J. Bindeslev Hansen, and M. Octavio, Phys. Rev. B **38**, 8707 (1988).
6. E. V. Bezuglyi, E. N. Bratus', V. S. Shumeiko, *et al.*, Phys. Rev. B **62**, 14439 (2000).
7. M. V. Feigel'man, A. I. Larkin, and M. A. Skvortsov, Phys. Rev. Lett. **86**, 1869 (2001).
8. R. A. Donaton, S. Jin, H. Bender, *et al.*, Microelectron. Eng. **37/38**, 504 (1997).
9. B. J. van Wees, P. de Vries, P. H. C. Maguee, and T. M. Klapwijk, Phys. Rev. Lett. **69**, 510 (1992).
10. S. Gueron, N. O. Birge, D. Esteve, and M. H. Devoret, Phys. Rev. Lett. **77**, 3025 (1996).
11. A. F. Volkov and H. Takayanagi, Phys. Rev. B **56**, 11 184 (1997).
12. B. T. Matthias, T. H. Geballe, and V. B. Compton, Rev. Mod. Phys. **35**, 1 (1963).
13. S. I. Dorozhkin, F. Lell, and W. Schoepe, Solid State Commun. **60**, 245 (1986).
14. T. I. Baturina, Z. D. Kvon, and A. E. Plotnikov, Phys. Rev. B **63**, 180503 (2001).
15. J. M. Byers and M. E. Flatté, Phys. Rev. Lett. **74**, 306 (1995).
16. G. Deutscher and D. Feinberg, Appl. Phys. Lett. **76**, 487 (2000).
17. A. Jacobs and R. Kümmel, Phys. Rev. B **64**, 104515 (2001).
18. D. Beckman, H. B. Weber, and H. von Löhneysen, Phys. Rev. Lett. **93**, 197003 (2004).

*Translated by E. Golyamina*

# Electric-Dipole Increase in NMR Intensity in Mixed-Valence Complexes

M. A. Ivanov<sup>1</sup>, V. Ya. Mitrofanov<sup>2</sup>, L. D. Fal'kovskaya<sup>3</sup>,  
A. Ya. Fishman<sup>2</sup>, and B. S. Tsukerblat<sup>4</sup>

<sup>1</sup> *Institute of Metal Physics, National Academy of Sciences of Ukraine, pr. Vernadskogo 36, Kiev, 03680 Ukraine*  
*e-mail: ivanov@imp.kiev.ua*

<sup>2</sup> *Institute of Metallurgy, Ural Division, Russian Academy of Sciences, ul. Amundsena 101, Yekaterinburg, 620016 Russia*

<sup>3</sup> *Institute of Metal Physics, Ural Division, Russian Academy of Sciences, ul. S. Kovalevskoi 18, Yekaterinburg, 620219 Russia*

<sup>4</sup> *Ben-Gurion University of the Negev, Beer-Sheva, 84105 Israel*

Received November 30, 2004

The possibility of a considerable increase in NMR intensity has been shown for absorption on mixed-valence  $3d$  ions in magnetically ordered crystals. This effect is determined by the high intensity of electric dipole transitions between the ground and low excited levels of a mixed-valence complex, as well as by the existence of the unfrozen orbital angular momentum in such complexes, which mixes nuclear and electron states. © 2005 Pleiades Publishing, Inc.

PACS numbers: 31.30.Gs; 76.60.–k

## 1. INTRODUCTION

It is well-known that, in transition-metal oxides at low concentrations of either nonisovalent substitutional atoms or vacancies in both the cation and anion sublattices, extra electrons or holes appear and Coulomb forces localize them on nearest neighbors of the indicated centers [1]. In this case, each  $3d$  ion nearest to an impurity provides an equivalent possibility for localizing an extra electron or hole, so that orientationally degenerate impurity complexes (centers), which contain different-valence ions of the same  $3d$  element such as  $\text{Mn}^{4+}\text{--Mn}^{3+}$ ,  $\text{Cr}^{4+}\text{--Cr}^{3+}$ , etc., are formed in a crystal. The ground state of such a mixed-valence complex, where the excess charge can be transferred between  $3d$  ions, can be orbitally degenerate [2]. In this case, in addition to the ordinary Jahn–Teller properties, such a mixed-valence complex has features caused by the redistribution of the excess charge between the ions of the complex and, correspondingly, by the stabilization of the dipole moment when orientational degeneracy is removed due to an external perturbation or random crystal fields. Owing to its local nature, NMR can enable one to acquire valuable information on the features of the magnetic state of the systems under consideration and to analyze the local charge distribution in mixed-valence centers.

In this work, the possibility of the electric dipole mechanism of the absorption of electromagnetic radiation is analyzed for transitions between the magnetic states of the nuclear spins of  $3d$  ions in magnetically ordered crystals. Trigonal mixed-valence centers in spinel-structure crystals are taken as examples. The fea-

tures of the NMR spectra of the  $3d$  ions in such centers are primarily determined by the presence of an anomalously strong direct hyperfine interaction  $A_1(\sigma_\zeta I_\zeta)$  between the orbital angular momentum  $\sigma_\zeta$  and nuclear spin  $\mathbf{I}$  in one of the charge configurations  $3d^n$  or  $3d^{n\pm 1}$  [3]. It has been shown that the intensity of the NMR transitions under consideration can increase considerably due to the coupling between the orbital angular momentum and electric dipole moment in a mixed-valence center.

## 2. HAMILTONIAN OF THE MIXED-VALENCE CENTER

We consider the mixed-valence center that consists of three exchange-coupled  $3d$  ions with an extra  $t_{2g}$  hole localized on them and that is formed by a point defect in the cation sublattice of the spinel-structure crystal (Fig. 1). We assume that the ground energy level for ions with the  $3d^{n-1}$  configuration is doubly degenerate in the orbital quantum number (a trigonal  $E$  term). The ground electron state of other two magnetic ions with the  $3d^n$  configuration is treated as orbitally nondegenerate.

We restrict our consideration to the cluster states with the maximum projection of the total spin of the system, assuming that the ground state of the triad is among these states. The six lower levels of the triad (a mixed-valence center) are formed when states are mixed. Each of these levels is doubly degenerate and corresponds to the localization of the extra  $t_{2g}$  hole on one of the ions of the cluster. The corresponding wave

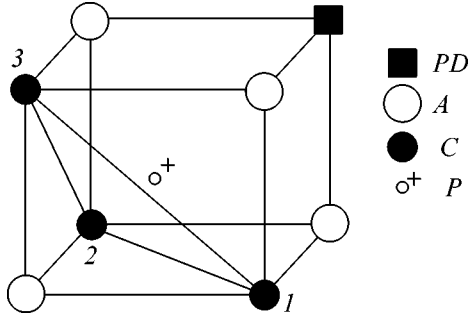


**Fig. 1.** Mixed-valence center formed near a point defect by three cations in the octahedral spinel sublattice with an extra  $t_{2g}$  hole located on them:  $PD$  is the point defect in the cation sublattice,  $A$  is an anion,  $C$  is a cation, and  $P$  is the hole.

functions are transformed according to the irreducible representations  $A_1$ ,  $A_2$ , and  $2E$  of the triad symmetry group  $C_{3v}$  [4].

Let us assume that the splitting of the ground  $E$  term is determined by the spin-orbit interaction and by some low-symmetric intracrystalline fields:

$$H_{el} = -\lambda S_{\zeta} \sigma_{\zeta} + h_{\xi} \sigma_{\xi} + h_{\eta} \sigma_{\eta}, \quad \sigma_{\zeta} = \begin{pmatrix} -1 & 0 \\ 0 & 1 \end{pmatrix}, \quad (1)$$

$$\sigma_{\xi} = \begin{pmatrix} 0 & 1 \\ 1 & 0 \end{pmatrix}, \quad \sigma_{\eta} = \begin{pmatrix} 0 & i \\ -i & 0 \end{pmatrix}.$$

Here,  $\sigma_{\zeta}$ ,  $\sigma_{\xi}$ ,  $\sigma_{\eta}$  are the orbital operators specified on the trigonal basis, the  $\zeta$  axis is the trigonal symmetry axis of the triad in the chosen coordinate system,  $\lambda$  is the parameter of the spin-orbit interaction, and  $h_{\xi}$  and  $h_{\eta}$  are the components of the low-symmetric field on the mixed-valence center. Random elastic and electric crystalline fields, as well as magnetic anisotropy fields created, e.g., due to the second-order effects in the spin-orbit interaction, can serve as low-symmetric fields [2, 3].

For simplicity, we describe the hyperfine interactions on the mixed-valence center only by the following terms (similar to [4]):

$$H_{hf}(3d^n) = A'_0(\mathbf{IS}'), \quad (2)$$

$$H_{hf}(3d^{n-1}) = A_0(\mathbf{IS}) + A_1 \sigma_{\zeta} I_{\zeta}.$$

Here, only the isotropic term is taken into account for ions with the  $3d^n$  configuration, whereas the isotropic hyperfine interaction and an anisotropic term describing the direct interaction between the orbital angular momentum  $\sigma_{\zeta}$  and the nuclear spin  $\mathbf{I}$  are taken into account for ions with the  $3d^{n-1}$  configuration, and  $S'$  and  $S$  are the spins of  $3d$  ions in the respective electron configurations.

It is convenient to transform the Hamiltonian of the mixed-valence center using functions diagonalizing electron Hamiltonian (1) and hyperfine-interaction Hamiltonian (2) written in the mean-field approximation as the basis functions. In this case, after the corresponding transformations of “rotation” [5] for the orbital operators ( $\sigma_{\zeta}$ ,  $\sigma_{\xi}$ ,  $\sigma_{\eta} \rightarrow \tau^z$ ,  $\tau^+$ ,  $\tau^-$ ) and nuclear spin operators ( $I_x$ ,  $I_y$ ,  $I_z \rightarrow I^z$ ,  $I^+$ ,  $I^-$ ), the Hamiltonian of the mixed-valence center can be represented in the form

$$H = H_0 + V, \quad H_0 = E_{el} \tau^z + \sum_{k=1}^3 \Omega_k I_k^z,$$

$$V = A_1 \left\{ \tau^+ \sum_{k=1}^3 [V_k^* I_k + V_k I_k^+] + \text{c.c.} \right\},$$

$$E_{el} = 2\sqrt{(\lambda S_{\zeta})^2 + h^2}, \quad h^2 = h_{\xi}^2 + h_{\eta}^2, \quad (3)$$

$$\sigma_v = \gamma_v \tau^z + B_v \tau^+ + B_v^* \tau^-, \quad (v = \xi, \eta, \zeta),$$

$$I_{\alpha} = \beta_{\alpha} I^z + D_{\alpha} I^+ + D_{\alpha}^* I^-, \quad (\alpha = x', y', z').$$

Here,  $E_{el}$  is the splitting energy of the ground  $E$  term of the mixed-valence center and  $\Omega_k$  are the NMR transition frequencies for ions with  $k = 1, 2, 3$ , which belong to the mixed-valence center. It is seen that the anisotropic hyperfine interaction mixes orbital and nuclear excitations on the mixed-valence center.

### 3. ELECTRIC DIPOLE NMR ABSORPTION IN MIXED-VALENCE CENTERS

The coefficient of the electric dipole absorption of electromagnetic radiation on the centers under consideration is represented as

$$\chi_{\alpha\beta} = N_0 \frac{\pi\omega}{cn} \text{Im} \langle \langle P_{\alpha}/P_{\beta} \rangle \rangle_{\omega}$$

$$= 4N_0 p_0^2 \frac{\pi\omega}{cn} \text{Im} \{ K_{\alpha\beta} \langle \langle \tau^+ | \tau^- \rangle \rangle_{\omega} + K_{\alpha\beta}^* \langle \langle \tau^- | \tau^+ \rangle \rangle_{\omega} \},$$

$$P_{\alpha} = 2p_0 [(B_{\xi} \cos \varphi_{\alpha} - B_{\eta} \sin \varphi_{\alpha}) \tau^+ + (B_{\xi}^* \cos \varphi_{\alpha} - B_{\eta}^* \sin \varphi_{\alpha}) \tau^- + (\gamma_{\xi} \cos \varphi_{\alpha} - \gamma_{\eta} \sin \varphi_{\alpha}) \tau^z], \quad (4)$$

$$K_{\alpha\beta} = |B_{\xi}|^2 \cos \varphi_{\alpha} \cos \varphi_{\beta} + |B_{\eta}|^2 \sin \varphi_{\alpha} \sin \varphi_{\beta} - B_{\xi} B_{\eta}^* \cos \varphi_{\alpha} \sin \varphi_{\beta} - B_{\eta} B_{\xi}^* \sin \varphi_{\alpha} \cos \varphi_{\beta}.$$

Here,  $\mathbf{P}$  is the dipole moment of the mixed-valence complexes under consideration;  $N_0$  is the number of the mixed-valence centers;  $c$  is the speed of light;  $n$  is the refractive index of the medium; the parameter  $p_0$  characterizes the maximum attainable dipole moment on the mixed-valence center; and  $\varphi_{\alpha} = 0$  ( $z$ ),  $2\pi/3$  ( $x$ ),  $-2\pi/3$  ( $y$ ).

After simple transformations with the use of Green's functions calculated in the second order of perturbation theory in the hyperfine-interaction Hamiltonian, the absorption coefficient in the region of NMR frequencies is expressed as

$$\begin{aligned} \chi_{\alpha\beta} &= \frac{32}{9} N_0 \frac{\pi^2 \omega}{cn} p_0^2 A_1^2 \langle \tau^z \rangle \frac{2K_{\alpha\beta}}{E_{el}^2} (1-x^2)(1-\gamma_\zeta^2) \\ &\times \sum_{k=1}^3 |\mathbf{n}_k \mathbf{D}_k|^2 \langle I_k^z \rangle \delta(\Omega_k - \omega), \\ \Omega_k^2 &= [\bar{\Omega} - \Delta\Omega x \sqrt{1-\gamma_\zeta^2} \cos(\varphi - \varphi_k) \langle \tau^z \rangle]^2 \\ &+ \left[ -\frac{2}{3} A_1 \gamma_\zeta \sqrt{1-x^2} \langle \tau^z \rangle \right]^2 \\ &+ 2 \left[ -\frac{2}{3} A_1 \gamma_\zeta \sqrt{1-x^2} \langle \tau^z \rangle \right] \\ &\times [\bar{\Omega} - \Delta\Omega x \sqrt{1-\gamma_\zeta^2} \cos(\varphi - \varphi_k) \langle \tau^z \rangle] (\mathbf{n} \mathbf{n}_k), \\ \langle \tau^z \rangle &= -\frac{1}{2} \tanh\left(\frac{E_{el}}{2T}\right), \quad \langle I_k^z \rangle = -\frac{1}{2} \tanh\left(\frac{\Omega_k}{2T}\right), \\ \bar{\Omega} &= \frac{1}{3}(A_0 S + 2A_0' S'), \quad \Delta\Omega = \frac{2}{3}(A_0 S - A_0' S'), \\ \varphi_k &= 2\pi k/3, \quad \cot\varphi = h_\xi/h_\eta. \end{aligned} \quad (5)$$

Here,  $\mathbf{n}$  and  $\mathbf{n}_k$  are the unit vectors directed along the magnetization and trigonal axes of ions of the mixed-valence center and the parameter  $x$  characterizes the mixing of two states of the mixed-valence center that correspond to the repeated  $E$  representations.

Total absorption on mixed-valence centers includes not only the contribution of the mixed-valence clusters shown in Fig. 1 with the  $[\bar{1}11]$  trigonal axis but also the contributions of other three types of clusters with the trigonal symmetry axes  $[1\bar{1}\bar{1}]$ ,  $[\bar{1}\bar{1}\bar{1}]$ , and  $[11\bar{1}]$ . Expression (5) is averaged over the distribution of random crystalline fields with the use of the Gaussian distribution function

$$g(h, \varphi) = \pi^{-1} \Delta^{-2} \exp\{-h^2/\Delta^2\}, \quad h^2 = h_\xi^2 + h_\eta^2, \quad (6)$$

where  $\Delta$  is the standard deviation of random crystalline fields.

#### 4. RESULTS CALCULATED FOR NMR SPECTRAL DISTRIBUTIONS

As an example, we consider mixed-valence centers in comparatively weak random fields such that  $\Delta \ll \lambda$ . Figure 2 shows the frequency dependence of the NMR spectrum of the mixed-valence centers that is typical for the electric dipole mechanism. The external mag-

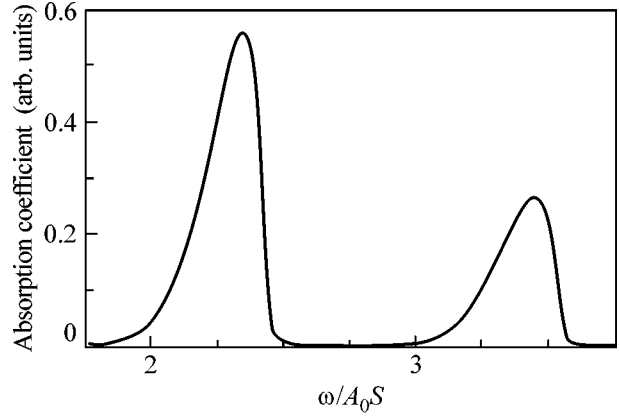


**Fig. 2.** Frequency dependence of the NMR spectrum on mixed-valence centers for electric dipole absorption. The magnetic field is directed along the  $[001]$  axis,  $x = 0.5$ ,  $A_0 S = A_0' S'$ ,  $A_1/A_0 S = 10$ ,  $T/J = 0.1$ ,  $\Delta J = 0.1$ , and  $J = \sqrt{3} \lambda S_{\max}$ .

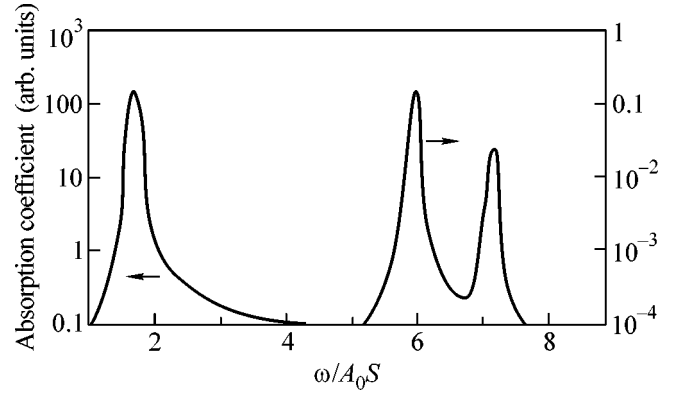


**Fig. 3.** Frequency dependence of the NMR spectrum on mixed-valence centers for electric dipole absorption. The magnetic field is directed along the  $[110]$  axis. The left part of the figure corresponds to the mixed-valence centers with the trigonal axes  $[\bar{1}\bar{1}\bar{1}]$  and  $[11\bar{1}]$ , the right part, to the mixed-valence centers with the trigonal axes  $[\bar{1}\bar{1}1]$  and  $[1\bar{1}\bar{1}]$ ,  $x = 0.5$ ,  $A_0' S'/A_0 S = 2$ ,  $A_1/A_0 S = 20$ ,  $T/J = 0.1$ ,  $\Delta J = 0.1$ , and  $J = \sqrt{3} \lambda S_{\max}$ .

netic field is directed along the tetragonal axis of the crystal,  $\mathbf{n} \parallel [001]$ , and all four types of the centers make the same contribution to the absorption coefficient. The left maximum of absorption is attributed to the triad ions with numbers  $k = 1$  and  $2$ , and the right maximum, to the ion with number  $3$ .

Figure 3 illustrates the anomalously strong anisotropy in the intensity of electric dipole NMR absorption in the mixed-valence centers. It has been shown that the spectral intensities for the mixed-valence centers with different directions of the trigonal axes may differ by several orders of magnitude. This figure corresponds to the orientation of magnetization in the crystal along the

[110] axis. For this direction of magnetization, mixed-valence clusters are divided into two groups: clusters with the trigonal axes  $[\bar{1}11]$  and  $[1\bar{1}1]$ , which are perpendicular to the chosen magnetization direction, and clusters with the trigonal axes  $[\bar{1}\bar{1}\bar{1}]$  and  $[11\bar{1}]$ , which are not perpendicular to magnetization. For the clusters of the first type, the spin-orbit interaction does not contribute to the splitting of the degenerate state of a cluster, and the NMR frequencies depend only on random fields:

$$\Omega_k = \frac{1}{3} |2A_0'S' + A_0S - 2(A_0S - A_0'S')x \cos(\varphi - \varphi_k) \langle \tau_z \rangle|. \quad (7)$$

The clusters of this type are responsible for the absorption band whose center is at the frequency  $\omega_1 = (2A_0'S' + A_0S)/3$ . The second group of clusters gives relatively weak peaks at frequencies (5) characteristic of the ions of the cluster when the random field is equal to  $h \cong \Delta$ . The ratio of the corresponding intensities is equal to  $(\lambda/\Delta)^4$ . The electric dipole mechanism is obviously most substantial in magnetic fields perpendicular to the trigonal axis of the mixed-valence clusters. In this case, when the splitting of the degenerate state is minimal, a noticeable increase in NMR signals can be expected.

## 5. CONCLUSIONS

Thus, the existence of a large electric dipole contribution has been found in the NMR spectral distribution of the mixed-valence centers. It has been shown that the possibility of a considerable increase in the NMR signal appears in principle due to the existence of the unfrozen orbital angular momentum. This effect is attributed to the high intensity of the electric dipole transition between the split components of the  $E$  term of the mixed-valence center and mixing between orbital and nuclear states due to the hyperfine interaction.

The ratio of magnetic-to-electric dipole absorption intensities for electromagnetic radiation in the NMR frequency band under consideration is about  $p_0^2 A_1^2 E_{el}^{-2} / \mu_B^2 A_0^2 \epsilon_{k=0}^{-2}$ , where  $\epsilon_{k=0}$  is the energy of a spin wave with  $\mathbf{k} = 0$ . The electric dipole contribution is at least comparable with the magnetic dipole contribution in wide ranges of the ratios  $A_1/A_0$  and  $\epsilon_{k=0}/E_{el}$ . The

spectral distributions for electric dipole and magnetic dipole contributions to electromagnetic-radiation absorption at the NMR frequencies noticeably differ from each other. This result enables one to understand the appearance of additional peaks in the NMR spectra of the systems under consideration for the case of comparable contributions of the above mechanisms.

At present, in the absence of an adequate theory for describing NMR spectra in magnetically ordered systems with mixed-valence  $3d$  ions, the above results extend the possibilities for qualitative interpretation of experimental data. It is sufficient to mention  $^{55}\text{Mn}$  NMR spectra [6–8] in  $(\text{LaMn})_{1-2x}\text{O}_3$  crystals containing mixed-valence Mn ions. The corresponding  $^{55}\text{Mn}$  NMR spectrum [6] is a set of several inhomogeneously broadened lines. A sharp increase in the NMR signal was observed in these systems over the entire frequency band when the concentration of defects was increased. These results have not yet been interpreted.

This work was supported by the Russian Foundation for Basic Research.

## REFERENCES

1. L. P. Gor'kov, *Usp. Fiz. Nauk* **168**, 665 (1998) [*Phys. Usp.* **41**, 589 (1998)].
2. B. S. Tsukerblat and M. I. Belinskii, *Magnetochemistry and X-ray Spectroscopy of Exchange Clusters* (Shtiintsa, Kishinev, 1983) [in Russian].
3. A. Abragam and B. Bleaney, *Electron Paramagnetic Resonance of Transition Ions* (Clarendon, Oxford, 1970; Mir, Moscow, 1973), Vol. 2.
4. V. Ya. Mitrofanov, A. Ya. Fishman, and B. S. Tsukerblat, *Pis'ma Zh. Éksp. Teor. Fiz.* **59**, 46 (1994) [*JETP Lett.* **59**, 45 (1994)].
5. S. V. Tyablikov, *Methods in the Quantum Theory of Magnetism*, 2nd ed. (Nauka, Moscow, 1975; Plenum, New York, 1967).
6. K. N. Mikhalev, S. A. Lekomtsev, A. P. Gerashchenko, *et al.*, *Fiz. Met. Metalloved.* **93** (4), 32 (2002) [*Phys. Met. Metallogr.* **93**, 322 (2002)].
7. G. Allodi, R. De Renzi, G. Guidi, *et al.*, *Phys. Rev. B* **56**, 6036 (1997).
8. Cz. Kapusta, P. C. Riedi, W. Kocemba, *et al.*, *J. Appl. Phys.* **87**, 7121 (2000).

*Translated by R. Tyapaev*

## Specificity of Magnetoelectric Effects in a New GdMnO<sub>3</sub> Magnetic Ferroelectric

A. M. Kadomtseva<sup>1</sup>, Yu. F. Popov<sup>1</sup>, G. P. Vorob'ev<sup>1</sup>, K. I. Kamilov<sup>1</sup>, A. P. Pyatakov<sup>1</sup>,  
V. Yu. Ivanov<sup>2</sup>, A. A. Mukhin<sup>2</sup>, and A. M. Balbashov<sup>3</sup>

<sup>1</sup> Moscow State University, Vorob'evy gory, Moscow, 119992 Russia

e-mail: Kadomts@plms.phys.msu.ru

<sup>2</sup> General Physics Institute, Russian Academy of Sciences,  
ul. Vavilova 38, Moscow, 117942 Russia

<sup>3</sup> Moscow Power Engineering Institute (Technical University),  
ul. Krasnokazarmennaya 14, Moscow, 105835 Russia

Received November 18, 2004; in final form, December 9, 2004

A complex study of the magnetic, electric, magnetoelectric, and magnetoelastic properties of GdMnO<sub>3</sub> single crystals has been performed in the low-temperature region in strong pulsed magnetic fields up to 200 kOe. An anomaly of the dielectric constant along the *a* axis of a crystal has been found at 20 K, where a transition from an incommensurate modulated phase to a canted antiferromagnetic phase, as well as electric polarization along the *a* and *b* axes of the crystal induced by the magnetic field  $H \parallel b$  ( $H_{cr} \sim 40$  kOe), is observed. Upon cooling the crystal in an electric field, the magnetic-field-induced electric polarization changes its sign depending on the sign of the electric field. The occurrence of the electric polarization is accompanied by anisotropic magnetostriction, which points to a correlation between the magnetoelectric and magnetoelastic properties. Based on these results, it has been stated that GdMnO<sub>3</sub> belongs to a new family of magnetoelectric materials with the perovskite structure. © 2005 Pleiades Publishing, Inc.

PACS numbers: 75.80.+q

### INTRODUCTION

Magnetoelectric interactions in systems (magnetoelectric materials) where magnetic and electric orderings can coexist have been investigated in a great number of works [1–3]. Recently, interest has been enhanced in studying unusual magnetoelectric materials based on the rare-earth manganites RMn<sub>2</sub>O<sub>5</sub> and RMnO<sub>3</sub> with the perovskite structure. It should be noted that RMnO<sub>3</sub> compounds, depending on the ionic radius of the rare-earth ion, can exhibit different structures: the perovskite structure for R = La–Tb and the hexagonal structure for R = Ho–Lu. The RMnO<sub>3</sub> crystals with the hexagonal structure are magnetoelectric materials and have been reasonably well studied [5]. The study of magnetoelectric effects in the RMnO<sub>3</sub> system is only starting.

Data on the interplay of magnetic and electric properties in TbMnO<sub>3</sub> and DyMnO<sub>3</sub> single crystals, exhibiting an orthorhombically distorted perovskite structure described by the *Pbnm* space group, have been reported recently [6, 7]. Since these compounds are centrosymmetric antiferromagnets, in which the classical magnetoelectric effect cannot be observed, the magnetoelectric effect observed in [6, 7] was attributed to a transition from an incommensurate modulated structure to a commensurate one. However, the nature of this transition is not fully understood, and it is necessary to seek

new nonstandard mechanisms of its occurrence to explain the specificity of the magnetoelectric interactions of rare-earth manganites with the perovskite structure.

It was also of interest to study the possibility of magnetoelectric effects in manganites with the RMnO<sub>3</sub> perovskite structure with other rare-earth ions, in particular, GdMnO<sub>3</sub>, about which contradictory data have been reported [6, 8]. Thus, it is argued in [6] that there is no spontaneous polarization in GdMnO<sub>3</sub> along the principal crystallographic axes throughout the entire temperature range above 2 K. At the same time, the conclusion that a small spontaneous polarization along the *a* axis exists at  $T < 13$  K was made in [8]. According to [9], GdMnO<sub>3</sub> at room temperature exhibits the same orthorhombically distorted perovskite structure (*Pbnm* space group) as TbMnO<sub>3</sub>. At temperatures below  $T_N \sim 40$  K, the spins of Mn<sup>3+</sup> ions are ordered in an incommensurate sinusoidal antiferromagnetic structure, which transforms to a canted antiferromagnetic structure (*A<sub>y</sub>F<sub>z</sub>*) at  $T_{CA} \sim 20$  K, whereas the antiferromagnetic ordering of the spins of Gd<sup>3+</sup> ions occurs at  $T_{N_2} \sim 6.5$  K [9].

This work is devoted to studies of the magnetic, electric, magnetoelectric, and magnetoelastic properties of GdMnO<sub>3</sub> single crystals upon spontaneous phase

transitions and phase transitions induced by a strong magnetic field.

## EXPERIMENTAL RESULTS AND DISCUSSION

GdMnO<sub>3</sub> single crystals were grown by floating zone melting with optical heating. Powder x-ray phase analysis showed that the crystals are single phase and exhibit an orthorhombic crystal structure of the *Pbnm* type. The crystals were oriented by the x-ray method. Samples were cut from them in the form of cubes with edges directed along the principal crystallographic axes with sizes of about several millimeters for measuring polarization and magnetostriction. For measuring the dielectric constant, the samples were cut in the form of plane-parallel wafers or disks with characteristic sizes  $d \sim 1$  mm and area  $S \sim 20$  mm<sup>2</sup>, and electrical contacts were attached to their surfaces with a silver paste.

The magnetic properties of single crystals were determined by measurements of torque curves, which were performed on a torque magnetometer in constant magnetic fields up to 12 kOe in the temperature range 4.2–50 K. The temperature dependence of the spontaneous magnetic moment along the *c* axis of a GdMnO<sub>3</sub> single crystal obtained from measurements of torque curves in a magnetic field of 3 kOe is shown in Fig. 1. It should be noted that this method is the most sensitive for detecting a transverse, weak ferromagnetic moment in canted antiferromagnets. In Fig. 1, it is evident that the weak ferromagnetic moment appears below  $T_{CA} \approx 20$  K and increases with decreasing temperature, reaching a value of  $35 \text{ s cm}^3 \text{ g}^{-1}$  at a temperature of 8 K; then, the magnetization drops sharply and, below the ordering temperature for the Gd ions, has a value of  $4 \text{ s cm}^3 \text{ g}^{-1}$ , which is close to the weak ferromagnetic moment of the manganese subsystem [10].

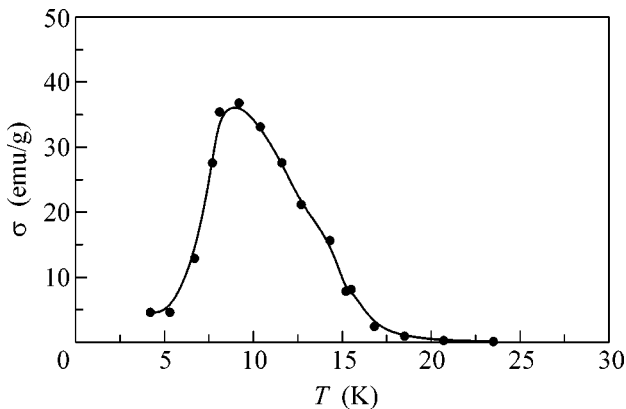


**Fig. 1.** Temperature dependence of the spontaneous magnetization along the *c* axis of the GdMnO<sub>3</sub> crystal.

These data correspond to the results of direct magnetization measurements [9]. The absence of the contribution of the gadolinium subsystem to the weak ferromagnetic moment in a low-temperature region is evidently associated with the antiferromagnetic ordering of Gd<sup>3+</sup> spins. It is also possible that the magnetic manganese and gadolinium subsystems differ in symmetry, as was observed for rare-earth orthoferrites [11].

In addition to magnetic properties, the temperature dependence of the dielectric constant has also been studied at a frequency of 1 MHz (Fig. 2). The dielectric constant  $\epsilon$  was calculated by the formula

$$\epsilon = Cd/\epsilon_0 S,$$

where  $\epsilon_0 = 8.85 \times 10^{-12}$  F/m is the permittivity of free space and  $C$ ,  $d$ , and  $S$  are the electric capacitance, thickness, and surface of the crystal, respectively. The crystal capacitance was determined using an automatic LCR meter E7-12. The anomaly in the temperature dependence  $\epsilon_c(T)$  along the *c* axis of the crystal was small at this frequency, whereas it was more pronounced at lower frequencies [6]. With decreasing temperature, a sharp jump of the dielectric constant was observed in the dependence  $\epsilon_a(T)$  at  $T_{CA} \approx 20$  K, where a transition from the incommensurate sinusoidal antiferromagnetic ordering of Mn<sup>3+</sup> to the canted structure takes place according to [9]. In the vicinity of  $T_{N_2}$ , a pronounced anomaly of the dielectric constant associated with the antiferromagnetic ordering of Gd<sup>3+</sup> was also observed; that is, a close connection between the electric and magnetic subsystems was manifested.

With the aim of further studying the correlation between the magnetic and electric states of the system, the dependences of the electric polarization on the external magnetic field were studied by the method described in [12]. When the external magnetic field was

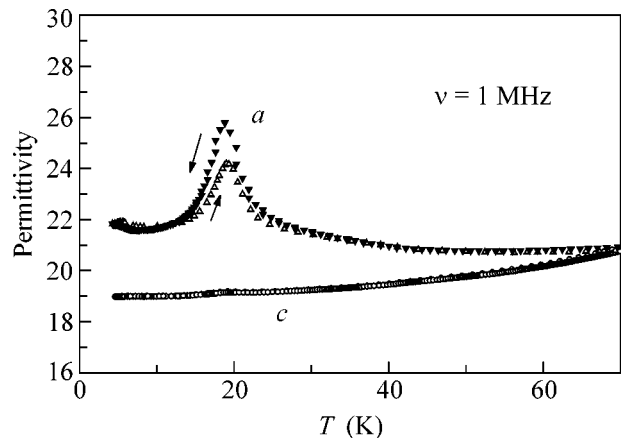


**Fig. 2.** Temperature dependence of the dielectric constant along the *a* and *c* axes of the GdMnO<sub>3</sub> crystal.

applied along the  $a$  and  $c$  axes, no longitudinal electric polarization was observed over the entire temperature range 10–50 K. When the magnetic field was aligned with the  $b$  crystal axis, along which the spins of  $\text{Mn}^{3+}$  ions were oriented, jumps in the electric polarization were observed in the temperature range 10–20 K at certain threshold fields.

Figure 3 shows the dependences of the electric polarization along various crystallographic directions at a temperature of 5 K on the magnetic field  $H \parallel b$  as obtained after the poling of a  $\text{GdMnO}_3$  crystal in an electric field of  $E = -1500$  V/cm below  $T_N$ . It is evident that the polarization increases most sharply along the  $a$  and  $b$  crystal axes in the threshold field  $H_{\text{cr}} \sim 40$  kOe, whereas the dependence  $P_c(H_b)$  along the  $c$  axis exhibits a smoother behavior. Note that the variation of the electric polarization along the  $a$  crystal axis with increasing field is opposite to that observed for the  $b$  and  $c$  axes. The magnetic-field dependence of the electric polarization exhibits a significant hysteresis with respect to the field. It should be noted that the magnetic-field-induced electric polarization along the  $b$  and  $a$  axes changed its value and sign depending on the sign of the applied electric field (Fig. 4). This is apparently associated with the existence of electric domains differing in the sign of polarization.

The dependence of the longitudinal polarization on  $H \parallel b$ ,  $P_b(H_b)$ , measured at various temperatures in the absence of an electric field, is shown in Fig. 5. At  $T > 21$  K, the electric polarization decreases sharply, which is apparently associated with a transition to an incommensurate sinusoidal state. It should be noted that the magnitude of the threshold field inducing this unconventional transition weakly depends on temperature. It is remarkable that the results obtained for  $\text{GdMnO}_3$  are formally similar to the data reported in [6, 7] for  $\text{TbMnO}_3$  and  $\text{DyMnO}_3$ , where the initial electric polarization was directed along the  $c$  axis. When the magnetic field  $H \parallel b$  was applied, this polarization in the case of  $\text{TbMnO}_3$  and  $\text{DyMnO}_3$  was reoriented to the  $a$  axis at the threshold field. The magnitude of the effect in  $\text{TbMnO}_3$  and  $\text{DyMnO}_3$  was substantially larger than that in  $\text{GdMnO}_3$ .

Since the method used for measurements allows one to detect only the change in the polarization in a magnetic field rather than the existence of polarization at  $H = 0$ , it is rather difficult to make an unambiguous conclusion about the existence of spontaneous electric polarization. Different signs of the change in  $P_a$  and  $P_b$  upon cooling in electric fields of different signs corroborate its existence in  $\text{GdMnO}_3$  in the direction perpendicular to the  $c$  axis at  $T < T_{\text{CA}}$ . The coexistence of electric polarization and a canted structure at these temperatures can also be explained under the assumption, in accordance with [13], that the magnetic structure of Gd below  $T_{\text{CA}} \sim 20$  K is partially modulated.

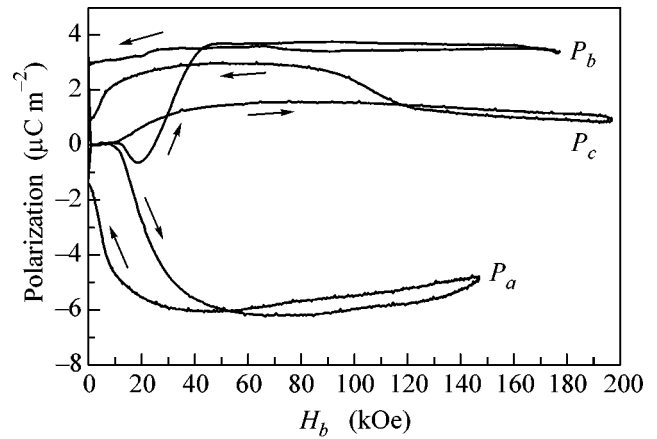


**Fig. 3.** Magnetic-field dependence of the electric polarization along the  $a$ ,  $b$ , and  $c$  axes of the  $\text{GdMnO}_3$  crystal at 5 K upon cooling from  $T_N = 40$  K in an electric field of  $E \sim -1500$  V/cm.

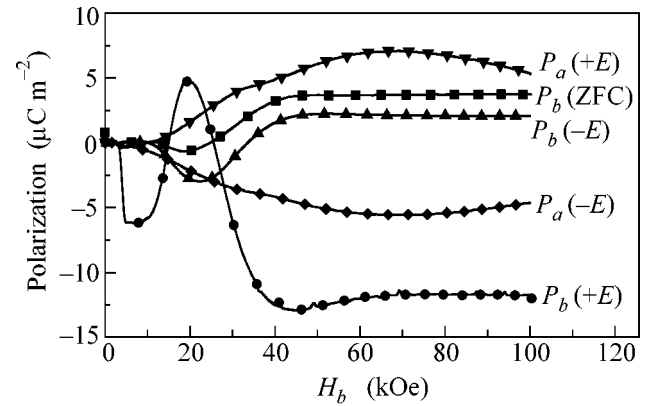


**Fig. 4.** Magnetic-field dependence of the electric polarization along the  $a$  and  $b$  axes of the  $\text{GdMnO}_3$  crystal upon cooling from  $T_N$  in the absence of an electric field (zero-field cooling, ZFC) and at  $E \sim +1500$  (+E) and  $-1500$  (-E) V/cm at 7 K.

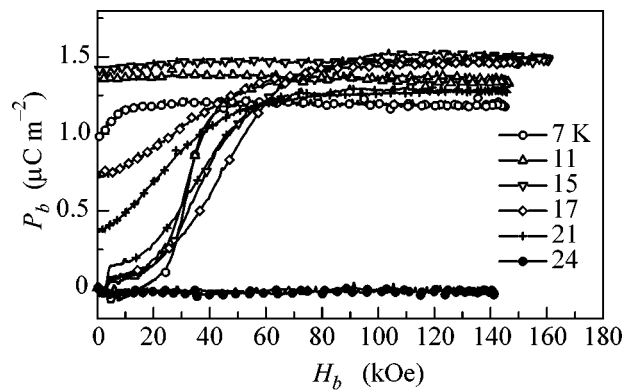


**Fig. 5.** Isotherms of the magnetic-field dependence of the electric polarization along the  $b$  axis for  $H \parallel b$ .

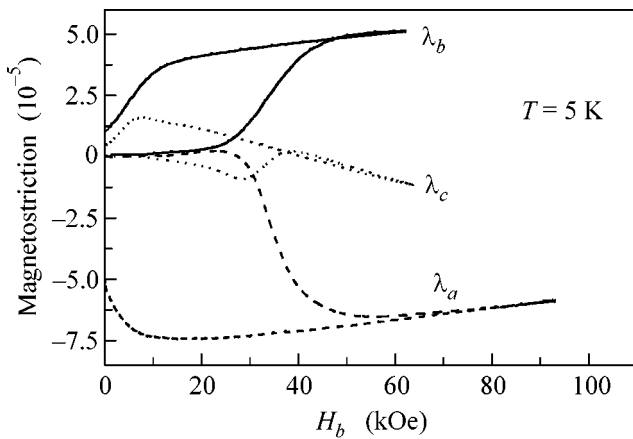


**Fig. 6.** Magnetostriction of GdMnO<sub>3</sub> along the  $a$ ,  $b$ , and  $c$  axes vs. the magnetic field  $H \parallel b$  at 5 K.

At the same time, another scenario cannot be completely excluded. According to this scenario, spontaneous electric polarization in GdMnO<sub>3</sub> is absent in accordance with the data reported in [6], but a magnetic field applied along the  $b$  axis induces a transition to a commensurate modulated structure similar to that observed in TbMnO<sub>3</sub> and DyMnO<sub>3</sub>. Such a structure already allows for the existence of electric polarization. In this case, the dependence of the polarization sign on the direction of the electric field can be tentatively explained by the pinning effects of the sinusoidal incommensurate magnetic structure on various defects. The application of an electric field can induce electric polarization. Upon the switching off of the field, this polarization can be partially retained and can affect the shape of the curves  $P(H)$  at  $T < T_{CA}$ .

As for the physical meaning of the observed threshold fields in the case of magnetization along the direction of the magnetic moments of Mn<sup>3+</sup> ions, it might be suggested (as it was done in [7]) that these fields are due to the spin-flip transition of Mn moments from the  $b$  axis to the  $c$  axis of the crystal. However, the estimation of the magnitude of these fields from the antiferromagnetic resonance frequencies  $\nu_{AFMR}$ , which are approximately the same as in LaMnO<sub>3</sub>, that is,  $\sim 20$  cm<sup>-1</sup> [14], gives  $H_{cr} \approx 200$  kOe. This value substantially exceeds the experimental values. Another possibility is the field-induced transition with a change in the wave vector of the commensurate magnetic structure (in the cases of TbMnO<sub>3</sub> and DyMnO<sub>3</sub> [6]) or, as indicated above, the transition from the canted structure to an incommensurate one (in the case of GdMnO<sub>3</sub>). The latter structure can be ferroelectric and have other components of the electric-polarization vector. The gain in the Zeeman energy due to the large susceptibility of the Mn subsystem along the  $b$  axis in the commensurate phase can favor this transition.

We found that the phase transition in GdMnO<sub>3</sub> mentioned above is accompanied by the occurrence of magnetic-field-induced magnetostrictive strains. The dependences of magnetostriction along the  $a$ ,  $b$ , and  $c$  axes of the crystal on the magnetic field  $H \parallel b$  at a temperature of 5 K are shown in Fig. 6. It is evident that the crystal strain is anisotropic. Such dependences of magnetostriction on the magnetic field were observed over the entire temperature range 5–21 K, and the threshold fields obtained from measurements of magnetostriction and the magnetoelectric effect agree with each other. It should be noted that, in agreement with [6, 8], the ferroelectric transition in the studied RMnO<sub>3</sub> compounds with the perovskite structure is apparently improper. This fact explains its occurrence in crystals with a centrosymmetric paraphase [1].

The difference of the results obtained in this work from the data reported in both [6] and [7] can be explained by the fact that GdMnO<sub>3</sub> is located on the boundary of the existence of the ferroelectric phase; therefore, minor structural features of crystals prepared by different technologies can lead to the occurrence or disappearance of spontaneous electric polarization.

In conclusion, note once again that an anomaly of the dielectric constant along the  $a$  axis of the crystal was observed at  $T_{CA} = 20$  K, where a transition from an incommensurate sinusoidal phase to a canted antiferromagnetic state takes place. At temperatures below  $T_{CA}$ , a change in the electric polarization along the  $a$  and  $b$  axes of the crystal was detected for  $H \parallel b$ . Upon poling the crystal below  $T_N$ , the polarization changed its sign in an electric field, depending on the sign of the electric field. A correlation between magnetoelectric and magnetoelastic properties was found. It was found that GdMnO<sub>3</sub> is a new ferroelectric with the perovskite structure.

We are grateful to V.V. Glushkov for placing the experimental setup at our disposal and for his help in measurements of the dielectric constant, to Z.A. Kazeř for help in the crystallographic orientation of single crystals, and to A.K. Zvezdin for valuable instructions given during the discussion of the results. This work was supported by the Russian Foundation for Basic Research, project nos. 04-02-16592 and 03-02-16445.

## REFERENCES

1. G. A. Smolenskiĭ and I. E. Chupis, *Usp. Fiz. Nauk* **137**, 415 (1982) [*Sov. Phys. Usp.* **25**, 475 (1982)].
2. Yu. N. Venevtsev, G. S. Zhdanov, and S. P. Solov'ev, *Kristallografiya* **5**, 520 (1960) [*Sov. Phys. Crystallogr.* **5**, 504 (1960)].
3. H. Schmid, *Int. J. Magn.* **4**, 337 (1973).
4. N. Hur, S. Park, P. A. Sharma, *et al.*, *Phys. Rev. Lett.* **93**, 107207 (2004).
5. M. Fiebig, Th. Lottermoser, D. Frohlich, *et al.*, *Nature* **419**, 818 (2002).

6. T. Goto, T. Kimura, G. Lawes, *et al.*, Phys. Rev. Lett. **92**, 257201 (2004).
7. T. Kimura, T. Goto, H. Shintani, *et al.*, Nature **426**, 55 (2003).
8. H. Kuwahara, K. Noda, J. Nagayama, and S. Nakamura, in *Proceedings of International Conference on Strongly Correlated Electron Systems* (Karlsruhe, Germany, 2004), p. 124.
9. J. Hemberger, S. L. Lobina, H.-A. Krug von Nidda, *et al.*, Phys. Rev. B **70**, 024414 (2004).
10. A. A. Mukhin, V. Yu. Ivanov, V. D. Travkin, *et al.*, Pis'ma Zh. Éksp. Teor. Fiz. **68**, 331 (1998) [JETP Lett. **68**, 356 (1998)].
11. K. P. Belov, A. K. Zvezdin, A. M. Kadomtseva, and R. Z. Levitin, *Oriental Transitions in Rare-Earth Magnets* (Nauka, Moscow, 1979) [in Russian].
12. Yu. F. Popov, A. M. Kadomtseva, D. V. Belov, *et al.*, Pis'ma Zh. Éksp. Teor. Fiz. **69**, 302 (1999) [JETP Lett. **69**, 330 (1999)].
13. J. Zukrowski, M. Wasniowska, Z. Tarnawski, and K. Krop, Acta Phys. Pol. B **34**, 1533 (2003).
14. A. A. Mukhin, V. Yu. Ivanov, V. D. Travkin, *et al.*, J. Magn. Magn. Mater. **272–276**, 96 (2004).

*Translated by A. Bagatur'yants*

# Isotropic Phase of Nematics in Porous Media<sup>†</sup>

**B. M. Khasanov**

*Department of Physics, Kazan State University, Kazan, 420008 Russia*

*e-mail: bulat.khasanov@ksu.ru*

Received October 14, 2004; in final form, December 8, 2004

We study the effect of random porous matrices on the isotropic–nematic phase transition. Sufficiently close to the cleaning temperature, both random field and thermal fluctuations are important as disordering agents. A novel random field fixed point of the renormalization group equation was found that controls the transition from isotropic to the replica symmetric phase. Explicit evaluation of the exponents in  $d = 6 - \epsilon$  dimensions yields to a dimensional reduction and three-exponent scaling. © 2005 Pleiades Publishing, Inc.

PACS numbers: 61.30.Pq; 64.70.Md

Liquid crystalline ordering in a confined geometry has been the subject of considerable investigation during the past decade. The study of liquid crystals constrained to a random network of porous silica aerogel has been an area of current interest due to their importance in technological applications and from a fundamental point of view. One of the fundamental questions concerns the effect of quenched disorder on the phase transitions. Liquid crystals exhibit a variety of experimentally accessible phase transitions involving orientational and translational ordering. Most of the studies are focused on the nematic–isotropic or nematic–smectic phase transitions. For example, the first has been investigated using various experimental techniques [1]. The main results can be summarized as follows: (a) the bulk isotropic–nematic (I–N) phase-transition temperature is shifted down, and the character of the transition changes; (b) even for above the bulk I–N phase-transition temperature, there exists a weak residual nematic ordering; and (c) Monte Carlo simulations show that, in some cases, the nematic order is replaced by a quasi-long-range nematic phase.

Theoretical modeling of such phenomena is difficult. The porous matrix not only geometrically confines the liquid crystal but also induces a random orienting field that fixes the direction of the order parameter near the surface of the matrix. Some experiments with liquid crystals in random porous media [2] have stimulated a random-field (RF) model for nematic liquid crystal [3] that qualitatively explains the glasslike behavior seen in experiments for liquid crystal–aerogel systems [2, 4–6].

The nematic phase within the pores could be modeled as an Ising-like system with an imposed random field coupled directly to the orientational order parameter to account for the random confinement. Such a model uses a random uniaxial anisotropy in a spin sys-

tem [3, 7], including a symmetric coupling between the anisotropy vector and the order parameter in order to account for the “up–down” nematic symmetry. This RF term in the Hamiltonian of the nematic liquid crystal is linearly coupled to the order parameter. The strength of the random field in this model should directly depend on the anchoring strength of the molecules to the surface of the gel and indirectly on the porosity.

The basic point in discussing the effect of RF on ordered nematic phases follows from the Imry–Ma argument [8, 9], which suggests that this continuous-symmetry system does not have nematic long-range order for dimensions less than four ( $d < 4$ ). The possibility for the nematic phase to be replaced by a glassy state characterized by quasi-long-range order was discussed in [10] and also predicted by numerical simulations [11] and a renormalization-group (RG) approach [12].

The theory in [12] is the first to extend beyond the mean-field approximation for the low-temperature phase of disordered nematics. In this low-temperature phase, uniaxial nematics in random porous media can be mapped onto the RF  $O(N)$  model. However, mapping becomes invalid near the phase transition to the isotropic phase. In this paper, we focus on the effects of quenched disorder that are introduced by the host silica aerogel at the high-temperature phase, i.e., above the I–N phase-transition temperature. An appropriate model would require a full Landau–de Gennes type Hamiltonian incorporating a random orienting field. We carry out the mean-field analysis and RG treatment as well.

The order parameter for a nematic liquid crystal is a three-dimensional symmetric traceless second-rank tensor  $Q_{ij}$ . The effective Landau–de Gennes free-energy

<sup>†</sup>This article was submitted by the author in English.

functional appropriate to the RF nematic model near the I–N phase transition can be written as

$$F = \int d^d x \left\{ \frac{1}{2} r_0 \text{Tr}(Q^2) + \frac{1}{2} \text{Tr}(\nabla Q)^2 - \frac{1}{3} b \text{Tr}(Q^3) + \frac{1}{4} c [\text{Tr}(Q^2)]^2 - \text{Tr}[h(x)Q(x)] \right\}, \quad (1)$$

where  $r_0 = T - T_0$ ,  $T_0$  is the second-order transition temperature if  $b = 0$  (bulk supercooled temperature limit), and  $b$  and  $c$  are temperature-independent constants. The quenched RF  $h_{ij}(x)$  is a symmetric, traceless, Gaussian random tensor with a vanishing quenched average  $[h_{ij}(x)]_{av} = 0$  and with variance [13]

$$\begin{aligned} & [h_{ij}(q)h_{km}(-q)]_{av} \\ &= h_0^2 \left( \frac{1}{2} (\delta_{ik}\delta_{jm} + \delta_{im}\delta_{jk}) - \frac{1}{n} \delta_{ij}\delta_{km} \right), \end{aligned} \quad (2)$$

where  $n$  is the dimensionality of the tensor  $h_{ij}$ .

Ground-state configurations of the longitudinal component of the field  $Q(x)$  (we consider here only the uniaxial nematic) are defined by the saddle-point equation

$$-\Delta Q + r_0 Q - b Q^2 + c Q^3 = h(x). \quad (3)$$

We recall first what behavior is expected for a nematic placed in a nonrandom field, i.e., a homogeneous field in a uniform direction. The isotropic phase acquires some order and is transformed into a paranematic phase. The paranematic–nematic phase transition occurs at  $r_{0c} = (2b^2/9c)(1 + h/2h_c)$ . Here,  $h_c = b^3/27c^2$  is a uniform critical field that determines the nematic–paranematic critical point,  $r_0^+(h_c) = b^2/3c$ . For  $h < h_c$ , the paranematic supercooling temperature  $T_0$  and the nematic overheating temperature  $T^*$  both have field dependence. All three temperatures  $T_0$ ,  $T_c$ , and  $T^*$  merge at the nematic–paranematic critical point  $r_0^+$ . For  $h > h_c$ , the order parameter  $Q$  will increase smoothly as temperature is decreased.

Apparently, the solutions of Eq. (3) with nonhomogeneous  $h(x)$  may essentially depend on a particular configuration of the quenched fields. The effect of RF is averaged over a length scale  $L$ , over which the orientation is correlated. The mean magnitude of the sum of the random fields is given by the sum of the squares of the random fields. Using the central-limit theorem, the effective RF that couples to the local order parameter is approximately  $h_0 L^{-d/2}$ . Now, because the order parameter is changing on a length scale  $L$ , the elastic energy term is of the form  $(Q/L)^2$ . Combining the ideas of Landau and those of Imry and Ma, it was shown that, for low-order parameters  $Q < ch_0/b^2$ , the correlation length

$L$  is about a molecular length scale [7]. The free energy advantage acts as though there were a fixed nematic field on the molecules and thus is negatively linear in  $Q$ . There is an energy cost in changing molecular orientation from point to point, but this is negligible because it is proportional to  $Q^2$ . Thus, for the isotropic phase, the effect in this mean-field consideration is roughly the same whether the imposed field is random or fixed.

Let us estimate under which conditions random fields are relevant and get a dominant contribution for the ground-state configurations. We divide the system into blocks of linear size  $L$ . As we have seen, the characteristic value of the RF in this block (averaged over realization) could be defined by  $h = h_0 L^{-d/2}$ . In the case when the fields can be considered the dominant factor, the order parameter does not depend on the temperature, and this happens for  $h > \tau^{\beta\delta}$ . Here,  $\beta$  and  $\delta$  are the order-parameter critical exponents as a function of temperature and field, respectively. Now, it is easy to estimate the characteristic size of the block up to which the RF can dominate:  $L < h_0^{2/d} \tau^{-2\beta\delta/d}$ . On the other hand, the approximation we are using is correct only on length scales much larger than the fluctuation region  $\xi \propto \tau^{-\nu}$ . Thus, we have another bound for  $L$ :  $L > \xi$ . Therefore, the temperature region where RF effects cannot be ignored is [14]

$$|\tau| < (ch_0^2)^{1/(2\beta\delta - d\nu)} = \tau_h. \quad (4)$$

Such a region of temperatures near  $T_c$  exists only if  $2\beta\delta > d\nu$ . This value of  $\tau_h$  can be interpreted as the estimate for the temperature interval around  $T_c$  in which the order-parameter configurations are essentially defined by the random fields.

In the mean-field theory, using Landau critical exponents, the above nontrivial temperature interval  $\tau_h$  exists only at dimensions  $d < 6$  and equals  $\tau_h = (ch_0^2)^{2/(6-d)}$ . These simple arguments hold only in the approximation where critical fluctuations can be neglected. Thus, the temperature region  $\tau_h$  where disorder induces a finite correlation length  $\xi(h_0) \propto (ch_0^2)^{-1/(6-d)}$  is correct in this regime only.

It is easy to estimate the Ginzburg criterion of the applicability of this approximation. For our model (Eq. (1)), one can get  $\tau_G \propto \max[b^{4/(6-d)}, c^{2/(4-d)}]$ , and the above result is valid only for  $\tau > \tau_G$ . On the other hand, the Ginzburg temperature region is larger than the metastable interval of the first-order I–N phase transition  $\tau_G > b^2/c$ . For weak RF such that  $\tau_h < \tau < \tau_G$ , critical exponents get renormalized by thermal fluctuations, and, in the region  $\tau < \tau_h$ , RF fluctuations are important as well.

The following qualitative arguments may be constructed. Actually, multiple global solutions of saddle-point equation (3) can appear due to the double-well

local potential. This potential has two local minima for  $T_0 < T < T^*$  and for the values of the field  $h < h_c$ . At temperatures above  $T^*$ , the disordered local minima solution is unique. The energy of the nematic solution is higher than the typical energy of the disordered solutions. At further temperature lowering, the interaction of the local minima solutions does not get small. As in spin glasses [15], there are a large number of the disorder-dependent local energy minima. In contrast to the usual spin-glass phase, these minima are probably separated by finite energy barriers. In this state, the standard nematic order parameter equals zero,  $[\langle Q \rangle]_{av} = 0$ . Therefore, it is possible to expect the existence of a finite-temperature interval between the isotropic and nematic phases where the glass-type behavior occurs, rather than the real spin-glass phase. At the same time, the application of an external magnetic field  $H$  restores the long-range orientational order, and the magnetic-field threshold is determined from the condition that the nematic coherence length  $\xi_H \propto H^{-1}$  is less than the disorder-induced correlation length  $\xi(h_0)$ .

In the glass-type phase, the thermodynamics is defined by numerous disorder-dependent local energy minima. The most developed technique in this case is the Parisi replica-symmetry-breaking method [16]. Using this technique, it has been proven that, for the  $N$ -component ( $N \gg 1$ ) spin systems with RF, the usual scaling replica-symmetry solution is unstable with respect to the replica symmetry breaking at the phase-transition point. Moreover, it turns out that the spin-glass transition, which is believed to take place at the replica-symmetry-breaking temperature, always precedes the low-temperature phase and obeys the equation  $\tau_{RSB} \propto (h_0^2)^{4/(6-d)}$  [17]. If we compare  $\tau_{RSB}$  with a RF-controlled temperature region  $\tau_h$ , we see that  $\tau_h > \tau_{RSB}$ .

Now, we consider the disordered I–N model, defined by Eq. (1), within the high-temperature, i.e., isotropic, phase. We assume the existence of rather strong fluctuations of the order parameter in the isotropic phase near the I–N transition, for which experimental evidence exists [18]. The Landau–de Gennes Hamiltonian has cubic and quartic interaction terms and the RF term; therefore, there are three length scales in the fluctuation theory:  $\xi_c \propto c^{-1/(4-d)}$ ,  $\xi_b \propto (b^2)^{-1/(6-d)}$ , and  $\xi_h \propto (ch_0^2)^{-1/(6-d)}$ .

Let us remove the fast modes and rewrite the Hamiltonian in terms of the block order parameter corresponding to the scale  $L = al$ . Here,  $a$  is the ultraviolet cutoff and  $l > 1$ . Then, we rescale in such a way that the Hamiltonian would be restored to its initial form with new constants  $b(L)$ ,  $c(L)$ , and  $h_0(L)$ . Dimensional analysis provides the estimates

$$\begin{aligned} b(L) &= l^{(6-d)/2} b(a), & c(L) &= l^{4-d} c(a), \\ h_0(L) &= l h_0(a). \end{aligned} \quad (5)$$

If one considers the combination  $\Delta = ch_0^2$  as a new parameter, we immediately get

$$\Delta(L) = l^{6-d} \Delta(a). \quad (6)$$

Iteration until  $\Delta(L_0) = 1$  yields  $L_0 = \xi_h$ , i.e., the length scale beyond which the RF fluctuations are significant. The same arguments are true for the order-parameter fluctuations coming from the cubic term in (1). The quartic term is an irrelevant variable in the RG sense. Hence, the two length scales are important for IN phase transition near  $d = 6$ . Thus, we interpret this result physically by noting that, sufficiently close to  $T_c$ , the dominant disordering agent is not the RF only, but also the thermal fluctuations caused by cubic interaction. Using the RG method for disordered systems, recursion relations are established for the parameters of the effective replica Hamiltonian. Then, replica symmetry is assumed and the RG equations become simple functions of replica number. In that respect, the use of replica is a trick of diagram counting. One can generally establish identical RG equations directly by considering disorder correlation functions, a method that is usually called replica-symmetry perturbation theory. After standard RG transformations, the one-loop equations in differential form are the following:

$$\frac{dr}{d \ln L} = (2 - \eta)r - \frac{7}{6}b^2(1 - 2r) + 7\Delta(1 - 2r), \quad (7)$$

$$\frac{d \ln b^2}{d \ln L} = \varepsilon - 3\eta - b^6 - 24\Delta, \quad (8)$$

$$\frac{d \ln \Delta}{d \ln L} = \varepsilon - 3\eta + \frac{22}{3}b^2 - 26\Delta. \quad (9)$$

Here, we set  $n = 3$  for a nematic liquid crystal, and  $\varepsilon = 6 - d$ .

The exponent  $\eta$  determines the behavior of the two-point correlation function  $G(q)$ , which is defined by means of the relation

$$\begin{aligned} G(q) &= [\langle Q(q)Q(-q) \rangle]_{av} \\ &\quad - [\langle Q(q) \rangle \langle Q(-q) \rangle]_{av}. \end{aligned} \quad (10)$$

At the critical point,  $G(q)$  diverges as  $q^{\eta-2}$ , and, to the lowest order in the perturbation expansion,

$$\eta = 7b^2/18. \quad (11)$$

We find that the fixed points  $\mu(b^2, \Delta)$  of the RG equations are given by  $\mu_0(0, 0)$ ,  $\mu_b(6\varepsilon/13, 0)$ ,  $\mu_\Delta(0, \varepsilon/26)$ , and  $\mu^*(6\varepsilon/613, 25\varepsilon/613)$ . The RG flow diagram in the  $(b^2, \Delta)$  plane is illustrated in the figure.

In addition to the trivial Gaussian fixed point  $\mu_0$ , these equations possess three nontrivial fixed points. The fixed point  $\mu_b$  describes the critical behavior of the pure nematic, and the coefficient  $r$  at this point is

greater than zero. Thus, the fixed-point Hamiltonian has a minima at  $Q = 0$  and at  $Q \approx b/c$ . The first-order transition occurs if the order parameter falls into the latter deep minimum. It is likely that the  $\mu_b$  fixed point corresponds to the critical fluctuations about the metastable minimum at  $Q = 0$  [19]. The fixed point  $\mu_\Delta$  is exactly the RF Heisenberg fixed point for the five-component  $O(N)$  model, and it describes the RF behavior at the isolated Landau point on the phase diagram, where  $b = 0$  [20]. All the above fixed points are unstable.

The only stable fixed point is  $\mu^*$ , which controls the behavior of the relevant parameters of the Hamiltonian below six dimensions and corresponds to the replica-symmetric phase with an infinite correlation length.

Let us now determine the critical exponents associated with the fixed point  $\mu^*$ . The correlation-length exponent  $\nu$  follows directly from Eq. (7):

$$\nu^{-1} = 2 + \frac{35}{18}b^2 - 14\Delta. \quad (12)$$

Using RG iterations and the perturbation expansion for the two-point correlation function, one can obtain the susceptibility exponent

$$\gamma = 1 - \frac{7}{6}b^2 + 7\Delta. \quad (13)$$

The specific-heat exponent  $\alpha$  can be calculated from a singular part of the free energy

$$F_s \propto \int_0^{l^*} \ln(1 + \tilde{r}(l)) e^{-dl},$$

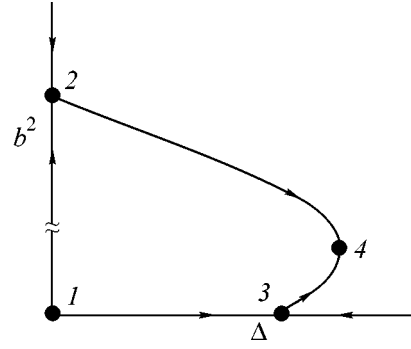
where  $\tilde{r}(l)$  is the coefficient of the  $Q^2$  term in the Hamiltonian averaged over the distribution of the RF and  $l^* = \ln \xi$ . Evaluating the above integral to leading order, we find  $F_s \propto \tau^{2-\alpha}$ , where

$$\alpha = \frac{6-d}{2} + \frac{7}{4}b^2 - 14\Delta. \quad (14)$$

Equations (11)–(14) yield the usual ‘‘thermodynamic’’ scaling law  $\gamma = \nu(2 - \eta)$  and the modified hyperscaling law  $2 - \alpha = \nu(d - \theta)$  with the ‘‘violation of hyperscaling’’ exponent  $\theta = 2 - \eta$ . This result is valid to first order in  $\epsilon$ .

In the presence of the RF, the quantity  $[\langle Q(0)\langle Q(x) \rangle]_{av}$  is nonzero even in phases where  $[\langle Q(x) \rangle]_{av}$  vanishes. There are, therefore, two distinct correlation functions to consider. The first is the analog of usual connected correlation function  $G$  (10), and the second is the disconnected function and is specific for random systems. It measures the fluctuations in the local quenched order parameter,

$$C_s(q) = [\langle Q(q)\langle Q(-q) \rangle]_{av} - [\langle Q(q) \rangle]_{av} [\langle Q(-q) \rangle]_{av}, \quad (15)$$



Phase diagram of the RG equations. Points 1, 2, 3, and 4 stand for the fixed points  $\mu_0$ ,  $\mu_b$ ,  $\mu_\Delta$ , and  $\mu^*$ , respectively.

and diverges at small  $q$  as  $C_s \propto q^{\tilde{\eta}-4}$ .

Near  $T_c$ , we can write  $C_s(q) = G^2(q)D(q)$  [21], where  $D(q)$  is related to a dressed spectral function  $h_0^2(q)$  of the RF fluctuations. If  $h_0^2(q) \propto q^{-\lambda_\Delta}$  for  $q\xi \gg 1$ , then one obtains  $C_s(q) \propto q^{2\eta-4-\lambda_\Delta}$  and  $\tilde{\eta} = 2\eta - \lambda_\Delta$ . Note that the choice  $\lambda_\Delta = 0$  yields  $\tilde{\eta} = 2\eta$ , a value that is on the limit of the exact inequality  $\tilde{\eta} \leq 2\eta$  that is due to [22]. Another relation was suggested by consideration of the RF contribution to the free energy in a correlation volume that scales as  $\xi^\theta$ . In contrast, for the pure system, the characteristic scale of variation of the effective free energy is simply set by the thermal fluctuations, i.e.,  $\propto T$ . On the other hand, if the local order parameter were uncorrelated with the RF, this would scale as  $\xi^{d/2-\beta/\nu}$ . Here, the factor  $\xi^{d/2}$  comes from the scaling of the total RF. The relation for  $\beta$  is easy to find from scaling the disconnected correlation function in a real space  $2\beta = (d - 4 + \tilde{\eta})\nu$ . Since the correlations could be included by an additional factor  $\xi^{\lambda_\Delta/2}$ , corresponding to  $h_0^2(q) \propto \xi^{\lambda_\Delta}$  for  $q\xi \ll 1$ , we expect that  $\theta = 2 - \eta + \lambda_\Delta$ . The case  $\lambda_\Delta = 0$  yields  $\theta = 2 - \eta$ , which is on the limit of another inequality, namely,  $\theta \geq 2 - \eta$  [23]. Thus, for the hyperscaling-violation exponent, we recover the result  $\theta = 2 + \eta - \tilde{\eta}$  [14, 17, 23, 24].

In one-loop calculations, the critical exponent  $\eta$  is determined by (11), and  $\tilde{\eta} = 2\eta$ . The  $\Delta$ -dependent terms appear in  $C_s(q)$  only in the two-loop diagrammatic expansion for  $D(q)$ ,

$$D(q) = h_0^2 \left( 1 + \frac{7}{3}\Delta(b^2 - 6\Delta)\ln q \right), \quad (16)$$

and, now, the particular value  $\lambda_\Delta = (7/3)\Delta(6\Delta - b^2)$  is nonzero to second order in  $\epsilon$ . All diagrams in (16) must be disconnected before averaging over the RF distribution.

Formally, we can divide the diagrams contributing to  $G(q)$  and write  $\eta = \eta_1(b^2) + \eta_2(\Delta^2, b^2\Delta)$ . In the one-loop approximation,  $\eta_2 = 0$  and  $\eta_1$  is given by (11). A straightforward evaluation of the RF-dependent diagrams leads to the expression  $\eta_2 = \lambda_\Delta$ . This means that, for the hyperscaling-violation exponent, we get  $\theta = 2 - \eta_1$ . In contrast to the disconnected correlation function, all diagrams here are connected before configuration averaging, and not all of them are treelike diagrams, as is the case for the  $O(N)$  model.

More generally, in the vicinity of the fixed point  $\mu^*$ , the random correlation function is proportional to  $c^{-1}$  for small  $c$ . Therefore, in the critical region, one expects that the random correlation function will scale as  $C_s(q, \xi, c) = c^{-1} e^{(2-\eta-\lambda_c)l} C_s(e^l q, e^{-l} \xi)$ , where  $\lambda_c$  is the scaling exponent of the irrelevant parameter  $c$ . For  $q = 0$ , one has the behavior  $C_s(0, \tau) \propto \tau^{-\tilde{\gamma}}$ , with  $\tilde{\gamma} = \nu(2 - \eta - \lambda_c)$ . Using the relation  $\tilde{\gamma} = \nu(4 - \tilde{\eta})$  that follows from the scaling at small  $q$  and  $\tau = 0$ , we can write  $\lambda_c = \tilde{\eta} - \eta - 2$ . We see that  $\lambda_c = -\theta$ . This result is quite obvious. Really, on the other hand, the perturbation expansion for free energy is a double power series in  $b^2$ ,  $c$ , and  $h_0^2$ . The first terms in this series behave like  $b^2 h_0^2$  and  $ch_0^4$ , or, for large  $h_0^2$ , they both are proportional to  $h_0^2$  as well. Thus, for the free-energy density, we have  $F(h_0^2, \tau) = \tau^{\nu d} f(h_0^2 \tau^{-\phi})$ , where  $\phi$  is the crossover exponent. If we conclude that  $f$  is a linear function of its argument for small  $\tau$ , as follows from the perturbation expansion, one can get  $F(h_0^2, \tau) \propto \tau^{\nu(d-\phi/\nu)}$ ; hence,  $\theta = \phi/\nu$ . The crossover exponent is related to the scaling of the RF near the fixed point  $\mu^*$ :  $h_0^2$  increases as  $\exp(l\phi/\nu)$ . Writing the recursion relation for  $h_0^2$  up to two-loop order, as we have done (Eq. (16)), we again find  $\phi/\nu = 2 - \eta + \lambda_\Delta = 2 - \eta_1$ .

All of our results for critical exponents suggest that  $\tilde{\eta} \neq 2\eta$ , in agreement with the three-exponent scaling picture [23, 24]. For example, the exponent scaling gives the ratio  $C_s(0)/G^2(0) \propto \xi^{\lambda_\Delta}$ , which would diverge unless  $2\eta = \tilde{\eta}$  is valid. However, this divergence is too weak to be detected, and, thus, this ratio may be concerned as a constant, and the concept of no self-averaging in RF systems is expected [25].

We have considered the effects of a RF (field conjugate to the order parameter) on an I–N phase transition using the  $\varepsilon = 6 - d$  expansion method. We have found the novel RF fixed point that proceeds from the existence of two relevant variables in the RG approach. The first involves the effects of the RF, while the latter involves those of thermal disorder. These two agents of disorder give comparable contributions to the problem.

In the pure nematic, when  $h_0 = 0$ , the zero cubic term means that the system is located at an isolated Landau point at the phase diagram [20]. This point is unstable with respect to  $b$ . When nonzero  $h_0$  is switched on,  $\Delta$  is renormalized towards a fixed point  $\mu^*$ , and all critical exponents are changed. We believe that this fixed point governs the critical behavior at the transition from isotropic to the replica-symmetric phase that precedes the replica-symmetry-breaking phase. The location of this nontrivial random fixed point on a phase diagram is quite close to the fixed point  $\mu_\Delta$  with zero cubic term (we may call this point a random isolated Landau point). This indicates that the critical behavior of the isotropic nematic in RF is like the behavior of the RF Heisenberg model for the five-component order parameter. Independent calculation of the critical exponents shows that the dimensional reduction in the hyperscaling relations for the RF isotropic nematic contain the shifted value  $d - 2 - \eta + \tilde{\eta}$  instead of  $d$ . The so-called “three-exponent scaling” appears in second order in  $\varepsilon$ . A model for studying the replica-symmetry-breaking transition from the replica-symmetric phase is clearly necessary to perform further investigations.

I would like to thank Prof. J. Stevens for his kind hospitality at the University of North Carolina at Asheville, which enabled completion of the present work.

## REFERENCES

1. *Liquid Crystals in Complex Geometries*, Ed. by G. P. Crawford and S. Zumer (Taylor and Francis, London, 1996).
2. X.-I. Wu, W. I. Goldberg, M. X. Liu, and J. Z. Xue, *Phys. Rev. Lett.* **69**, 470 (1992); T. Bellini, N. A. Clark, and D. W. Schaefer, *Phys. Rev. Lett.* **74**, 2740 (1995).
3. A. Maritan, M. Cieplak, T. Bellini, and J. R. Banavar, *Phys. Rev. Lett.* **72**, 4113 (1994); A. Maritan, M. Cieplak, and J. R. Banavar, in *Liquid Crystals in Complex Geometries*, Ed. by G. P. Crawford and S. Zumer (Taylor and Francis, London, 1996), Chap. 22.
4. K. Uzelac, A. Hasmy, and R. Jullien, *Phys. Rev. Lett.* **74**, 422 (1995).
5. G. S. Iannacchione, S. Qian, D. Finotello, and F. M. Aliev, *Phys. Rev. E* **56**, 554 (1997).
6. A. Mertelj and M. Copic, *Phys. Rev. E* **55**, 504 (1997).
7. D. J. Cleaver, S. Kralj, T. J. Sluckin, and M. P. Allen, in *Liquid Crystals in Complex Geometries*, Ed. by G. P. Crawford and S. Zumer (Taylor and Francis, London, 1996), Chap. 21.
8. Y. Imry and S. K. Ma, *Phys. Rev. Lett.* **35**, 1399 (1975).
9. E. I. Kats, *JETP Lett.* **65**, 725 (1997).
10. L. Radzihovsky and J. Toner, *Phys. Rev. Lett.* **79**, 4214 (1997).
11. J. Chakrabarti, *Phys. Rev. Lett.* **81**, 385 (1998).
12. D. E. Feldman, *Phys. Rev. Lett.* **84**, 4886 (2000).
13. N. Uchida, *Phys. Rev. E* **60**, R13 (1999).

14. T. Nattermann, in *Spin Glasses and Random Fields*, Ed. by A. P. Young (World Sci., Singapore, 1998), p. 277; cond-mat/9705295.
15. M. Mezard, G. Parisi, and M. Virasoro, *Spin-Glass Theory and Beyond* (World Sci., Singapore, 1987); Vik. Dot-senko, Phys. Usp. **38** (5), 1 (1995).
16. G. Parisi, J. Phys. A **13**, 1101 (1980).
17. C. De Dominicis, H. Orland, and T. Temesvari, J. Phys. I **5**, 987 (1995).
18. P. G. de Gennes and J. Prost, *The Physics of Liquid Crystals*, 2nd ed. (Clarendon, Oxford, 1993; Mir, Moscow, 1982).
19. R. G. Priest and T. C. Lubensky, Phys. Rev. B **13**, 4159 (1976).
20. P. B. Vigman, A. I. Larkin, and V. M. Filev, Sov. Phys. JETP **41**, 944 (1976).
21. G. Grinstein, Phys. Rev. Lett. **37**, 944 (1976).
22. M. Schwartz and A. Soffer, Phys. Rev. Lett. **55**, 2499 (1985).
23. D. Fisher, Phys. Rev. Lett. **56**, 416 (1986).
24. J. Villain, J. Phys. (Paris) **46**, 1843 (1985).
25. A. Aharony and A. B. Harris, Phys. Rev. Lett. **77**, 3700 (1996).

## Resonant Raman Scattering in GeSi/Si Superlattices with GeSi Quantum Dots

A. G. Milekhin<sup>1</sup>, A. I. Nikiforov<sup>1</sup>, O. P. Pchelyakov<sup>1</sup>, A. G. Rodrigues<sup>2</sup>,  
J. C. Galzerani<sup>2</sup>, and D. R. T. Zahn<sup>3</sup>

<sup>1</sup> *Institute of Semiconductor Physics, Siberian Division, Russian Academy of Sciences,  
pr. Akademika Lavrent'eva 13, Novosibirsk, 630090 Russia  
e-mail: milekhin@thermo.isp.nsc.ru*

<sup>2</sup> *Departamento de Fisica, Universidade Federal de Sao Carlos, C.P. 676, Sao Carlos, SP, Brasil*

<sup>3</sup> *Institut für Physik, Technische Universität Chemnitz, D 09107 Chemnitz, Germany*

Received November 29, 2004

The resonant Raman scattering in GeSi/Si structures with GeSi quantum dots has been analyzed. These structures were formed at various temperatures in the process of molecular-beam epitaxy. It has been shown that Raman scattering spectra recorded near resonances with the  $E_0$  and  $E_1$  electronic transitions exhibit the lines of Ge optical phonons whose frequencies differ significantly from the corresponding values in bulk germanium. In the structures grown at low temperatures (300–400°C), the phonon frequency decreases with increasing excitation energy. This behavior is attributed to Raman scattering, which is sensitive to the size of quantum dots, and shows that quantum dots are inhomogeneous in size. In the structures grown at a higher temperature (500°C), the opposite dependence of the frequency of Ge phonons on excitation energy is observed. This behavior is attributed to the competitive effect of internal mechanical stresses in quantum dots, the localization of optical photons, and the mixing of Ge and Si atoms in structures with a bimodal size distribution of quantum dots. © 2005 Pleiades Publishing, Inc.

PACS numbers: 63.22.+m; 78.67.Hc; 78.30.Am

Owing to new physical properties and compatibility with well-developed silicon technology, structures with Ge/Si self-assembled quantum dots have large potential for application as an element base of photoreceivers and light-emitting devices [1–6], nonlinear optical devices [7], memory devices [8], and lasers [9]. It is obvious that the production of such devices imposes stringent requirements on the technology of the formation and structure parameters of quantum dots (such as size, shape, content, stresses in quantum dots, etc.), which determine their energy spectrum. The understanding of the vibrational properties of quantum dots is important both for studying the fundamental properties (electron–phonon scattering and heat conductivity) of new physical objects and for applications, because the vibrational spectrum of quantum dots carries information on their structural properties. The Raman scattering is the most informative method for studying the vibrational properties of structures with Ge quantum dots. Acoustic [10–13] and optical [13–18] phonons in Ge quantum dots of various sizes and shapes were studied. Recently, we reported the observation of resonant Raman scattering sensitive to the size of quantum dots in multilayer structures with Ge quantum dots of the pyramidal shape (“hut” cluster) [19].

In this work, we present the results of studying the Raman scattering in structures with Ge/Si quantum

dots, which are formed in a wide range of growth temperatures and have various structural and optical properties. Four samples, denoted as T300, T400, T500, and T600, were sequentially grown by the process of molecular-beam epitaxy in the Stranski–Krastanov growth regime at Ge deposition temperatures of 300, 400, 500, and 600°C, respectively, on Si substrates oriented in the (001) direction. The temperature of the growth of Si layers was equal to 800 and 500°C before and after the Ge deposition, respectively. The structures consisted of five sequentially repeated pairs of Ge and Si quantum-dot layers with a nominal thickness of 1.4 and 50 nm, respectively. The scattering of light was studied at a temperature of 8 K upon excitation by 457.8–630.1 nm light from a laser that was based on Rhodamine 6G dyes and pumped by an Ar<sup>+</sup>Kr<sup>+</sup> laser. The Raman spectra were recorded by means of a T64000 triple monochromator in the backscattering geometry.

As is well known, the Raman spectra for structures with GeSi quantum dots exhibit three main lines at frequencies 300–320 and near 420 and 525 cm<sup>-1</sup>, corresponding to Ge–Ge, Ge–Si, and Si–Si optical vibrations (longitudinal optical phonons), respectively [14–19]. Moreover, weaker lines can be observed near 300 and 510 cm<sup>-1</sup>, which are attributed to the contributions

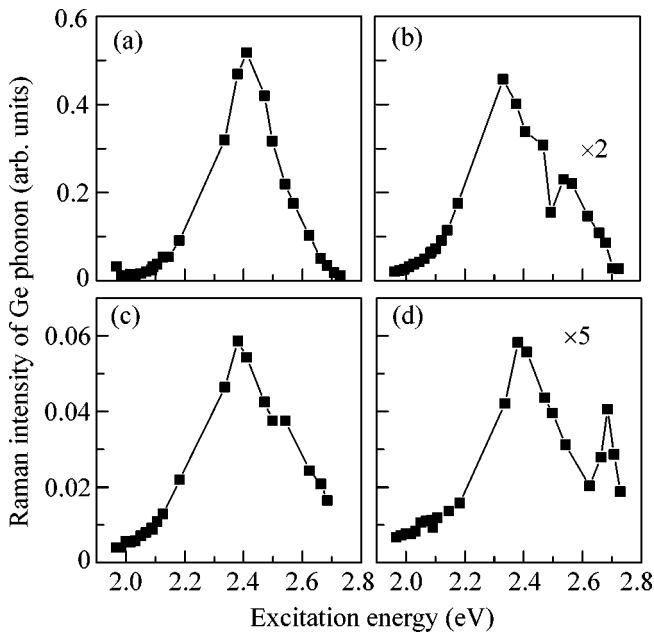


**Fig. 1.** Intensity of the Raman scattering line of the Ge–Ge vibrational mode vs. laser excitation energy for the structures (a) T300, (b) T400, (c) T500, and (d) T600.

of second-order scattering ( $2TA_{Si}$ ) and Si–Si local vibrations [20], respectively.

We consider in more detail Ge–Ge optical vibrations localized in quantum dots. Three physical phenomena competitively affect the frequencies of these phonons: internal mechanical stresses (a high-frequency shift corresponds to them), mixing of Ge and Si atoms in quantum dots, and the localization of optical phonons (both effects induce low-frequency shift) [12–19]. Figure 1 shows the results obtained in the experiments on the resonant Raman scattering for the samples under investigation. This figure presents the intensity of the signal of longitudinal optical phonons in germanium, which was normalized to the intensity of the Si–Si signal for each spectrum, as a function of laser excitation energy. As is seen in the figure, the resonance profile has a wide maximum near 2.4 eV for all structures. Samples grown at higher temperatures (T400 and T500) exhibit an asymmetric high-frequency shoulder, and the resonance profile of the T600 sample has an additional maximum near 2.68 eV.

The behavior of the frequencies of longitudinal optical phonons in germanium as a function of excitation energy seems to be important (Fig. 2). The frequency of longitudinal optical phonons in germanium for the T300 and T400 samples decreases with increasing excitation energy (from 2.5 to 2.7 eV). This shift is equal to 4–5  $\text{cm}^{-1}$  and corresponds to a value observed previously for samples similar to the T300 sample [11, 13]. At the same time, an increase in the phonon frequency for the T500 sample from 308 to 316  $\text{cm}^{-1}$  is simultaneously observed. The frequency of longitudinal opti-

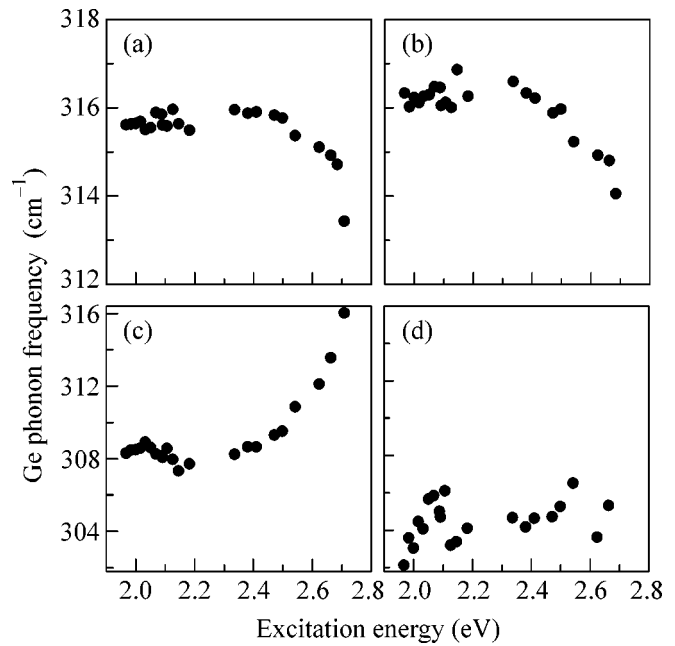


**Fig. 2.** Frequency of the Ge–Ge optical vibrational modes in quantum dots vs. laser excitation energy for the structures (a) T300, (b) T400, (c) T500, and (d) T600.

cal phonons in germanium for the T600 sample remains constant at 305  $\text{cm}^{-1}$ .

The large FWHM value of the resonance profile (up to 0.2 eV) for the T300 and T400 samples implies the presence of contributions from several electron resonances. First, the energy of  $E_1$  transitions in stressed Ge quantum dots is equal to 2.39 eV, which is higher than its bulk value by 0.16 eV [21]. Second, the energy of  $E_0$  resonance in the wetting Ge layer is equal to 2.0–2.2 eV [22]. Therefore, electronic transitions in the wetting layer can also contribute to the Raman scattering to become process. Third, the energy of  $E_0$  transitions in quantum dots can reach 2.4–2.6 eV, which allows for the resonant Raman scattering to become sensitive to the size of quantum dots. The Raman scattering by small quantum dots for which the energy of  $E_0$  transitions is higher appears to be resonantly enhanced when the energy of the exciting laser coincides with the energy of localized electron states. The effect of the localization of optical phonons is much larger for small quantum dots, which is manifested in a decrease in the frequency of optical phonons in the spectra of the Raman scattering (Fig. 2) that are excited by higher laser energies (2.5–2.7 eV). The direction of the phonon-energy shift is determined by the negative dispersion of optical phonons in germanium [23]. Mixing of atoms in quantum dots in the T300 and T400 samples is insignificant (the Si content is no more than 15–20%) [16] and does not lead to considerable change in electronic transitions.

Quantum dots in the T500 and T600 samples form a GeSi solid solution, where Si content reaches 33 and

47%, respectively, and quantum dots have sizes 25–100 nm [16]. For such compositions, Cerdeira *et al.* [24] determined that the energies of  $E_1$  transitions in  $\text{Ge}_x\text{Si}_{1-x}/\text{Si}$  superlattices are equal to 2.6 and 2.7 eV, respectively, which agrees well with the energy positions of the shoulder observed near 2.6 eV and the additional peak for the T600 sample (2.68 eV). At growth temperatures of 300–400°C, small stressed quantum dots in which the localization effect is large are formed. For this reason, the frequencies of phonons in quantum dots are determined by the above-discussed Raman scattering sensitive to the size of quantum dots [11]. A small increase in the frequency of longitudinal optical phonons in Ge quantum dots for the T400 sample (about  $1\text{ cm}^{-1}$ ) as compared to the corresponding value for the T300 sample can apparently be attributed to an increase in the mean size of quantum dots with an increase in the growth temperature, which is observed in experiments with high-resolution electron microscopy [16]. A further increase in the growth temperature leads to intense mixing of Ge and Si atoms, which must lead to a decrease in the Ge–Ge vibrational frequency (near  $308\text{ cm}^{-1}$ ) for the T500 sample. This behavior is observed in the spectra of the Raman scattering at relatively low laser excitation energies (up to 2.4 eV) but does not explain an increase in the phonon frequency (up to  $316\text{ cm}^{-1}$ ) with increasing excitation energy up to 2.7 eV.

Such a behavior of the phonon frequency as a function of excitation energy can be attributed to the bimodal character of the size distribution of quantum dots, which is typical for samples grown at temperatures near 500°C [25]. With an increase in the growth temperature, the density of small stressed quantum dots (hut clusters) decreases, whereas the density of partially relaxed large GeSi quantum dots increases. At a growth temperature of 500°C, the contribution from the quantum dots of the GeSi solid solution becomes considerable, which leads to a decrease in the phonon frequency ( $308\text{ cm}^{-1}$ ) compared to the stressed state ( $316\text{ cm}^{-1}$ ). However, with increasing laser excitation energy (above 2.4 eV), the hut clusters make the resonant contribution to the Raman scattering, which leads to an increase in the phonon frequency to a value corresponding to the stressed state in the hut clusters. In the structures grown at a higher temperature (600°C), the density of the hut clusters decreases significantly. As a result, the contribution of large relaxed GeSi quantum dots to the Raman scattering prevails at all laser excitation energies, and the vibrational frequency remains constant near  $305\text{ cm}^{-1}$ . The intensity of the vibrational modes of quantum dots in the solid solution increases additionally due to the 2.68-eV resonance (Fig. 2d). We emphasize that the intensity of resonance curves for the T300 and T400 samples decreases with an increase in the growth temperature. This dependence may be attributed both to a decrease in the density of quantum dots with an increase in the temperature and to a

decrease in the intensity of Raman scattering by Ge–Ge vibrational modes in GeSi solid solutions.

Thus, a nonmonotonic behavior of the frequency of Ge–Ge vibrational modes as a function of laser excitation energy has been found for GeSi/Si structures grown in a wide temperature range. At low growth temperatures (300–400°C), the mode frequencies are determined by internal mechanical stresses and by the localization of optical phonons. At a higher growth temperature (500°C), the bimodal size distribution of quantum dots plays a considerable role. At low laser excitation energies, the phonon frequencies are determined by the contribution from large relaxed GeSi quantum dots, whereas small stressed quantum dots make the resonant contribution to the Raman scattering at high energies. With a further increase in the growth temperature, the density of small quantum dots decreases, and the phonon frequencies are independent of excitation energy and are completely determined by the effect of the mixing of atoms in quantum dots.

This work was supported by the Russian Foundation for Basic Research, project no. 02-02-17746.

## REFERENCES

1. R. A. Mezger, *Semicond. Comp.* **1**, 21 (1995).
2. U. Konig, *Phys. Scr. T* **68**, 90 (1996).
3. R. A. Soref, *Thin Solid Films* **294**, 325 (1997).
4. T. Tashiro, T. Tatsumi, M. Sugiyama, *et al.*, *IEEE Trans. Electron Devices* **44**, 545 (1997).
5. D. J. Paul, *Thin Solid Films* **321**, 172 (1998).
6. S. Janz, J.-M. Baribeau, D. J. Lockwood, *et al.*, *J. Vac. Sci. Technol. A* **18** (2), 588 (2000).
7. Y. E. Jie, Y. N. Xiong, A. T. S. Wee, *et al.*, *Appl. Phys. Lett.* **77**, 3926 (2000).
8. W. K. Choi, W. K. Chim, C. L. Heng, *et al.*, *Appl. Phys. Lett.* **80**, 2014 (2002).
9. J. L. Liu, G. Jin, Y. S. Tang, *et al.*, *Appl. Phys. Lett.* **76**, 586 (2000).
10. M. Cazayous, J. R. Huntzinger, J. Groenen, *et al.*, *Phys. Rev. B* **62**, 7243 (2000).
11. A. G. Milekhin, A. I. Nikiforov, O. P. Pchelyakov, *et al.*, *Pis'ma Zh. Éksp. Teor. Fiz.* **73**, 521 (2001) [*JETP Lett.* **73**, 461 (2001)].
12. A. Milekhin, N. P. Stepina, A. I. Yakimov, *et al.*, *Appl. Surf. Sci.* **175–176**, 629 (2001).
13. A. Milekhin, D. Tenne, and D. R. T. Zahn, in *Quantum Dots and Nanowires*, Ed. by S. Bandyopadhyay and H. S. Nalwa (Am. Sci., Stevenson Ranch, Calif., 2003), p. 375.
14. N. V. Vostokov, S. A. Gusev, I. V. Dolgov, *et al.*, *Fiz. Tekh. Poluprovodn. (St. Petersburg)* **34**, 8 (2000) [*Semiconductors* **34**, 6 (2000)].
15. A. G. Milekhin, A. I. Nikiforov, O. P. Pchelyakov, *et al.*, *Physica E (Amsterdam)* **13/2–4**, 982 (2002).
16. A. G. Milekhin, A. I. Nikiforov, M. Yu. Ladanov, *et al.*, *Physica E (Amsterdam)* **21/2–4**, 464 (2004).

17. M. Ya. Valakh, R. Yu. Holiney, V. N. Dzhagan, *et al.*, Fiz. Tverd. Tela (St. Petersburg) **47**, 54 (2005) [Phys. Solid State **47**, 54 (2005)].
18. P. H. Tan, D. Bougeard, G. Abstreiter, *et al.*, Appl. Phys. Lett. **84**, 2632 (2004).
19. A. G. Milekhin, A. I. Nikiforov, M. Yu. Ladanov, *et al.*, Fiz. Tverd. Tela (St. Petersburg) **46**, 94 (2004) [Phys. Solid State **46**, 92 (2004)].
20. M. I. Alonso and K. Winer, Phys. Rev. B **39**, 10056 (1989).
21. S. H. Kwok, P. Y. Yu, C. H. Tung, *et al.*, Phys. Rev. B **59**, 4980 (1999).
22. R. Schorer, G. Abstreiter, S. de Gironcoli, *et al.*, Phys. Rev. B **49**, 5406 (1994).
23. C. Trallero-Giner, A. Debernardi, M. Cardona, *et al.*, Phys. Rev. B **57**, 4664 (1998).
24. F. Cerdeira, A. Pinczuk, and J. C. Bean, Phys. Rev. B **31**, 1202 (1985).
25. J. Drucker, IEEE J. Quantum Electron. **38**, 975 (2002).

*Translated by R. Tyapaev*

## Orientalional Effect of the Texture of a Carbon-Nanotube Film on $CK_{\alpha}$ Radiation Intensity

A. V. Okotrub<sup>1</sup>, S. B. Dabagov<sup>2,3</sup>, A. G. Kudashov<sup>1</sup>, A. V. Gusel'nikov<sup>1</sup>, I. Kinloch<sup>4</sup>,  
A. H. Windle<sup>4</sup>, A. L. Chuvilin<sup>5</sup>, and L. G. Bulusheva<sup>1</sup>

<sup>1</sup> *Institute of Inorganic Chemistry, Siberian Division, Russian Academy of Sciences,  
pr. Akademika Lavrent'eva 3, Novosibirsk, 630090 Russia  
e-mail: spectrum@che.nsk.su*

<sup>2</sup> *Laboratori Nazionali di Frascati, INFN, I-00044 Frascati (RM), Italy*

<sup>3</sup> *Lebedev Physical Institute, Russian Academy of Sciences, Leninskiĭ pr. 53, Moscow, 119991 Russia*

<sup>4</sup> *Department of Materials Science and Metallurgy, Cambridge, United Kingdom*

<sup>5</sup> *Boreskov Institute of Catalysis, Siberian Division, Russian Academy of Sciences,  
pr. Akademika Lavrent'eva 5, Novosibirsk, 630090 Russia*

Received September 16, 2004; in final form, December 6, 2004

The angular dependence of the intensity of  $CK_{\alpha}$  radiation measured from a film of oriented carbon nanotubes shows an increase in the yield of x-ray fluorescence along the growth direction of the nanotubes. The angular distribution of the intensity of scattered x rays is close in magnitude to the angular distribution of the directivity of nanotubes in the film that is determined by analyzing an electron-microscope image. To explain the propagation of radiation along the nanotubes, two mechanisms are proposed on the basis of reflection from inner walls of a tube (channeling) and an anomalous dispersion of  $CK_{\alpha}$  photons in the carbon medium. © 2005 Pleiades Publishing, Inc.

PACS numbers: 07.85.Fv; 41.50.+h; 61.85.+p; 78.70.Ck; 81.07.De

Carbon nanotubes are quasi-one-dimensional structures formed by the self-assembly of carbon atoms at high temperatures. The existence of an internal cylindrical hollow implies the possibility of channeling charged particles, neutrons, and x rays in nanotubes [1–4]. The propagation of x rays in the nanotube hollow can be considered as multiple reflections from the walls of the tube similar to the propagation of radiation in capillary structures [5, 6]. The features of refraction of radiation in micron-diameter capillaries are well studied (see [4] and references cited therein). The most interesting feature of the propagation of radiation near the strongly curved surface of the channel is the surface channeling of radiation [7]. The effective wavelength of ultrasoft photons is approximately equal to the diameter of the internal hollow of nanotubes  $\lambda_{\perp} \approx d_0$  ( $d_0 = 1$ – $10$  nm). Therefore, it is necessary to take into account wave features leading to the bulk channeling of radiation in nanotubes. In this case, wave effects of surface channeling are strongly suppressed [8]. The difficulty of the manipulation of nanoobjects and the low scattering intensity restrict the possibilities for experimentally studying x-ray radiation in an individual carbon nanotube. However, orientational dependences can be measured for an array of ordered nanotubes. One of the most common methods of producing film structures consisting of oriented carbon nanotubes is the method

of the pyrolysis of carbon compounds in the presence of catalyst particles [9].

The aim of this work is to study the orientational effect of the texture of a carbon nanotube film on the intensity of  $CK_{\alpha}$  radiation. The angular dependence of the intensity of x rays from the film is compared with the degree of the disorder of the nanotubes in a sample, which is determined by analyzing an electron-microscope image. The angular divergence of x rays propagating in the channel of a multilayer carbon nanotube has been theoretically estimated.

The films of multilayer carbon nanotubes were grown on the surface of a silicon plate via the process of the pyrolysis of vapors of a mixture of fullerene  $C_{60}$  and ferrocene  $Fe(C_5H_5)_2$  in a tube furnace 1 m in length and 3.8 cm in diameter with an atmospheric pressure of argon and at a temperature of  $950^{\circ}C$ . The resulting materials were analyzed with the use of a JSM 6340F scanning electron microscope and a JEOL 100C transmission electron microscope. Carbon nanotubes were formed on a substrate and had a prevailing orientation perpendicular to the surface (Fig. 1a). The mean length of nanotubes coincided with a film thickness of about  $30 \mu m$ . The film consists of individual nanotubes  $10$ – $30$  nm in diameter (Fig. 1b) and their bundles possessed a mean distance between tubes of about  $100$  nm. The nanotubes are multiwalled, the diameter of the internal hollow of tubes was equal to  $5$ – $7$  nm (Fig. 1c), and the

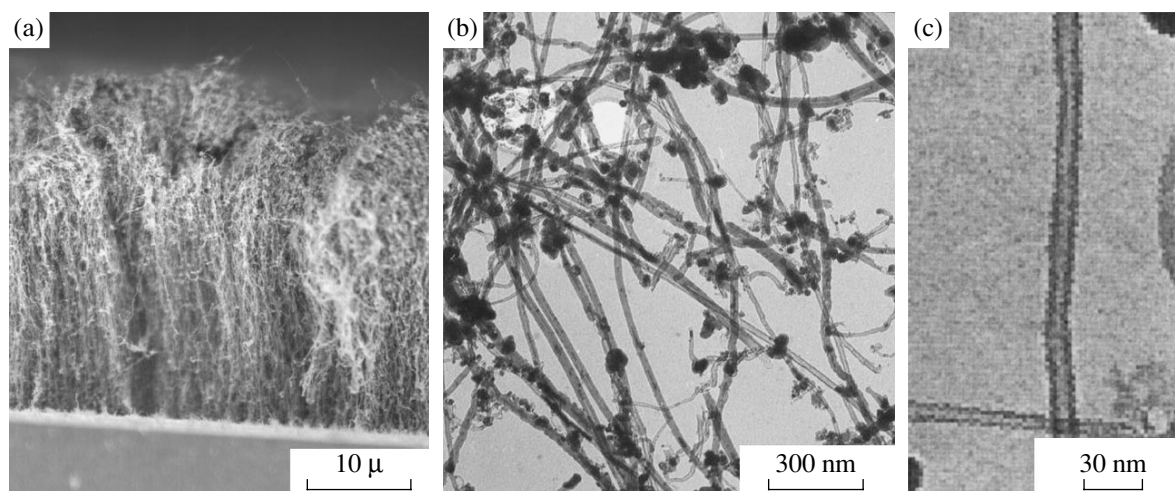


**Fig. 1.** (a) Image of the carbon-nanotube film on the silicon-plate surface as obtained by scanning electron microscopy, (b) the image of nanotubes forming the film as obtained by transmission electron microscopy, and (c) the enlarged image of multilayer nanotubes.

number of layers varied from 7 to 30. Transmission electron microscopy showed that, in addition to nanotubes, the samples contained metal nanoparticles, which served as a catalyst of nanotube growth.

The intensity of x rays from the film of oriented nanotubes was measured by a deep-vacuum laboratory x-ray spectrometer. Figure 2 shows the arrangement of a sample, an x-ray source, and a gate emergence slit. The  $8 \times 2$ -mm sample was mounted on a rotating axis, which made it possible to vary the angle  $\alpha$  between the sample surface and optical axis of the spectrometer from  $60^\circ$  to  $100^\circ$ . The positions of the copper anode and the gate emergence slit were fixed. The angle  $\beta$  complementary to the angle between the direction from the surface of the primary anode to the sample and spectrometer axis was  $20^\circ$ . The directions of radiation incident on the sample and fluorescence propagation through the collimator are denoted as I and II in Fig. 2. A gas proportional counter filled with methane at a pressure of 0.2 atm was placed behind the system of collimating slits. This optical system ensured an angular resolution of about  $0.5^\circ$ . The x-ray tube operated at a voltage of 2.3 kV and a current of 0.1 A. The count rate at the intensity maximum was equal to 3000 pulses per second. The angular dependence of x-ray fluorescence was measured for initial sample 1 with the vertical orientation of nanotubes. Measurements were then carried out for the same sample, where the vertical orientation of nanotubes was broken due to mechanical action on the film surface (sample 2). The disorientation of nanotubes in sample 2 was corroborated by scanning electron microscopy (SEM).

To estimate the angular directivity of nanotubes (texture) in sample 1, SEM microphotographs of the film were mathematically processed. Figure 3 shows an image of the lateral cut of the carbon-nanotube film and Fourier-analysis data for this image, which enable one

to estimate the degree of the disorientation of nanotubes with respect to the growth axis [10]. The resulting dependence (Fig. 3b) is the averaged angular distribution of nanotubes for the film section presented on the microphotograph. The distribution is characterized by a maximum at  $90^\circ$  with a width of about  $20^\circ$ . To obtain the image of the lateral cut, the film sample was cleaved. As a result, the texture of nanotubes was partially broken. For this reason, one can expect that the angular distribution of nanotubes in the initial sample can be significantly narrower. Moreover, electron microscopy provides information on the material structure only in the local region of the sample.

X-ray fluorescence is due to the occupation of previously created core vacancies by valence electrons. Owing to the localization and symmetry of the inner C1s level, the x-ray fluorescence of carbon atoms is isotropic. However, the probability of radiation in single

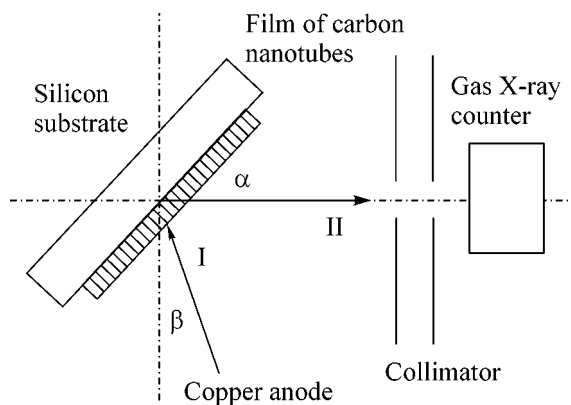


**Fig. 2.** Layout of measurements of the angular dependence of x-ray fluorescence yield from the film of oriented nanotubes.

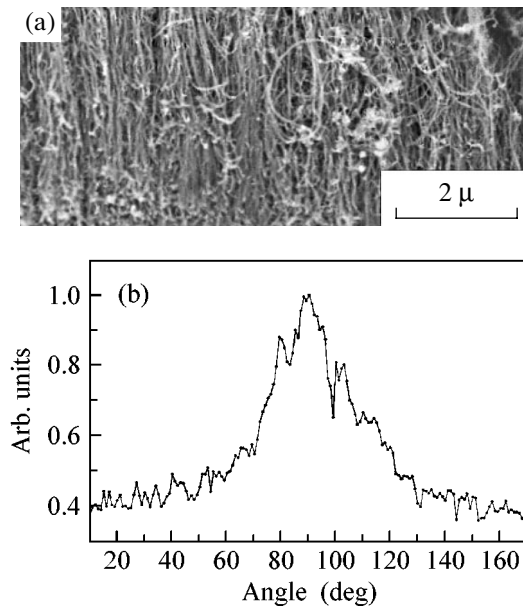


**Fig. 3.** (a) Image of the section of the lateral film surface of oriented nanotubes and (b) the angular distribution of the directivity of nanotubes with respect to the substrate surface as constructed on the basis of the Fourier transform of this image.

crystals depends on the electron distribution in the valence band and is a complicated function of the fluorescence-yield angle. In layered structures consisting of  $2p$  elements, fluorescence radiation can be completely or partially polarized for transitions involving different-symmetry bands. In particular, in the x-ray spectra of graphite, the contributions of  $\pi$  and  $\sigma$  components change depending on the angular orientation of the detector [11, 12]. The shape of the x-ray  $CK_{\alpha}$  spectrum changes monotonically, and the total intensity of the spectrum must change similarly.

Figure 4 shows the angular dependences of the intensities (curve 1)  $I_1(\alpha)$  and (curve 2)  $I_2(\alpha)$  of x-ray fluorescence that were measured for samples consisting of the oriented and disoriented nanotubes, respectively. The dependences were normalized such that the lines coincide in the angular range  $60^{\circ}$ – $70^{\circ}$ . As is seen, the angular distributions for samples 1 and 2 are close to each other and demonstrate an increase in the intensity at angles of  $60^{\circ}$  to  $85^{\circ}$  and a decrease in the intensity at larger angles. Lines differ only for angles close to  $90^{\circ}$ , where additional intensity appears for sample 1 of the oriented nanotubes. The effective density of the film is one-thirtieth to one-twentieth of the density of graphite. Therefore, the excitation of  $CK_{\alpha}$  radiation occurs over the entire depth of the film. Since the absorption coefficient of  $CK_{\alpha}$  radiation in the carbon film is comparatively small [13], radiation from the entire thickness of the sample can contribute to the detected spectrum.

For the texture-free sample, the angular distribution of x-ray fluorescence depends on the geometric param-

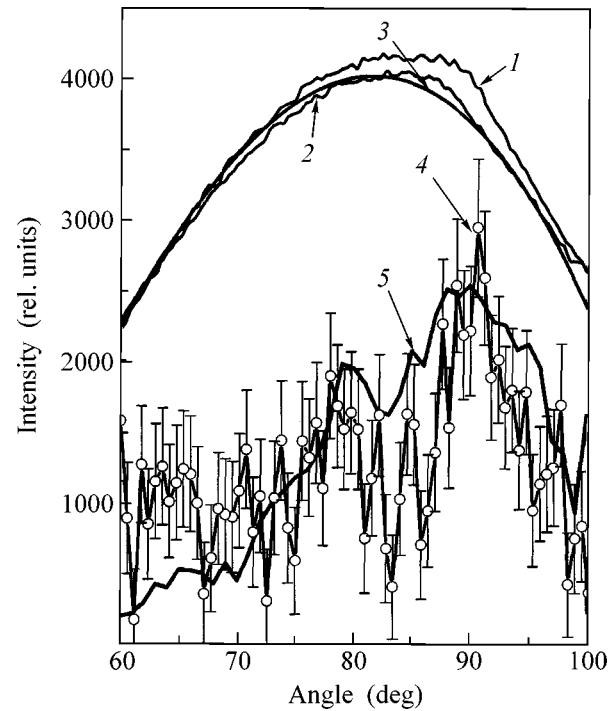


**Fig. 4.** Angular dependence of the intensity of x-ray fluorescence as measured for (1) the film of oriented nanotubes and (2) the film of disoriented nanotubes and (3) as calculated by formula (1) for an isotropic sample, as well as (4) the fivefold increased difference between curves 1 and 2. The error bars show the statistical spread of the curve  $4\sigma = (I_1)^{0.5} + (I_2)^{0.5}$ . For comparison, curve 5 shows part of the angular distribution of the directivity of carbon nanotubes as obtained by mathematically processing the electron microscope image (Fig. 3).

eters of the experiment and absorption coefficients for the incident and fluorescence beams and can be expressed by the formula

$$I = I_0 \sin \alpha \sin(110^{\circ} - \alpha) \exp\left(-\frac{\eta \cos(20^{\circ} - \alpha)}{\sin \alpha}\right). \quad (1)$$

Here,  $I_0$  is the intensity of incident radiation and  $\eta$  is the factor determined by the absorption coefficient and sample density. Change in the visible surface as a function of the angle  $\alpha$  is also taken into account in Eq. (1). Formula (1) is presented in Fig. 4 by curve 3. The parameter  $\eta$  was chosen such that curves 3 and 2 are in best agreement in the angular range over which the measurement was carried out. Curve 3 has an asymmetric shape with a maximum near  $82^{\circ}$ . The difference between experimental curve 2 and curve 3 can be attributed to the imperfection of the film structure, in particular, to the presence of metal inclusions, thickness inhomogeneity of the film, etc. Moreover, it is not excluded that, after mechanical action on the sample of oriented nanotubes, small sections of the textured film hold.

To reveal the effect of the film texture on the angular distribution of  $CK_\alpha$  radiation, the difference between lines 1 and 2 is obtained and multiplied by a factor of five, and the result is presented in Fig. 4 by line 4. The accumulated number of pulses per channel when measuring dependences 1 and 2 was equal to about 40000 at a maximum, which makes it possible to determine the difference between them with an accuracy of about 0.3% of the total intensity. A large statistical spread in the difference line is associated with a small effect of anisotropic scattering. Nevertheless, the presence of a maximum at  $\alpha = 90^\circ$  with a width of  $6^\circ$  is identified with a probability of more than 97%. In our opinion, this feature can be attributed to the directing action of carbon nanotubes on the propagation of x-ray fluorescence in the film. Knowing the total intensity of the difference line, one can estimate that the angle of radiation trapping in the direction of the orientation of nanotubes is equal to about  $6^\circ$ . A broad scattering halo that is superimposed on the general fluorescence background is formed due to nanotubes with large bending angles. For comparison, the part of the angular distribution obtained for carbon nanotubes as obtained from the Fourier analysis of the SEM image is also shown in Fig. 4 (line 5). Both lines have maxima at an angle of  $\alpha = 90^\circ$ , which confirms the determining effect of the orientation of nanotubes in the sample on the directivity of the scattering of x-ray radiation. The difference between lines 5 and 4 can be attributed to the electron-microscopy features mentioned above and the inhomogeneity of the sample.

Two causes of the orienting effect of carbon nanotubes on the propagation of x rays along them are possible. The first cause may be the channeling effect, which arises due to the anomalous scattering of x-ray photons on the walls of the internal hollow of nanotubes. In the x-ray range, the refractive index is slightly smaller than unity. Therefore, the vacuum is a denser medium for x rays. The propagation of x rays in the channels of microcapillaries is described on the basis of the effect of total internal reflection. For nanotubes, such an approximation is valid only for sufficiently hard photons, i.e., under the condition  $\lambda_\perp < d_0$ . In the case under consideration, this condition is violated, and all estimates must be obtained in the wave approximation [4].

Atoms in carbon nanotubes are arranged in hexagons forming the walls of tubes. In the first approximation, a channel formed in such a way is axisymmetric. The interaction of an x-ray photon with a medium is determined by the plasmon energy  $\omega_0 = \sqrt{4\pi e^2 N_0 / m_0}$ , where  $e$  and  $m_0$  are the charge and mass of an electron, respectively, and  $N_0$  is the density of the electron cloud of a nanotube. Since the electron density can be approximated by an averaged axisymmetric function, which is minimal in the channel center and maximal on the walls, the averaged plasmon energy has the same sym-

metry [6]. Estimates show that this energy at a maximum varies in the range  $(\omega_0)_{\max} \approx 100\text{--}170$  eV depending on the character of the formation of a nano-system. The angular divergence of photons channeled in the averaged potential of a nanotube is given by the expression  $\overline{\theta^2} = \int dV \theta^2 f(\theta, \mathbf{r})$ , where  $f(\theta, \mathbf{r})$  is the radiation distribution function in the nanotube channel, and it is determined by the interaction potential of x-ray photons with the electrons of the medium. By analogy with the scattering of channeling electrons in crystals [14], the angular divergence can be estimated by the formula

$$\overline{\Delta\theta_{\text{ch}}^2} \propto \int_{\omega_{\min}}^{\omega_{\max}} d\omega \frac{N_{\text{ph}}(\omega)}{\omega^2} \int_0^{r_0} dx N_0(x),$$

where  $r_0$  is the radius of the internal hollow of the nanotube and  $\omega$  and  $N_{\text{ph}}(\omega)$  are the energy and number of emitted photons, respectively. For carbon nanotubes with  $r_0 \approx 2.5\text{--}3.5$  nm, the angle of radiation trapping in the internal channel of the tube is estimated as  $\overline{\Delta\theta} \leq 6^\circ\text{--}10^\circ$ . Thus, the contribution of the channeling of x rays to the formation of the total pattern of radiation scattering in the film of carbon nanotubes is small and cannot exceed 0.5%, which agrees well with the experimental value.

The main part of radiation undergoes diffuse scattering, which is determined by the structure and density of nanotubes, as well as by the presence of structures differing from tubular. In our opinion, diffuse scattering forms a broad halo in the angular distribution of fluorescence. Moreover, secondary radiation can pass through “gaps,” when x-ray photons propagate in cavities between nanotubes and bundles of nanotubes. This is so-called “effect of the collimation” of radiation. The effect of collimation absorption is considerably suppressed due to a small absorption coefficient for  $CK_\alpha$  radiation near the  $K$  absorption edge [13]. We estimate this contribution to the angular distribution of radiation from the film of oriented nanotubes as follows. The mean “visibility distance” in the “forest” of nanotubes in a plane parallel to the substrate is equal to about 600 nm. The absorption coefficient is so small that a 2- $\mu\text{m}$ -thick carbon film can be used as a window in an x-ray counter to detect  $CK_\alpha$  bands, in particular, in the x-ray spectrometer used in the experiments. Therefore, an x-ray photon must cover a distance of about 35  $\mu\text{m}$  for noticeable absorption. The angular width of the corresponding distribution is  $\geq 50^\circ$ , which is much larger than the width of the feature observed at an angle of  $90^\circ$ .

A nonzero thickness of the walls of multilayer nanotubes  $\Delta d_0 \approx 2\text{--}10$  nm (7–30 layers) is responsible for the specific propagation of radiation in a nanochannel, leading to diffraction effects and restricting the angular

divergence. The cause is that the width of the main mode of radiation propagation in the channeling regime ( $\sim 10\text{--}100$  nm) may be larger than the wall thickness, which, in turn, leads to the tunneling of radiation through the potential barrier of the wall. In this case, it is necessary to take into account the diffraction of radiation in the multilayer system, which determines the angular divergence of the dechanneled fraction of radiation. According to estimates, this value is of the same order of magnitude as the angular divergence of the channeling of x-ray photons.

Another possible cause of the orienting effect of the propagation of  $CK_\alpha$  radiation along nanotubes is the conditions for anomalous dispersion. The decrement of the refractive index  $\delta$  for photons with a wavelength of  $\lambda \sim 0.1$  nm in the carbon medium is equal to about  $\sim 10^{-6}$  [15]. If the photon energy is slightly lower than the edge of the absorption band of the medium, the decrement of the refractive index is negative and increases significantly in magnitude [16]. This behavior leads to total internal reflection, and, therefore, a nanotube behaves as a hollow waveguide [17]. In this case, the critical angle is determined as  $\varphi_0 \sim \sqrt{2} \delta$  and is equal to about  $2.5^\circ$  for a carbon sample with  $\delta \sim -10^{-3}$ . Therefore, the propagation of x-ray photons in the film of ideally oriented carbon nanotubes is characterized by an angular divergence of about  $5^\circ$ . The total intensity of such “trapped” radiation can be equal to about 0.5%, which is close to the total intensity of line 4 (Fig. 4).

Thus, the measurements and analysis show the possibility of the dominant propagation of  $CK_\alpha$  radiation along carbon nanotubes.

#### REFERENCES

1. V. V. Klimov and V. S. Letokhov, Phys. Lett. A **222**, 424 (1996).
2. G. V. Dedkov, Nucl. Instrum. Methods Phys. Res. B **143**, 584 (1998).
3. N. K. Zhevago and V. I. Glebov, Phys. Lett. A **250**, 360 (1998).
4. S. B. Dabagov, Usp. Fiz. Nauk **173**, 1083 (2003) [Phys. Usp. **46**, 1053 (2003)].
5. M. A. Kumakhov and F. F. Komarov, Phys. Rep. **191**, 289 (1990).
6. M. A. Kumakhov, Proc. SPIE **4155**, 1 (2000).
7. G. Cappuccio, S. B. Dabagov, A. Pifferi, and C. Gramaccioni, Appl. Phys. Lett. **78**, 2822 (2001).
8. S. B. Dabagov, in *X-ray and Inner-Shell Processes*, Ed. by A. Bianconi, A. Marcelli, and N. L. Saini (AIP, New York, 2003); AIP Conf. Proc. **652**, 89 (2003); S. Bellucci and S. B. Dabagov, J. Phys.: Condens. Matter **15**, 3171 (2003).
9. M. Terrones, N. Grobert, J. P. Zhang, *et al.*, Chem. Phys. Lett. **285**, 299 (1998).
10. I. A. Kinloch, C. Singh, M. Nolte, *et al.*, in *Proceedings of Nanotech03: Nanotechnology in Carbon and Related Materials* (Univ. of Sussex at Brighton, UK, 2003), p. 10.
11. A. Simunek and G. Wiech, Solid State Commun. **64**, 1375 (1987).
12. A. V. Okotrub, A. V. Gusel'nikov, and L. G. Bulusheva, *Nanoengineered Nanofibrous Materials, NATO Science Series Volume NATO-ASI (PST 979397)*, Ed. by S. I. Guceri, Y. Gogotsi, and V. Kuznetsov (Kluwer Academic, Dordrecht, Netherlands, 2004), p. 347.
13. B. L. Henke *et al.*, At. Data Nucl. Data Tables **27**, 1 (1982).
14. S. B. Dabagov, Radiat. Eff. Defects Solids **25**, 103 (1993).
15. Z. G. Pinsker, *Dynamical Scattering of X-rays in Crystals* (Nauka, Moscow, 1974; Springer, Berlin, 1978).
16. M. A. Blokhin, *Physics of X-rays* (Gostekhizdat, Moscow, 1957) [in Russian].
17. A. M. Zheltikov, Usp. Fiz. Nauk **170**, 1203 (2000) [Phys. Usp. **43**, 1125 (2000)].

*Translated by R. Tyapaev*

# Irradiation-Induced Suppression of the Critical Temperature in High- $T_c$ Superconductors: Pair Breaking Versus Phase Fluctuations<sup>†</sup>

L. A. Openov

Moscow Engineering Physics Institute, Moscow, 115409 Russia

e-mail: [opn@supercon.mephi.ru](mailto:opn@supercon.mephi.ru)

Received November 30, 2004

Experiments on the irradiation-induced suppression of the critical temperature in high- $T_c$  superconductors are analyzed within the mean-field Abrikosov-Gor'kov-like approach. It is shown that the experimental data for  $\text{YBa}_2\text{Cu}_3\text{O}_{7-\delta}$  single crystals can be quantitatively explained by the pair-breaking effects under the assumption of the combined effect of potential and spin-flip scattering on the critical temperature and with an accounting for a nonpure  $d$ -wave superconducting order parameter. © 2005 Pleiades Publishing, Inc.

PACS numbers: 74.20.-z; 74.25.Fy; 74.62.Dh; 74.72.Bk

Particle irradiation is a powerful tool that provides an opportunity to modify the physical properties of superconductors. Irradiation-induced defects act as effective pinning centers [1], thus causing the critical current density to increase. Apart from the practical benefits, irradiation effects may be used to probe the fundamental characteristics of superconductors. For example, peculiarities of the disorder-induced suppression of the critical temperature  $T_c$  are expected to depend on the pairing mechanism and the symmetry of the superconducting order parameter  $\Delta(\mathbf{p})$ . In this respect, a study of the response of high- $T_c$  cuprates to intentionally incorporated impurities or radiation defects provides an indirect way to elucidate the cause of their unusual normal- and superconducting properties. Among other things, depending on the symmetry of  $\Delta(\mathbf{p})$ , clear differences were predicted for the defect-induced variations of experimentally accessible characteristics such as  $T_c$  [2, 3], the density of states [4], the isotope coefficient [5], the specific-heat jump [6], etc.

Various mechanisms of the disorder-induced  $T_c$  suppression have been considered, including, e.g., the pair-breaking [7], localization [8], and phase-fluctuation [9] effects, etc. The main problem here is that the disorder results not only in a decrease in  $T_c$  but also in the strong increase in the width of the superconducting transition,  $\Delta T_c$ , so that the functional form of  $T_c$  versus, e.g., the defect concentration  $x_d$  appears to be poorly defined at  $T_c \ll T_{c0}$ , where  $T_{c0}$  is the initial value of  $T_c$  in the absence of the disorder. In fact, the value of  $\Delta T_c$  usually becomes comparable to the value of  $T_c$  at  $T_c/T_{c0} \approx 0.3$  [10, 11]. While the measured  $T_c$  versus  $x_d$  curve in high- $T_c$

cuprates was commonly observed to be approximately linear at  $T_c/T_{c0} > 0.3$  [10], the details of  $T_c(x_d)$  behavior at  $T_c/T_{c0} \ll 1$  remained unclear.

In a recent paper [12], Rullier-Albenque *et al.* reported the results of experimental studies of  $T_c$  degradation under electron irradiation of underdoped and optimally doped  $\text{YBa}_2\text{Cu}_3\text{O}_{7-\delta}$  single crystals. They have measured  $T_c$  and in-plane resistivity  $\rho_{ab}$  in a very broad range of  $x_d$ , the value of  $x_d$  being proportional to  $\Delta\rho_{ab}$ , the increase in  $\rho_{ab}$  upon irradiation. The authors of [12] succeeded in the creation of an extremely uniform distribution of radiation defects over the sample, so that the value of  $\Delta T_c$  never exceeded 5 K. Moreover, the value of  $\Delta T_c$  did not increase monotonously with radiation dose but had a maximum at  $T_c/T_{c0} \approx 0.3$  and subsequently decreased again to  $\Delta T_c < 1$  K at the highest dose for which the resistive superconducting transition was still observed at  $T_c \approx 1$  K. Thus, the dependence of  $T_c$  on  $\Delta\rho_{ab}$  (or  $x_d$ ) was obtained with an excellent accuracy from  $T_c/T_{c0} = 1$  down to  $T_c/T_{c0} = 0$  (or, at least,  $T_c/T_{c0} \sim 10^{-2}$ ).

It was found in [12] that  $T_c$  unexpectedly decreased quasi-linearly with  $x_d$  in the *entire* range from  $T_{c0}$  down to  $T_c = 0$ . Having compared the results obtained with the predictions of Abrikosov-Gor'kov (AG) pair-breaking [13] and Emery–Kivelson phase-fluctuations [9] theories, the authors of [12] arrived at the conclusion that the experimental data are at variance with AG theory and point to a significant role of phase fluctuations of the order parameter in high- $T_c$  superconductors.

To compare the pair-breaking theory with the experiment, the authors of [12] made use of the AG formula

<sup>†</sup>This article was submitted by the author in English.

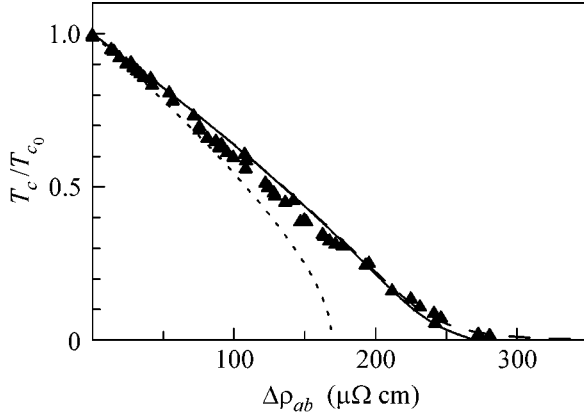


**Fig. 1.**  $T_c/T_{c0}$  versus  $\Delta\rho_{ab}$  in electron-irradiated  $\text{YBa}_2\text{Cu}_3\text{O}_7$  crystals. Experiment [12] (triangles). Theory (Eqs. (2)–(5)) for  $\omega_{pl} = 0.75$  eV,  $\chi = 0.9$ , and  $\alpha = 0$  (dashed line), 0.01 (solid line), and 1 (dotted line).

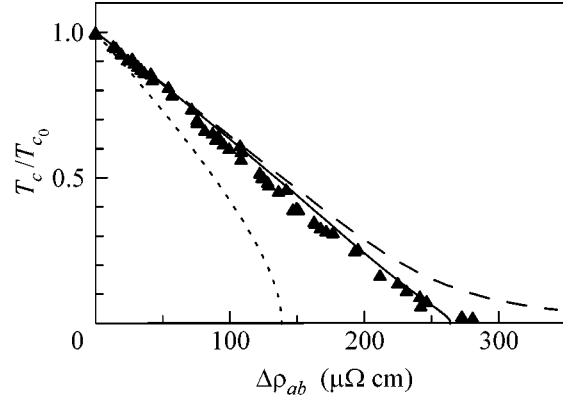


**Fig. 2.** The same as in Fig. 1 for  $\omega_{pl} = 0.8$  eV,  $\chi = 0.8$ , and  $\alpha = 0$  (dashed line), 0.04 (solid line), and 1 (dotted line).

[13] for a  $d$ -wave superconductor (we set  $\hbar = 1$  hereinafter):

$$\ln(T_{c0}/T_c) = \Psi(1/2 + 1/4\pi T_c \tau) - \Psi(1/2), \quad (1)$$

where  $\Psi(z)$  is the digamma function and  $\tau$  is the electron scattering time [14],  $\tau^{-1} \propto x_d \propto \Delta\rho_{ab}$ . This formula gives a negative curvature of the  $T_c$  versus  $\Delta\rho_{ab}$  curve, contrary to the experimental observations. Note, however, that, first, the symmetry of  $\Delta(\mathbf{p})$  in  $\text{YBa}_2\text{Cu}_3\text{O}_{7-\delta}$  is different from pure  $d$  wave due to an orthorhombic lattice distortion [15], and, second, irradiation may result in the appearance of spin-flip scatterers along with potential ones, since radiation defects created in  $\text{CuO}_2$  planes disturb antiferromagnetic correlations between copper spins. The AG-like formula that accounts for both those effects reads [3, 16]

$$\ln\left(\frac{T_{c0}}{T_c}\right) = (1 - \chi) \left[ \Psi\left(\frac{1}{2} + \frac{1}{2\pi T_c \tau_s}\right) - \Psi\left(\frac{1}{2}\right) \right] + \chi \left[ \Psi\left(\frac{1}{2} + \frac{1}{4\pi T_c} \left(\frac{1}{\tau_p} + \frac{1}{\tau_s}\right)\right) - \Psi\left(\frac{1}{2}\right) \right], \quad (2)$$

where  $\tau_p$  and  $\tau_s$  are scattering times due to potential and spin-flip scatterers, respectively; the coefficient

$$\chi = 1 - \langle \Delta(\mathbf{p}) \rangle_{FS}^2 / \langle \Delta^2(\mathbf{p}) \rangle_{FS} \quad (3)$$

is a measure of the degree of in-plane anisotropy of  $\Delta(\mathbf{p})$ ; and  $\langle \dots \rangle_{FS}$  means the Fermi surface (FS) average. The range  $0 \leq \chi \leq 1$  covers the cases of isotropic  $s$ -wave ( $\Delta(\mathbf{p}) = \text{const}$ ,  $\chi = 0$ ),  $d$ -wave ( $\langle \Delta(\mathbf{p}) \rangle_{FS} = 0$ ,  $\chi = 1$ ), and mixed ( $d + s$ )-wave or anisotropic  $s$ -wave ( $0 < \chi < 1$ ) symmetries of  $\Delta(\mathbf{p})$ .

In fact, the assumption concerning the combined effect of potential and spin-flip scatterers on  $T_c$  and accounting for a nonpure  $d$  wave  $\Delta(\mathbf{p})$  in  $\text{YBa}_2\text{Cu}_3\text{O}_{7-\delta}$  (i.e.,  $\chi \neq 1$ ) allows for a quantitative explanation of the

experimental data [12] within the modified pair-breaking AG-like theory [17], without resorting to phase-fluctuations effects [9]. Figure 1 shows the measured  $T_c/T_{c0}$  versus  $\Delta\rho_{ab}$  curve taken from [12] along with theoretical curves computed with Eq. (2) for  $\chi = 0.9$  and various values of the coefficient

$$\alpha = \tau_s^{-1} / (\tau_p^{-1} + \tau_s^{-1}) \quad (4)$$

that specifies the relative contribution of spin-flip scatterers to the total scattering rate. Here, we represent the scattering time in terms of the in-plane residual resistivity  $\rho_0$  obtained by the extrapolation of  $\rho_{ab}(T)$  to  $T = 0$ ,

$$\tau_p^{-1} + \tau_s^{-1} = (\omega_{pl}^2 / 4\pi) \rho_0, \quad (5)$$

where  $\omega_{pl}$  is the plasma frequency (see [7, 16]). We also make use of the fact that  $\rho_0 = \Delta\rho_{ab}$  in a very good approximation [12]. From Fig. 1, one can see that, at  $\chi = 0.9$  and  $\omega_{pl} = 0.75$  eV, the quasi-linear experimental dependence of  $T_c$  on  $\Delta\rho_{ab}$  in  $\text{YBa}_2\text{Cu}_3\text{O}_7$  is quantitatively reproduced at  $\alpha = 0$ –0.01.

We emphasize that the quantity  $\omega_{pl}$  that enters into Eq. (2) for  $T_c$  through relation (5) should be considered as just a characteristic energy that does not necessarily coincide with the value of the plasma frequency determined by, e.g., optical spectroscopy. Based on general grounds, one could expect  $\omega_{pl} \sim 1$  eV. In this respect, although our choice of  $\omega_{pl} = 0.75$  eV is, to some extent, arbitrary, a change in  $\omega_{pl}$  results only in a change in the best-fitting values of  $\chi$  and  $\alpha$ . For example,  $\chi \approx 0.8$  and 0.6,  $\alpha = 0.04 \pm 0.01$ , and  $0.045 \pm 0.01$  for  $\omega_{pl} = 0.8$  and 1.0 eV, respectively (see Figs. 2 and 3). Meanwhile, for  $\chi = 1$ , i.e., for pure  $d$ -wave symmetry of  $\Delta(\mathbf{p})$ , the experimental data cannot be described at any value of  $\omega_{pl}$  (see Fig. 4). This is not surprising, because of the orthorhombic crystal structure of  $\text{YBa}_2\text{Cu}_3\text{O}_{7-\delta}$ , which excludes the pure  $d$ -wave symmetry of  $\Delta(\mathbf{p})$  and points

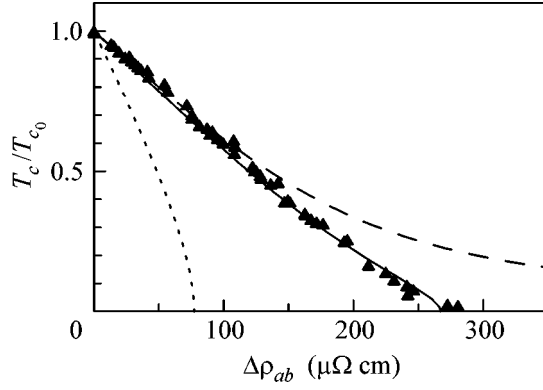


**Fig. 3.** The same as in Fig. 1 for  $\omega_{pl} = 1.0$  eV,  $\chi = 0.6$ , and  $\alpha = 0$  (dashed line), 0.045 (solid line), and 1 (dotted line).

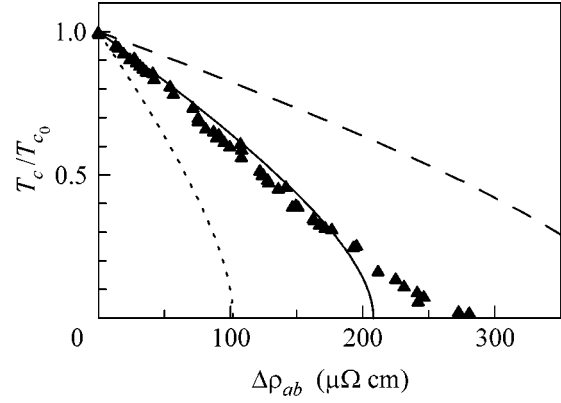


**Fig. 4.** The same as in Fig. 1 for  $\chi = 1$  and  $\omega_{pl} = 0.5$  eV (dashed line), 0.7 eV (solid line), and 1 eV (dotted line) (see [18]).

to an admixture of the  $s$ -wave component to the  $d$ -wave type, so that  $\Delta(\mathbf{p})$  is of  $(d + s)$ -wave or  $(d + is)$ -wave type [15]. Thus, the experimental data [12] for  $\text{YBa}_2\text{Cu}_3\text{O}_7$  single crystals can be quantitatively explained by the pair-breaking theory taking a nonpure  $d$  wave  $\Delta(\mathbf{p})$  and the combined effect of potential and spin-flip scatterers on  $T_c$  into account.

As for the underdoped single crystals  $\text{YBa}_2\text{Cu}_3\text{O}_{6.6}$ , the experimental dependence [12] of  $T_c/T_{c0}$  versus  $\Delta\rho_{ab}$  is close to that for  $\text{YBa}_2\text{Cu}_3\text{O}_7$  and can be fitted within the same approach at similar values of  $\omega_{pl}$ ,  $\chi$ , and  $\alpha$ . The discussion of the probable effect of the oxygen content, i.e., the hole concentration, on the value of  $\omega_{pl}$ , the gap anisotropy, and the relative amount of spin-flip scatterers in the sample is, however, beyond the scope of this paper.

Note that  $\chi < 1$  not only for a mixed  $(d + s)$  wave  $\Delta(\mathbf{p})$  but also for an anisotropic  $s$  wave  $\Delta(\mathbf{p})$ . Recently, the  $d$ -wave symmetry of  $\Delta(\mathbf{p})$  in hole-doped cuprate superconductors [19] has been doubted by several authors (see, e.g., [20, 21]). The reanalysis of the results obtained by angle-resolved photoemission spectroscopy, Fourier-transform scanning tunneling spectroscopy, low-temperature thermal conductivity, etc., including phase-sensitive techniques, has shown that the combined data agree quantitatively with the extended  $s$ -wave symmetry [20, 21]. Making use of the fit [21]  $\Delta(\theta) = 24.5(\cos 4\theta + 0.225)$  meV to single-particle tunneling spectra of  $\text{YBa}_2\text{Cu}_3\text{O}_{7-\delta}$ , with the angle  $\theta$  being measured from the Cu–O bonding direction, we have  $\chi \approx 0.9$  for  $\text{YBa}_2\text{Cu}_3\text{O}_{7-\delta}$ . It follows from the fits presented in [21] that an even lower value of  $\chi$  may be expected for  $\text{Bi}_2\text{Sr}_2\text{CaCu}_2\text{O}_{8+y}$ . In this respect, it would be very interesting to study the behavior of  $T_c$  versus  $\rho_{ab}$  in this and other high- $T_c$  cuprates down to  $T_c = 0$ .

Finally, a note is in order about one more argument presented in [12] in favor of the phase-fluctuations theory and against the pair-breaking mechanism of  $T_c$  suppression in high- $T_c$  cuprates. According to [12], the pos-

itive curvature of the  $T_c(\Delta\rho_{ab})$  curve is necessary to explain the maximum of the transition width  $\Delta T_c$  as a function of  $\Delta\rho_{ab}$  that was experimentally observed at  $T_c/T_{c0} \approx 0.3$ . Note, however, that, first, this argument is incompatible with the experimental data themselves, since the curvature of the *measured*  $T_c(\Delta\rho_{ab})$  dependence is (with a few exceptions) close to zero in the whole range of  $\Delta\rho_{ab}$  and, respectively, in the whole range of  $T_c/T_{c0}$ , including the region near  $T_c/T_{c0} \approx 0.3$ . Second, the line of reasoning in [12] is based on a naive assumption that  $\Delta T_c(x_d) \propto x_d(dT_c/dx_d)$ . Such an assumption is at least questionable for the resistive superconducting transition whose critical temperature and width are determined by the zero-resistance path and the uniformity of the defect distribution, respectively. Besides this, the value of  $\Delta T_c$  depends on a specific criterion used for its evaluation from the curve  $\rho_{ab}(T)$ . Thus, knowledge of the function  $T_c(x_d)$  alone is obviously insufficient to draw definite conclusions about the function  $\Delta T_c(x_d)$ , and vice versa.

We note that the phase-fluctuations theory [9] goes beyond the standard mean-field theory and implies that the so-called pseudogap [22] is a precursor of superconductivity. This contradicts the experiments, which give evidence for interplay between competing and coexisting (superconducting and nonsuperconducting) ground states (see, e.g., [23]). We note also that the AG-like pair-breaking approach is based on the BCS–Bogolyubov mean-field theory that seems to describe the spatial-momentum quasiparticle states in high- $T_c$  cuprates, at least in optimally doped samples such as, e.g.,  $\text{YBa}_2\text{Cu}_3\text{O}_7$ , rather well [24, 25].

In summary, we have shown that experiments on the irradiation-induced  $T_c$  suppression in  $\text{YBa}_2\text{Cu}_3\text{O}_{7-\delta}$  can be quantitatively explained within the AG-like pair-breaking mean-field theory under the assumption of the combined effect of potential and spin-flip scattering on  $T_c$  and with an accounting for a nonzero Fermi surface average of the superconducting order parameter, with-

out resorting to phase-fluctuations effects. One cannot exclude, however, a possibility that the latter become important at  $T_c \rightarrow 0$ , i.e., in the very vicinity of the superconductor–insulator transition.

I am grateful to A.V. Kuznetsov for assistance.

### REFERENCES

1. L. Civale, A. D. Marwick, T. K. Worthington, *et al.*, Phys. Rev. Lett. **67**, 648 (1991).
2. A. A. Abrikosov, Physica C (Amsterdam) **214**, 107 (1993).
3. L. A. Openov, Pis'ma Zh. Éksp. Teor. Fiz. **66**, 627 (1997) [JETP Lett. **66**, 661 (1997)].
4. S. V. Pokrovsky and V. L. Pokrovsky, Phys. Rev. B **54**, 13275 (1996).
5. L. A. Openov, I. A. Semenihin, and R. Kishore, Phys. Rev. B **64**, 012513 (2001).
6. L. A. Openov, Phys. Rev. B **69**, 224516 (2004).
7. R. J. Radtke, K. Levin, H.-B. Schüttler, and M. R. Norman, Phys. Rev. B **48**, 653 (1993).
8. V. F. Elesin, Zh. Éksp. Teor. Fiz. **105**, 168 (1994) [JETP **78**, 89 (1994)].
9. V. J. Emery and S. A. Kivelson, Nature **374**, 434 (1995).
10. V. F. Elesin, K. E. Kor'kov, A. V. Krasheninnikov, and L. A. Openov, Zh. Éksp. Teor. Fiz. **110**, 731 (1996) [JETP **83**, 395 (1996)], and references therein.
11. S. K. Tolpygo, J.-Y. Lin, M. Gurvitch, *et al.*, Phys. Rev. B **53**, 12454 (1996).
12. F. Rullier-Albenque, H. Alloul, and R. Tourbot, Phys. Rev. Lett. **91**, 047001 (2003).
13. A. A. Abrikosov and L. P. Gor'kov, Zh. Éksp. Teor. Fiz. **39**, 1781 (1960) [Sov. Phys. JETP **12**, 1243 (1961)].
14. In Ref. [12], the authors erroneously made use of the AG formula for  $T_c$  of an isotropic  $s$ -wave superconductor disordered by magnetic impurities. The correct formula (Eq. (1)) for a  $d$ -wave superconductor differs from that used in Ref. [12] by a factor of two in the term containing the scattering time, the value of  $\tau$  being the *total* scattering time due to *both* potential and spin-flip scattering; see, e.g., Refs. [2, 7]. However, this does not change the overall conclusions drawn in Ref. [12].
15. K. A. Kouznetsov, A. G. Sun, B. Chen, *et al.*, Phys. Rev. Lett. **79**, 3050 (1997).
16. L. A. Openov, Phys. Rev. B **58**, 9468 (1998).
17. L. A. Openov, Phys. Rev. Lett. **93**, 129701 (2004).
18. Note that in a  $d$ -wave superconductor ( $\chi = 1$ ), the value of  $T_c$  does not depend on  $\alpha$ , see Eqs. (2) and (4).
19. C. C. Tsuei and J. R. Kirtley, Rev. Mod. Phys. **72**, 969 (2000).
20. B. H. Brandow, Phys. Rev. B **65**, 054503 (2002).
21. G. M. Zhao, Phys. Rev. B **64**, 024503 (2001); cond-mat/0305483.
22. T. Timusk and B. Statt, Rep. Prog. Phys. **62**, 61 (1999).
23. L. Alff, Y. Krockenberger, B. Welter, *et al.*, Nature **422**, 698 (2003).
24. K. McElroy, R. W. Simmonds, J. E. Hoffman, *et al.*, Nature **422**, 592 (2003).
25. H. Matsui, T. Sato, T. Takahashi, *et al.*, Phys. Rev. Lett. **90**, 217002 (2003).

# Plasma Generated from Collision of Cluster Beams<sup>†</sup>

B. M. Smirnov

*Institute for High Temperatures, Moscow, 127412 Russia*

Received November 17, 2004; in final form, December 16, 2004

Processes are analyzed in the course of production of a microplasma as a result of the collision of two dense cluster beams. In reality, this microplasma is characterized by a lifetime of  $\sim 1$  ns, by a size of  $\sim 0.01$  cm, by a number density of electrons of  $\sim 10^{20}$  cm $^{-3}$ , by an electron temperature of several tens of eV, and by a charge of its multicharged ions of up to  $z = 10$ . Under contemporary conditions, the laser method allows one to create a hot microplasma with a higher electron temperature and charge of atomic ions. © 2005 Pleiades Publishing, Inc.

PACS numbers: 36.40.–c; 52.20.Hv; 52.50.–b

## INTRODUCTION

A convenient method for the generation of a hot microplasma consists in irradiation of a cluster beam by a femtosecond laser pulse of high intensity, so that the electric-field strength of the laser field exceeds that inside the hydrogen atom by several orders of magnitude. As a result of the absorption process, clusters are excited by taking on the energy of an electromagnetic wave. The subsequent expansion of excited cluster matter during times of 0.1–1 ps leads to the formation of a more or less uniform microplasma that can be used as a source of x-ray radiation, neutrons, and fast multicharged ions, and these processes proceed during the expansion time of this uniform plasma ( $\sim 1$  ns) [1–3]. Though excited multicharged ions, which are responsible for the x-ray radiation of this plasma, can be formed at the first stage of cluster excitation, the generation of x-ray radiation proceeds mostly in a uniform microplasma.

Below, we consider an alternative method for the creation of such a microplasma that results from the collision of two intense cluster beams. Collision of two clusters that are moving towards each other or collisions of a cluster with individual nuclei lead to the transformation of the kinetic energy of nuclei in cluster beams into the energy of excitation of a forming microplasma. Our goal is to analyze the processes that proceed in the course of formation of this microplasma and to estimate the parameters of the plasma.

## CLUSTER PARAMETERS IN COLLIDING CLUSTER BEAMS

A general scheme of this process corresponds to the almost frontal collision of two dense cluster beams after their generation. As a result, a microplasma is formed in the region of the collision of the cluster beams, and the energy of this microplasma is taken

from the kinetic energy of the colliding beams. Because this process requires a high intensity and a small duration for the colliding beams, we will be guided by the pulse scheme of cluster generation [4]. Using an example of tungsten clusters, we use the parameters of clusters in a beam evaluated for this scheme. These parameters for the tungsten case are as follows: a typical number of cluster atoms is  $n \sim 10^6$ ; the number density of bound atoms in clusters is  $N_b \sim 4 \times 10^{19}$  cm $^{-3}$ ; and a radius of a cluster beam is 40  $\mu$ m. Note that the number density of bound atoms corresponds to the number density of multicharged ions in a forming microplasma.

At a certain stage of cluster generation, clusters are charged by an electron beam. A charge of an individual cluster is restricted by its strength, and the Rayleigh instability threshold gives the maximum cluster charge [5, 6]  $Z_{cr} \approx (5Ar/e^2)^{1/2}$ , where  $A$  is the specific cluster surface energy and the cluster radius  $r$  is expressed through the Wigner–Seits radius  $r_W$  as  $r = r_W n^{1/3}$ . From this formula, we have, for a tungsten cluster of the indicated size ( $A = 4.7$  eV,  $r_W = 1.6 \text{ \AA}$  [7]),  $Z_{cr}/n \approx 2 \times 10^{-3}$ . It is necessary to account both for the decrease of the reduced cluster strength due to cluster excitation by an electron beam in the course of its ionization and also for its increase if a cluster is broken apart by electron impact, so that these effects are mutually cancelled. We take below  $Z/n = 1 \times 10^{-3}$  for the case under consideration.

At the last stage of cluster generation, clusters are accelerated in an electric field. We assume the pulse electric potential in which clusters are accelerated to be equal to 1 and 10 MV in the two examples under consideration, and these values are available for the contemporary pulse technique. This corresponds to an energy per nucleus of 1 and 10 keV, respectively, and this corresponds to cluster velocities of  $3 \times 10^6$  and  $1 \times 10^7$  cm/s. For the pulse method of cluster generation [4], when clusters are formed from a drop of radius 10  $\mu$ m and the final radius of a generated cluster beam

<sup>†</sup>This article was submitted by the author in English.

is 40  $\mu\text{m}$ , the total energy transmitted to clusters is 0.02 and 0.2 J, respectively. Later collisions of clusters and collisions of clusters with free ions lead to the formation of a microplasma, so that a typical nucleus charge in this microplasma is  $z \sim 10$  and a typical plasma temperature is several tens of eV.

### PROCESSES OF COLLISION OF CLUSTER BEAMS AND PARAMETERS OF MICROPLASMA

As a result of the collision of two cluster beams, the kinetic energy is converted in the excitation of the electron component, and a hot plasma is formed that is similar to that resulting from the excitation of a cluster beam by a femtosecond laser pulse [1–3]. In this case, during the collision of two clusters, atoms of one cluster penetrate into the other one and are decelerated there by interaction with the electron component. As a result, the nuclei almost stop, and the excitation energy of the electron subsystem is equal to the initial kinetic energy of the nuclei. Considering almost frontal collisions of cluster beams with a small angle between them, we obtain the following criterion for the beam length  $L$  in order for each cluster to take part in the collision:

$$N_{cl}\sigma L \geq 1. \quad (1)$$

Here,  $\sigma = 4\pi r_w^2 n^{2/3}$  is the cross section of collision of two identical clusters and  $r_w$  is the Wigner–Seits radius of clusters. From this, we find the beam length

$$L \geq \frac{n^{1/3}}{4\pi r_w^2 N_b} \quad (2)$$

and, for the above parameters ( $N_b \sim 1 \times 10^{19} \text{ cm}^{-3}$ ,  $r_w \approx 1.6 \text{ \AA}$ ), criterion (2) gives  $L \geq 30 \mu\text{m}$ . This corresponds to a beam size under the pulse method [4] of its generation and gives a collision time of  $\tau = L/v \approx 1 \text{ ns}$ , which is also a typical lifetime of a forming microplasma that occupies a region of size  $\sim L$  during this time.

We now consider the character of transformation of the cluster kinetic energy into the excitation energy of a forming microplasma. According to a study of cluster collision with a solid surface [8–13], during this collision cluster nuclei penetrate into a solid, and, then, under the pressure of a cluster shock, a shockwave is formed at some distance from the solid surface, so that the transformation of the kinetic energy of cluster beams proceeds to a large extent through a shock wave. In the case of cluster collisions, this mechanism does not hold true because of their small size. Another mechanism of this process consists in the excitation of the electron subsystem by moving nuclei, including collective effects such as plasma oscillations, and we consider this mechanism for two limiting cases, taking into account that a typical nuclear velocity is small compared to typical electron velocities. Indeed, if a nucleus is moving with a low velocity inside an electron subsystem that is found in the ground state, a small part of

the electrons can take part in transitions, because the transition with a small change in the electron momentum is prohibited for the majority of electrons. If the electron subsystem is excited, this prohibition does not hold, and the transformation of the nucleus energy proceeds more effectively.

For the ground state of the electron subsystem, we consider the model of a dense degenerate electron gas in which electrons are located in a Fermi sphere in a space of electron momenta. Since the nucleus velocity is

$$v \ll v_F, \quad (3)$$

where  $v_F$  is the electron velocity on the Fermi surface, only electrons near the Fermi surface (at a distance from it  $\sim v$ ) can partake in transitions. This gives, for the deceleration rate [14, 15],

$$\begin{aligned} -\frac{dE}{dx} &= \frac{2z\hbar v}{3\pi a_o^2} \left[ \ln\left(\frac{4}{\alpha}\right) - 3 + 3\alpha \ln\frac{4}{\alpha} - \frac{11}{2}\alpha \right] \\ &= C(\alpha) \frac{z\hbar v}{a_o^2}, \quad \alpha = \frac{v}{\pi v_F}. \end{aligned} \quad (4)$$

Here, a small parameter of this expansion is  $\alpha \approx v/\pi v_F$ ,  $a_o$  is the Bohr radius, and  $z$  is the effective charge of a nucleus when it is moving with a velocity  $v$  inside the cluster.

Considering cluster electrons as a degenerate electron gas, we have the Fermi velocity for these electrons:

$$\begin{aligned} v_F &= \frac{\hbar}{m_e} (3\pi^2 N_e)^{1/3} = \frac{\hbar}{m_e} \left( 3\pi^2 \frac{z\rho}{m} \right)^{1/3} \\ &= \frac{\hbar}{m_e r_w} \left( \frac{9\pi z}{4} \right)^{1/3}, \end{aligned} \quad (5)$$

where  $N_e$  is the electron number density,  $z$  is the nucleus charge in a degenerate electron gas,  $\rho$  is the tungsten density, and  $m$  is the atom mass. The electron shell of tungsten atoms is  $5d^4 6s^2$ , and we assume that electrons of these shells can form a degenerate electron gas; i.e.,  $z = 6$ . This gives  $v_F = 1.2e^2/\hbar$  for the tungsten case and  $\alpha = 0.004$  and  $\alpha = 0.012$  for the tungsten-nucleus energies 1 and 10 keV, respectively. For these cases, we have  $C(\alpha) = 0.86$  and  $C(\alpha) = 0.60$ . The mean free path of a nucleus inside the cluster with respect to its deceleration is, according to formula (4),

$$\lambda = \frac{E a_o^2}{z\hbar v C(\alpha)}, \quad (6)$$

and, for the tungsten cases under consideration, we have  $\lambda = 500a_o$  and  $\lambda = 200a_o$ . In reality, excitation of the electron subsystem accelerates the excitation process, and, hence, these values are overstated.

In the other limiting case, when final channels for electron transition are open, the deceleration rate for a

moving nucleus with respect to the excitation of electrons is given by [16]

$$-\frac{dE}{dt} = N_e v \frac{4\pi z e^4}{m_e v^2} \ln \Lambda, \quad (7)$$

where the Coulomb logarithm is  $\ln \Lambda = \ln(p_{\max}/p_{\min})$ ;  $p_{\max} = m_e v$  is the maximum momentum transferred to a scattered electron;  $p_{\min}$  is its minimum value, which is determined by the structure of the electron subsystem; and we take, for definiteness,  $\ln \Lambda \approx 5-10$ . From this, we have, for the nucleus mean free path with respect to interaction with an electron subsystem,

$$\lambda = \frac{Em_e v^2 r_w^3}{3z^2 e^4 \ln \Lambda}, \quad (8)$$

and, for the parameters of an example under consideration, we obtain  $\lambda \ll a_0$ . In reality, we have an intermediate case between these two limiting ones. Indeed, if we start from the ground state of the electron subsystem, the rate of excitation of the electron subsystem increases sharply in the course of an increase in the degree of its excitation.

Thus, the transformation of the kinetic energy of clusters and the collision of two cluster beams results from the mutual penetration of atomic cores of one cluster into another cluster, and these cores are decelerated by excitation of the electron subsystem. Because the deceleration process is the same in the case of an individual atom, transformation of the kinetic energy also proceeds in collisions of individual atoms and atomic ions with clusters and their fragments before the Coulomb explosion of excited clusters. This leads to effective conversion of the initial kinetic energy of cluster beams into the energy of a forming microplasma.

We now consider the properties of this microplasma from another standpoint. Various processes lead to the establishment of an equilibrium, so that a forming microplasma consists of electrons and multicharged ions. Assuming the ionization equilibrium to be fulfilled, we find the electron temperature  $T_e$  at which the equilibrium constant is

$$K(T) = \frac{1}{N_e} \left( \frac{m_e T_e}{2\pi\hbar^2} \right)^{3/2} \exp\left(-\frac{J_z}{T_e}\right), \quad (9)$$

where  $J_z$  is the ionization potential for an atomic ion of a charge  $z$ . Taking  $z \approx 6$ , we find that the ionization equilibrium takes place at  $J_z/T_e \approx 12$ . From this, we have that, at typical temperatures in the range  $T_e = 20-40$  eV, ionization takes place for ions with an ionization potential  $J_z \approx 200-500$  eV that corresponds to  $z = 7-12$ . Note that the kinetic energy of plasma electrons and ions is in the range 150–300 eV in these cases; i.e., a significant portion of the initial cluster energy is consumed upon ionization of atoms and their ions.

## MICROPLASMA FROM CLUSTER COLLISIONS AND CLUSTER LASER PLASMA

The properties of this microplasma are similar to those obtained by excitation of a cluster beam by an ultrashort and superpower laser pulse. The lifetime of the plasma resulting from the collision of two clusters is  $\sim r_w n^{1/3}/v \sim 5 \times 10^{-13}$  s, and, during this time, a dense microplasma is formed inside a region of cluster collision with a number density of electrons of  $N_e \sim 10^{24}$  cm $^{-3}$ , and, then, this plasma expands and is characterized by the electron number density  $10^{19}-10^{20}$  cm $^{-3}$ . The latter plasma lives for a time of  $\sim 1$  ns. The electron temperature of this microplasma is several tens of electron volts, and the charge of multicharged ions of this plasma is about  $z = 10$ . These parameters are restricted by the kinetic energy of nuclei in the incident cluster beams, which we take to be 1 keV per nucleus. This value can be increased by a decrease in the size of clusters in a beam and by an increase in the kinetic energy of clusters as determined by an experimental technique and can be raised in the course of improvement of the experimental technique.

As for a microplasma formed as a result of irradiation of a cluster beam by a femtosecond laser pulse, its parameters are better, though both microplasmas have approximately the same lifetime ( $\sim 1$  ns) at the last stage of their evolution, when each microplasma is almost uniform. Indeed, the temperature of the cluster-laser plasma is 0.1–1 keV, and the charge of multicharged ions of this plasma can be  $z \approx 30$  (for example, see [17–19]).

Thus, at the contemporary stage of the experimental technique, the parameters of the microplasma resulting from the collision of two cluster beams yield to those of a laser-cluster plasma. In spite of this, the alternative case of creation of a hot nanosecond microplasma is worthy of notice, since the development of this method can give new results for this microplasma.

This paper is supported in part by the Russian Foundation for Basic Research (project no. 03-02-16059).

## REFERENCES

1. T. Ditmire, T. Donnelly, R. W. Falcone, and M. D. Perry, *Phys. Rev. Lett.* **75**, 3122 (1995).
2. T. Ditmire, R. A. Smith, R. S. Marjoribanks, *et al.*, *Appl. Phys. Lett.* **71**, 166 (1997).
3. V. P. Krainov and M. B. Smirnov, *Phys. Rep.* **370**, 237 (2002).
4. B. M. Smirnov, *Phys. Usp.* **46**, 589 (2003).
5. L. D. Landau and E. M. Lifshitz, *Electrodynamics of Continuous Media* (GIFML, Moscow, 1959; Addison-Wesley, Reading, Mass., 1960).
6. A. V. Eletsii and B. M. Smirnov, *Sov. Phys. Usp.* **32**, 763 (1989).
7. B. M. Smirnov, *Clusters and Small Particles in Gases and Plasmas* (Springer, New York, 2000).

8. G. Basbas and R. H. Ritchie, Phys. Rev. A **25**, 1943 (1982).
9. S. Eliezer, J. M. Martinez-Val, and C. Deutsch, Laser Part. Beams **13**, 43 (1995).
10. A. Bret and C. Deutsch, Fusion Eng. Des. **32–33**, 517 (1996).
11. C. Deutsch *et al.*, Fusion Technol. **31**, 1 (1997).
12. G. Zwicknagel and C. Deutsch, Phys. Rev. E **56**, 970 (1997).
13. A. Bret and C. Deutsch, Nucl. Instrum. Methods Phys. Res. A **415**, 703 (1998).
14. E. Fermi and E. Teller, Phys. Rev. **72**, 399 (1947).
15. B. M. Smirnov, Zh. Éksp. Teor. Fiz. **44**, 192 (1963) [Sov. Phys. JETP **17**, 133 (1963)].
16. L. D. Landau and E. M. Lifshitz, *Course of Theoretical Physics*, Vol. 3: *Quantum Mechanics: Non-Relativistic Theory*, 4th ed. (Nauka, Moscow, 1989; Pergamon, Oxford, 1980).
17. Y. L. Shao *et al.*, Phys. Rev. Lett. **77**, 3343 (1996).
18. G. C. Junkel-Vives *et al.*, Phys. Rev. A **66**, 033204 (2002).
19. M. B. Smirnov and W. Becker, Phys. Rev. A **69**, 013201 (2004).